University of Kentucky
UKnowledge

Theses and Dissertations--Mechanical Engineering | Mechanical Engineering

2014

FABRICATION OF MAGNETIC TWO-DIMENSIONAL AND THREE-DIMENSIONAL MICROSTRUCTURES FOR MICROFLUIDICS AND MICROROBOTICS APPLICATIONS

Hui Li
University of Kentucky, uky.huili@gmail.com

Click here to let us know how access to this document benefits you.

Recommended Citation
Li, Hui, "FABRICATION OF MAGNETIC TWO-DIMENSIONAL AND THREE-DIMENSIONAL MICROSTRUCTURES FOR MICROFLUIDICS AND MICROROBOTICS APPLICATIONS" (2014). *Theses and Dissertations--Mechanical Engineering*. 51.
https://uknowledge.uky.edu/me_etds/51

This Doctoral Dissertation is brought to you for free and open access by the Mechanical Engineering at UKnowledge. It has been accepted for inclusion in Theses and Dissertations--Mechanical Engineering by an authorized administrator of UKnowledge. For more information, please contact UKnowledge@lsv.uky.edu.

STUDENT AGREEMENT:

I represent that my thesis or dissertation and abstract are my original work. Proper attribution has been given to all outside sources. I understand that I am solely responsible for obtaining any needed copyright permissions. I have obtained needed written permission statement(s) from the owner(s) of each third-party copyrighted matter to be included in my work, allowing electronic distribution (if such use is not permitted by the fair use doctrine) which will be submitted to UKnowledge as Additional File.

I hereby grant to The University of Kentucky and its agents the irrevocable, non-exclusive, and royalty-free license to archive and make accessible my work in whole or in part in all forms of media, now or hereafter known. I agree that the document mentioned above may be made available immediately for worldwide access unless an embargo applies.

I retain all other ownership rights to the copyright of my work. I also retain the right to use in future works (such as articles or books) all or part of my work. I understand that I am free to register the copyright to my work.

REVIEW, APPROVAL AND ACCEPTANCE

The document mentioned above has been reviewed and accepted by the student's advisor, on behalf of the advisory committee, and by the Director of Graduate Studies (DGS), on behalf of the program; we verify that this is the final, approved version of the student's thesis including all changes required by the advisory committee. The undersigned agree to abide by the statements above.

Hui Li, Student

Dr. Christine Ann Trinkle, Major Professor

Dr. James M. McDonough, Director of Graduate Studies

FABRICATION OF MAGNETIC TWO-DIMENSIONAL AND THREE-DIMENSIONAL MICROSTRUCTURES FOR MICROFLUIDICS AND MICROROBOTICS APPLICATIONS

A dissertation submitted in partial fulfillment of the requirements for the degree of Doctor of Philosophy in the College of Engineering at the University of Kentucky

By

Hui Li

Lexington, Kentucky

Co-director: Dr. Christine Ann Trinkle, Professor of Mechanical Engineering

Co-director: Dr. Lyndon Scott Stephens, Professor of Mechanical Engineering

Copyright © Hui Li 2014

ABSTRACT OF DISSERTATION

FABRICATION OF MAGNETIC TWO-DIMENSIONAL AND THREE-DIMENSIONAL MICROSTRUCTURES FOR MICROFLUIDICS AND MICROROBOTICS APPLICATIONS

Micro-electro-mechanical systems (MEMS) technology has had an increasing impact on industry and our society. A wide range of MEMS devices are used in every aspects of our life, from microaccelerators and microgyroscopes to microscale drug-delivery systems. The increasing complexity of microsystems demands diverse microfabrication methods and actuation strategies to realize. Currently, it is challenging for existing microfabrication methods—particularly 3D microfabrication methods—to integrate multiple materials into the same component. This is a particular challenge for some applications, such as microrobotics and microfluidics, where integration of magnetically-responsive materials would be beneficial, because it enables contact-free actuation. In addition, most existing microfabrication methods can only fabricate flat, layered geometries; the few that can fabricate real 3D microstructures are not cost efficient and cannot realize mass production.

This dissertation explores two solutions to these microfabrication problems: first, a method for integrating magnetically responsive regions into microstructures using photolithography, and second, a method for creating three-dimensional freestanding microstructures using a modified micromolding technique. The first method is a facile method of producing inexpensive freestanding photopatternable polymer micromagnets composed NdFeB microparticles dispersed in SU-8 photoresist. The microfabrication process is capable of fabricating polymer micromagnets with 3 μm feature resolution and greater than 10:1 aspect ratio. This method was used to demonstrate the creation of freestanding microrobots with an encapsulated magnetic core. A magnetic control system was developed and the magnetic microrobots were moved along a desired path at an average speed of 1.7 mm/s in a fluid environment under the presence of external magnetic field. A microfabrication process using aligned mask micromolding and soft lithography was also developed for creating freestanding microstructures with true 3D geometry. Characterization of this method and resolution limits were demonstrated. The combination of these two microfabrication methods has great potential for integrating several material types into one microstructure for a variety of applications.

KEYWORDS: MEMS, Microfabrication, Freestanding Two- & Three-Dimensional Microstructures, Magnetic Microrobots, Microfluidics and Microrobotics

Hui Li

____
Student's Signature

December 3, 2014

____
Date

FABRICATION OF MAGNETIC TWO-DIMENSIONAL AND THREE-DIMENSIONAL MICROSTRUCTURES FOR MICROFLUIDICS AND MICROROBOTICS APPLICATIONS

By

Hui Li

Christine Ann Trinkle
Co-Director of Dissertation

Lyndon Scott Stephens
Co-Director of Dissertation

James M. McDonough
Director of Graduate Studies

December 3, 2014

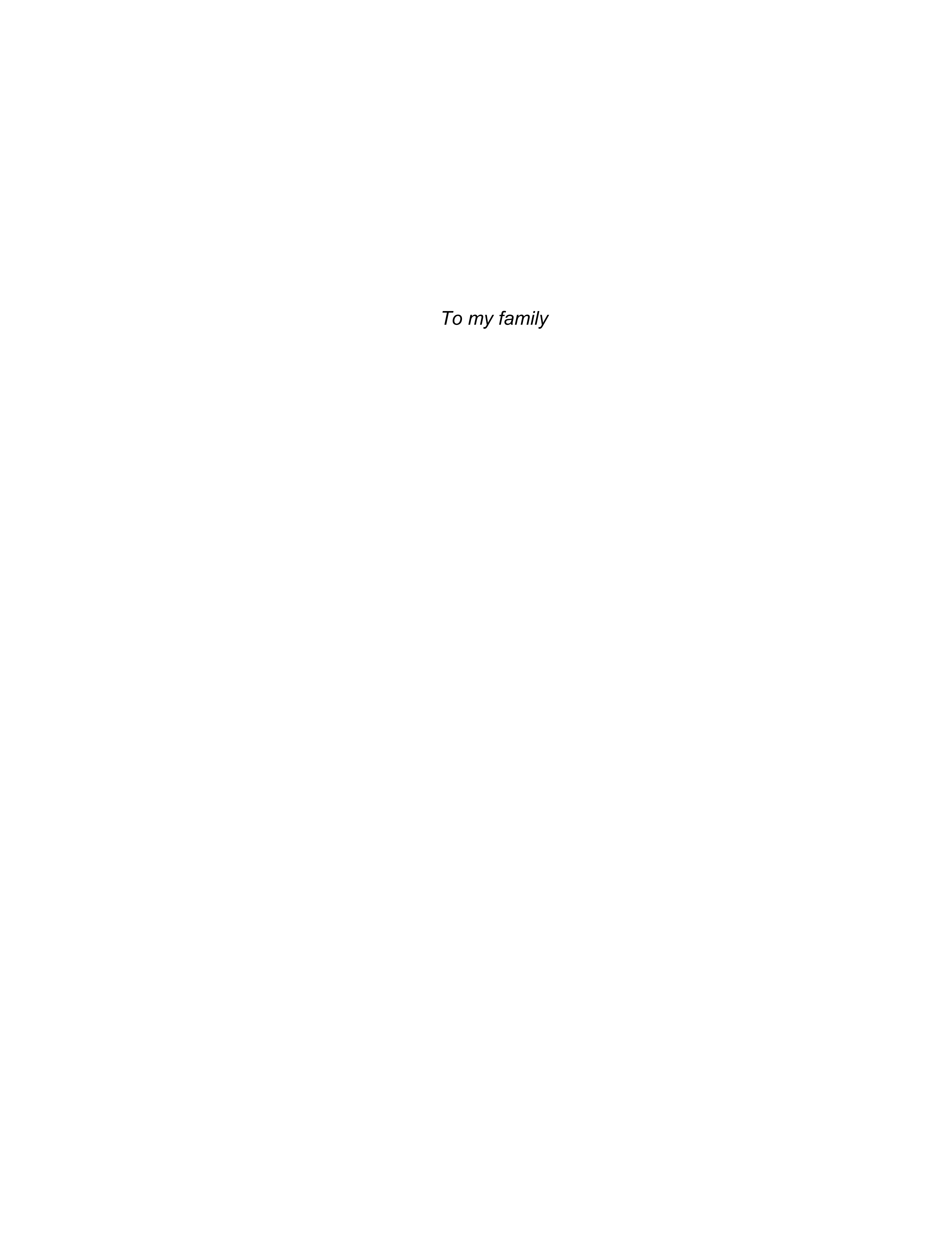

To my family

ACKNOWLEGEMENT

I would like to express my sincere gratitude to my advisor, Dr. L. Scott Stephens, for all of his support, guidance, and motivation, especially, the great opportunity he offered keeping me in the academic research area and leading me to micro-electro-mechanical systems. I would like to convey my deep appreciation to my advisor, Dr. Christine A. Trinkle. She opened the doors to MEMS for me and led me onto the avenue towards MEMS research. Her continuous encouragement, guidance, support and understanding helped me on my Ph.D. work in the past four years. She deserves a tremendous amount of credit for this work and my development as a researcher and technical writer. I would also like to thank Dr. Tim Wu and Dr. Keith Rouch for their serving as my dissertation committee members and critical review of my research. I also thank Dr. Laurence G. Hassebrook serving as my outsider examiner.

I thank Dr. Charles E. May, Mr. Brian Wajdyk, and all the staff for the equipments training and technique support in the Center for Nanoscale Science and Engineering (CeNSE) at the University of Kentucky. I also thank Dr. Jia Ye, Dr. Dali Qian, and Lei Wang, for training me on SEM and EDX in the Electron Microscopy Center at the University of Kentucky. I would also like to thank Mr. Herb Mefford and Mr. Nick Cprek for their machining experiment parts for my research.

I would like to thank all my lab members, Dr. Wei Li, Tyler J. Flynn, Ning Ge, and Dr. David Weatherly. I thank them for their sharing hands-on experience, scientific discussions, suggestions and advices on my research. They make my study pleasant and memorable. I would like to thank Dr. Mettin Sitti of Carnegie Mellon University for productive conversations on microrobotics applications of the magnetic polymer.

I would like to thank AMT Nano, LLC of Lexington, KY for providing partial funding of this work under SBIR grant No. SB1341-11-SE-0864 from the National Institutes of Standards and Technology, and under a matching grant from the Kentucky Cabinet for Economic Development, Office of Entrepreneurship, under grant agreement KSTC-184-512-12-122 with the Kentucky Science and Technology Corporation. I also want to thank the National Science Foundation under Grant No. CMMI-1125722 for the three-dimensional mold material.

Last, I would love to thank my family for their unconditional love, support and encouragement, especially my father, thank him for always believing in me. I also thank my wife, Jing Chen, for her endless love, supporting, and encouraging me pursuing what I love wholeheartedly. And to my little daughter Grace, she brings me endless joy and pleasure.

TABLE OF CONTENTS

ACKNOWLEGEMENT....iii
TABLE OF CONTENTS v
LIST OF TABLES vii
LIST OF FIGURES viii
Chapter 1 Introduction 1
1.1 Background and Motivation 1
1.2 Dissertation Organization 3
Chapter 2 Literature Review 5
2.1 Freestanding Microstructure Fabrication 9
2.1.1 Freestanding One- and Two- dimensional Microstructure Fabrication .. 9
2.1.2 Freestanding Three-dimensional Microstructres Fabrication 12
2.1.3 Freestanding Microstructures Release Techniques 23
2.2 Contact-free Control in MEMS.... 30
Chapter 3 Fabrication of Two-dimensional Polymer Micromagnets.... 41
3.1 Introduction 41
3.2 Materials and Fabrication Method 42
3.3 Composite Material Characterization 45
3.4 Summary 54
Chapter 4 Fabrication and Contact-free Actuation of Encapsulated Micromagnets for Microrobotics Applications.... 55
4.1 Introduction 55
4.2 Encapsulated Magnetic Microrobot Fabrication 57
4.3 Surface Characterization of Microfabrication Method.... 60
4.3.1 Surface Texture Description.... 60
4.3.2 Areal Surface Parameters for Biplanar Surfaces 62
4.3.3 Surface Analysis Results and Discussion 66
4.4 Force Calculations on Mobile Magnetic Microrobots 69

4.5 Remote Actuation of Magnetic Microrobots 76
4.6 Summary 78
Chapter 5 Creation of Freestanding Three Dimensional Microstructures by Aligned Mask Micromolding 79
5.1 Introduction 79
5.2 Materials and Methods 80
5.3 Demonstration of Film-Free Micromolding 84
5.4 Film Thickness Measurements 86
5.5 Solvent Loss Experiments 89
5.6 Summary 90
Chapter 6 Conclusions and Future Work 92
6.1 Conclusions 92
6.2 Future Work 93
References 95
Vita 112

LIST OF TABLES

Table 3.1 Fabrication properties and patterning resolution limits of magnetic polymer composite [121] 54
Table 4.1 Feature Area Fraction [161] 62
Table 4.2 Closed Form Solutions for Surface Parameters [161] 65
Table 4.3 Typical Measurement Data for Polymer Asperity Surfaces [161] 68
Table 5.1 Properties of SU-8 series 10 89

LIST OF FIGURES

Figure 2.1 Typical UV photolithography fabrication process. 7
Figure 2.2 “Idealized” SU8 molecule with epoxy groups [45]. 8
Figure 2.3 Schematic diagram of capillary force lithography. (A) When the film is relatively thick with respect to the mold’s step height; (b) when it is relatively thin [58]. 10
Figure 2.4 (A) Description of the SU-8 lift-off process for the fabrication of the DWP [61]. (B) Fabrication process for multi-level SU-8 microstructures (left) and examples of fabricated SU-8 microstructures (Right) [40]. 11
Figure 2.5 The 313 nm absorption method (left); SEM image of clamp structure made by the method (right) [60]... 12
Figure 2.6 (a) Example of a three-level gray-scale mask pattern and the resulting photoresist structure. (b) Three gray levels patterned in AZ 4620 photoresist resulting from a similar mask pattern [63]. 13
Figure 2.7 SEM image showing developed AZ 4620 photoresist using a 3.5 μm pitch and one row per pixel size [63]. 14
Figure 2.8 The principle of scanning-based microstereolithography [15]............ 15
Figure 2.9 Scanning-based micrpstereolithography processes to produce 3D microstructures: (a) 3D STL model; (b) sliced 2D sections; (c) binary images; (d) stacking; (e) final structure [67]... 16
Figure 2.10 (a) Schematic diagram of DMD-based microstereolithography system. SEM images of complex 3D microstructures with down-facing surfaces successfully fabricated using MSL and cure depth control: (b) 4 micro-springs and (c) micro-wineglass [67]. 17
Figure 2.11 Outline of 3-D method of fabrication based on pixels exposed lithography. (A) Concept underlying this method, using the mask with pattern created function where SR light is shaped by aperture, and amount of exposure energy is controlled by closing and opening aperture with actuator; (B) using the

mask with pattern created function to apply mosaicked energy distribution to resist surface [77]. 19
Figure 2.12 (a) 3D microstructure derived from Equation 2.2. (b) 3D microstructures fabricated by overlapping ½ aperture size. (c) 3D microstructures fabricated by overlapping ¼ aperture size [77]. 20
Figure 2.13 Schematic of microneedles fabriacation by “drawn lithography” and SEM images of the microneedles [78]. 21
Figure 2.14 Fabricated microbowl (left) and eight electrodes after the ball bearing release (right) [79]. 22
Figure 2.15 (a) Self-scrolling method for ABF fabrication. Bi- or tri-layered thin-film ribbons and a square nickel head are grown and deposited, respectively. After wet-etching, the ribbons curl into helices in a controlled manner. (b) GLAD fabricated helices. Pillars are deposited at an angle and under constant rotation of the stage, resulting in helices on the spherical seeds [84] 23
Figure 2.16 Schematic of general sacrificial layer deposition and freestanding microstructures releasing. 24
Figure 2.17 SEM image of an untethered electrostatic microrobot [122]. 32
Figure 2.18 The state transition diagram of the microrobot [122]. 32
Figure 2.19 Sample paths traversed by one of the micro-robots under teleoperated control [122]. 33
Figure 2.20 (a) Top-down schematic of four microrobots, A, B, C, and D, demonstrating coupled and decoupled motion. (b) A free body diagram of an anchored magnetic microrobot experiencing an electrostatic anchoring force [123]. 34
Figure 2.21 (a) Side view and top view SEM image of a standing microrobot. (b) Comparison of idealized impulse drive and inchworm walk. (c) and (d) Schematic and SEM images of forward motion and steering. Scale bar = 20 μm in (a) and 120 μm in (d) [124]. 35
Figure 2.22 (a) Nickel microrobot components and an assembled microrobot. (b) Schematic of microrobot steering actuation system. (c) Image of magnetic steering system [127]. 37

Figure 2.23 (a) Schematic of resonant magnetic microrobot actuation. (b) Microrobot design model and cross-section from A-A' shows the dimple feet [125]. 38
Figure 2.24 Electromagnetic system for the wireless control of microjets in three-dimensional space. Insets in the bottom right corner show a microjet moving towards a reference position (crosshair) under the influence of its propulsion force and the controlled magnetic fields. The upper left inset shows the propulsion mechanics of the microjet. The bottom left inset shows a reservoir for the hydrogen peroxide that contains microjets [142]. 39
Figure 3.1 (a) Fabrication process of freestanding two-dimensional magnetic micromagnets. (b) Scanning electron microscopy (SEM) images of micromagnets arrays. (c) SEM image of single 40mm thick micromagnet. Scale bars = 100 μm [121]. 44
Figure 3.2 (a) Optical microscopy image of patterned micromagnets. (b) Optical microscopy image of freestanding micromagnets released from substrate by dissolving sacrificial layer. All scale bars = 100 μm [121]. 45
Figure 3.3 Material thickness as a function of spin-coating speed for different mass ratios of magnetic microparticles. (a) 1000 rpm spin-coating speed. (b) 2000 rpm spin-coating speed. (c) 3000 rpm spin-coating speed. (d) 4000 rpm spin-coating speed. 47
Figure 3.4 Spin speed versus composite thickness for magnetic polymer composite using manufacturer's recommended exposure energy for corresponding thickness micromagnets [121]. 48
Figure 3.5 (a) Optimized UV exposure energy necessary for material crosslinking. (b) SEM images display rounding of corners inherent in material processing (left) and excessive rounding of corners and deterioration of edges due to UV overexposure (right) [121]. 50
Figure 3.6 Magnetic composite uniformity for different particle concentration and fabrication spin speeds. Histograms represent C values for samples at given processing parameters [121]. 52

Figure 4.1 Hybrid microrobots fabrication process: Microrobots were created by spin-coating a thin sacrificial layer onto a silicon wafer, followed by deposition and patterning of layers of SU-8, magnetic composite, and another layer of SU-8 [121]. 58

Figure 4.2 Hybrid microrobot microscopy images: (a) 3D profile of microrobot shown in (f); data obtained using scanning white light interferometry. (b)-(f) Optical microscopy images of hybrid microrobots; scale bar = 100 µm [121]. 59

Figure 4.3 Closed form solutions for surface parameters as a function of feature area fraction for asperity-covered surfaces [163]........ 66

Figure 4.4 Microrobot geometries of height h_1 = 45 µm (Square and Janus features) or h_1 = 40 µm (Crescent and C-Channel features). Each shape is patterned into an array with a unit cell length of L = 550 µm [161]. 67

Figure 4.5 Calculated and ideal surface parameters for photolithography patterned microrobot arrays [161]........ 69

Figure 4.6 Typical magnetization (B - H) Curve [173]. 72

Figure 4.7 Free body diagrams of magnetic microrobot in fluid environment. (a) When the permanent magnet is static and aligned with the microrobot. (b) When the permanent magnetic is moving with a velocity v and misaligned with the microrobot which causes a cogging force $\boldsymbol{Fcog}$. 75

Figure 4.8 (a) Magnetic microrobots control setup. (b) Enlarged schematic diagram of locations of the permanent magnet and microrobot. (c) Visualization of the magnetic field generated by a permanent cubic magnet. 77

Figure 4.9 Time-lapse images of “swimming” magnetic polymer microrobot powered by external magnetic field; the robot completed the course in 18 seconds following the line 30.5 mm in length. Scale bar = 2 mm [121]. 78

Figure 5.1 Flash formation in micromolding versus flash-free micromolding using AMM. 81

Figure 5.2 Final negative PDMS mold fabrication process and microscopy images. (a) Polymer mold copy fabrication process. (b) SEM image of original tungsten carbide negative master mold (provided by AMT Nano, LLC). (c) SEM

image of PDMS positive sister mold. (d) SEM image of PDMS final polymer mold copy. All scale bars = 100 μm.. 83

Figure 5.3 (a) SEM image of micromilled hemisphere cavity of original nickel mold [192]. (b, c) SEM images of freestanding SU8 three dimensional microhemisphere by AMM; sacle bars = 150 μm... 85

Figure 5.4 SEM images of original metal mold (left) [192] and SU-8 molded component with surrounding film (right); scale bars = 150 μm. 87

Figure 5.5 (a) SEM image of SU-8 with 2.49 mm^2/s kinetic viscosity micro-molded component with intentional film halo without force applied during pre-exposure baking. The scale bar = 150 μm. (b) Surface profile of SU-8 with 2.49 mm^2/s kinetic viscosity micro-molded component with intentional film halo without force applied during pre-exposure baking. (c) Film thickness vs. material viscosity with/without force during pre-exposure baking. 88

Figure 5.6 Solvent loss for AMM processing of SU-8 10 with/without applied force. 90

Chapter 1 Introduction

1.1 Background and Motivation

Micro-electro-mechanical systems (MEMS) technology has had an increasingly large impact on industry and our society. This technology is growing rapidly and its applications range from consumer electronics to the automotive industry, aeronautics and astronautics, pharmaceutics, health care, and bioengineering. MEMS technology has enabled a variety of innovative and improved products, like microphones [1], micro-gears [2, 3], micro- /bio- sensors/actuators [4-6], drug delivery devices [7], and disease diagnostic tools [8, 9].

MEMS devices typically consist of two dimensional and three dimensional microstructured components. Here the term "two dimensional" typically refers to microfabrication processes that deposit individual, thin films of material, such as most photolithography-based methods [10]. These two dimensional methods are normally used to fabricate structural layers or bases for MEMS applications [11]; and it can only be used for very limited three dimensional fabrication. Multiple layers of material can be deposited in a way that makes quasi-3D stair-stepped structures [12], but it is usually very difficult to create arbitrary three-dimensional geometry. "Three-dimensional" typically means the creation of three dimensional microstructures with arbitrary out-of-plane geometry, including curvature—such as a hemisphere—not just the stacking of flat layers. There is high demand for three dimensional microfabrication process to mass produce defect-free three dimensional microfeatures with various materials and geometries.

Although there are many current MEMS three dimensional fabrication methods, most suffer from some major limitations. As mentioned in the previous paragraph, one of the most established microfabrication methods—photolithography based processing,

originally developed for integrated circuit fabrication—excels in the area of precision but is fundamentally limited to creating 2D features [13] . A variety of 3D microprototyping methods have recently been demonstrated [14-16], but these have limitations in feature resolution, throughput, quality, and material types that can be processed. Inclined UV lithography with micromolding can yield some specific three dimensional microstructures [17], but it is impossible to fabricate three dimensional microstructures with curvature. Roll-to-roll micro- and nanofabrication excel in high-throughput production [18-20], but it is challenging to create freestanding microcomponents with this fabrication method, and there are limitations to the material types than can be processed.

New fabrication methods are needed in order to expand material choices for microfabrication, create true three-dimensional microstructure geometry, enable high-throughput micromanufacturing, and reduce cost. An ideal microfabrication process would allow the user to incorporate various materials into a single component, allowing them to take advantage of different physical, magnetic, electrical and chemical properties at the microscale. This ability could create new opportunities to improve and invent new classes of MEMS devices with unique functionalities.

In this thesis, a facile microfabrication method was developed for freestanding 2D polymer micromagnets that can be utilized in MEMS, microfluidics, microrobotics applications. Micromagnets can be photopatterned by integrating magnetic particles with standard UV photolithography. The method was capable of fabricating polymer micromagnets with 3 μm feature resolution and greater than 10:1 aspect ratio. It was found that the magnetic particles within the polymer matrix were possible to be dispersed uniformly by modulating spin speed during fabrication without requiring chemical modification of either of the two composite components. Also, freestanding micromagnets with encapsulated magnetic cores were fabricated utilizing this method and multilayer photolithography. The micromagnets were magnetically actuated in isopropanol alcohol along a desired path and achieved an average speed of 1.7 mm/s, demonstrating that these micromagnets could be remotely controlled with high accuracy in a liquid environment.

In addition, a method was created to produce freestanding microstructures with controllable 3D geometry. This method, called Aligned Mask Micromolding uses a combination of selective UV exposure through a photomask, polymer micromolding, and soft lithography to generate 3D microscale components without unwanted connecting "film". This method was optimized with respect to processing parameters, such as material viscosity, solvent concentration and molding pressure, and ultimately the method was used to demonstrate the creation of freestanding hemispherical microscale structures.

1.2 Dissertation Organization

The main theme of this dissertation is development of two new microstructures fabrication methods: first, a method for integrating magnetically responsive regions into microstructures using photolithography, and second, a method for creating three-dimensional freestanding microstructures using a modified micromolding technique. The first method is a facile method of producing inexpensive freestanding photopatternable polymer micromagnets composed NdFeB microparticles dispersed in SU-8 photoresist. This method was used to demonstrate the creation of freestanding microrobots with an encapsulated magnetic core. A magnetic control system was developed and the magnetic microrobots were moved along a desired path at an average speed of 1.7 mm/s in a fluid environment under the presence of external magnetic field. A microfabrication process using aligned mask micromolding and soft lithography was also developed for creating freestanding microstructures with true 3D geometry. The combination of these two microfabrication methods has great potential for integrating several material types into one microstructure for a variety of applications. The dissertation consists of 6 chapters the content of each chapter is summarized as below:

- Chapter 1 provides a brief introduction of MEMS fabrication methods and the current limitations of these methods.
- Chapter 2 systematically reviews the current research work that has been performed by other researchers on freestanding microstructure fabrication, three

dimensional microstructure fabrication, magnetic microstructure fabrication, and wireless control of magnetic microstructures in an external magnetic field.

- Chapter 3 demonstrates the novel fabrication method developed for freestanding magnetic microstructures using NdFeB nanoparticles and SU-8 photoresist. Micromagnets are photopatterned by integrating the magnetic particles with standard UV photolithography. Characterization of the process, the nanocomposite, and the microstructures are presented.
- Chapter 4 presents a method for creating "hybrid" magnetic microstructures with ferromagnetic regions. The "hybrid" magnetic microstructures are fabricated by photopatterning two layers of SU-8 photoresist with one inserted magnetic composite layer. This method is used to create microrobotic structures that are then actuated in an aqueous environment using an external magnetic field.
- Chapter 5 focuses on the development of a high throughput, low-cost microfabrication method for creating arbitrary three-dimensional microstructures. The freestanding film-free 3D microstructures are fabricated by selectively exposing the material inside the cavities to UV light, combining soft lithography, photolithography, and micromolding.
- Chapter 6 summarizes the work presented in the dissertation and provides recommendations for future work.

Chapter 2 Literature Review

The microfabrication processes used in MEMS technology were originally developed for the integrated circuit (IC) industry [13], which can be traced back to 1954 when the first IC was built with germanium (Ge) by Texas Instruments. In 1956, the piezoresistive effect in Ge and Silicon (Si) was discovered and measured in the Bell Telephone Laboratory [21, 22]. It was found that Ge and Si had the potential to produce strain gauges with a gauge factor (i.e., instrument sensitivity) 10 to 20 times greater than those based on metal films [21-23].

Since then, miniaturization had become faster in order to keep pace with the increasing complexity of integrated circuits. This phenomenon followed Moore's Law, named after Gordon E. Moore, co-founder of Intel Corporation. Moore described an observation in 1965 that the number of transistors in a dense integrated circuit doubled approximately every two years. This trend has proven to still be accurate today [21-23]. In the almost fifty years since this observation, the IC industry has grown exponentially and had an increasing impact on our daily life. Now IC chips with features tens of nanometers are becoming commercially available and the scaling process is still continuing.

The same microfabrication technology that has enabled increasingly smaller ICs has also been used to fabricate MEMS devices. Because MEMS was derived from IC industry processes, it includes conventional IC process technology and materials, like film growth, doping, etching, dicing, and packaging [24]. Other MEMS fabrication techniques that are unique from IC methods have evolved as well, including bulk micromachining, surface micromachining, and micromolding [25, 26]. Bulk micromachining is a method of fabricating MEMS using etching techniques to sculpt MEMS features on silicon substrate. Surface micromachining enables producing complex micro-components for various MEMS applications. Unlike bulk micromachining, surface

micromachining uses a silicon substrate just as a mechanical support and fabricates microfeatures by deposition, patterning layers on the substrate and chemically removing sacrificial layers. The remaining layers are regarded as structural layers, which form the desired micro-components. Micromolding enables microstructures to be cast from master micromolds, which are typically prepared by bulk micromachining.

One of the most popular micromolding processes is the LIGA process. LIGA is a German acronym that stands for lithography (lithographie), electrodeposition (galvanoformung), and molding (abformung) [13]. There are two main LIGA fabrication technologies, X-ray LIGA and UV LIGA. X-ray LIGA was first developed by Becker, et al. [27] in the Research Karlsruhe, Germany in the 1980's. This method uses X-rays produced by a synchrotron to create high-aspect ratio structures in X-ray sensitive polymer photoresist, typically PMMA, bonded to an electrically conductive substrate. But because it requires a rare and expensive synchrotron source, X-ray LIGA has not been utilized in large-scale industrial applications [24, 28].

In the 1990's, UV LIGA was developed by Frazier [29]. UV LIGA is a more accessible, lower cost LIGA technology that can be used to create structures with relatively low aspect ratios using ultraviolet light [29, 30]. The first step in this microfabrication process is called UV photolithography [31, 32]; this process fabricates microfeatures in a light-sensitive chemical material called "photoresist" by using light to transfer a geometric pattern from a photomask. As shown in Figure 2.1, the typical UV photolithography process starts with spincoating a layer of photoresist onto a flat substrate. Then the photoresist is exposed to UV light through a patterned photomask, followed by hard baking and development processes.

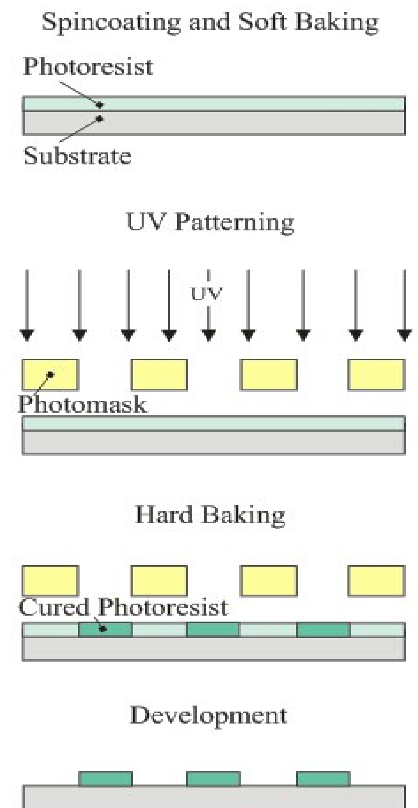

Figure 2.1 Typical UV photolithography fabrication process.

A wide variety of materials have been used in MEMS fabrication. In the early development of MEMS, manufacturing processes were based on those used by the IC industry, so silicon was the first material used to fabricate an engineered large-scale MEMS device in 1960's [33, 34]. MEMS relied heavily on silicon as the primary material for decades, prompted largely by silicon's excellent mechanical and electrical properties, low cost, and high availability. But in the past few decades, the variety of materials used has broadened through the development of new fabrication process based on wider range of materials, like metals [17, 35-38], ceramics [39], and polymers [11, 40, 41].

One of the most widely used polymer materials in MEMS fabrication is SU8, an epoxy-based negative tone photoresist [42]. Various SU8 formulations are commercially available from MicroChem®, which can be used to make features ranging from less than

1 micrometer tall to several hundred micrometers tall using a single spin-coating process [30, 43]. SU8 photoresist consists of a multifunctional, highly branched polymeric epoxy resin dissolved in an organic solvent (GBL, gamma-butyrolacton), and a photoacid generator (PAG) [44]. An "idealized" SU-8 molecule with epoxy groups is shown in Figure 2.2. An average single molecule contains eight epoxy groups, hence the "8" in SU-8.

Figure 2.2 "Idealized" SU8 molecule with epoxy groups [45].

When SU8 photoresist is exposed to UV light, the photoacid generator decomposes to form H^+A^- (hexafluoroantimonic acid) and reacts with the epoxides in a series of cross-linking reaction during a post-UV-exposure heating step [46, 47]. The photoacid acts as a catalyst during the SU8 crosslinking process, and it is only generated in the irradiate regions, so only the SU8 in the UV exposed region will become cross-linked. Because of its low cost, good mechanical, thermal, and chemical stability, SU8 has become a very popular material for microstructure fabrication. SU8-based technology has been gaining in popularity in MEMS products; a wide range of MEMS devices fabricated primarily using SU8 have been demonstrated [11, 41].

2.1 Freestanding Microstructure Fabrication

Freestanding means independent, standing alone or on its own foundation free of support or attachment according to Merriam-Webster dictionary. Freestanding microstructures are the microstructures which are not relying on or linked to anything else, including substrates and other microparts. Freestanding microstructures compose MEMS devices and implement the MEMS applications [38]. Especially for today's complex functional MEMS applications, fabrication of freestanding microcomponents, from one dimensional, two dimensional, to three dimensional, is the fundamental issue of producing MEMS devices. Diverse techniques were developed to fabricate microstructures with semiconductors, metal, ceramic and polymers [13, 48-50]. Current freestanding microstructures fabrication methods are numerous, from conventional photolithography, reactive-ion etching (RIE), to soft molding and dry and wet etching, etc. Processing materials are also various, like SU8 photoresist, Polydimethylsiloxane (PDMS), photonic polymer, etc.

2.1.1 Freestanding One- and Two- dimensional Microstructure Fabrication

In MEMS field, one-dimensional (1D) microstructures always refer to the microfeatures with great length/width ratio, usually in hundreds magnitude, like capillary micro channels [51]. Two-dimensional (2D) microstructures are normally defined as one-layer simple geometries fabricated through one step photolithography, like cube, cuboid, etc.

Photolithography patterning is a conventional method to fabricate freestanding microstructure, which are mostly one- and two- dimensional microstructures. Hiroshi Ito [52] and Y. Tang group [53, 54] represented using typical photolithography to produce freestanding micro-features with SU-8 photoresist. Zhigang Zhu, et al. [55] used soft lithography to fabricate freestanding microgear with aluminia. Capillary force lithography was also developed from soft lithography to fabricate microstructures, the soft mold cavities were filled with processing materials by capillary force driven. E. Kim,

et al.[56], and K. Y. Suh and H. H. Lee [57] used this method and fabricated large-scale microstructures by placing PDMS mold on polymer film and then heating above the glass-transition temperature of the polymer. But in these studies, PDMS was primarily used as a soft mold for creating patterns of other materials on various substrates. Jagannathan Rajagopalan and M. Taher A. Saif [51] used similar principle, capillary driven flow through micro channels, to create long, freestanding PDMS microstructures for use in biomechanical study and as platform for bio-devices.

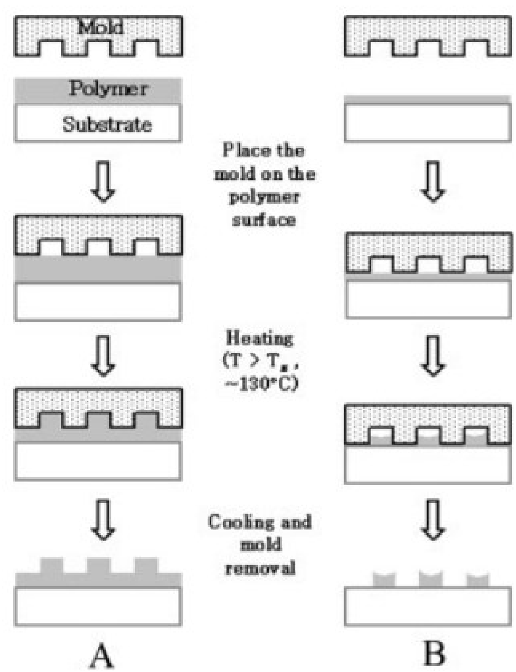

Figure 2.3 Schematic diagram of capillary force lithography. (A) When the film is relatively thick with respect to the mold's step height; (b) when it is relatively thin [58].

Those methods summarized previously can only produce simple 2D geometric microstructures, like cuboid, cylinder, or anything can be vertically extruded from a 2D shape. These simple micro-components couldn't meet the development of MEMS applications. Complex MEMS components were needed for advanced MEMS devices and numerous microfabrication for complex freestanding microstructures were developed. Benjamin Bohl, et al., and Jung A. Lee, et al., improved the traditional photolithography to multi- spincoat and expose SU-8 layers to obtain complex microstructures, such as microfluidic devices [59] and 3D carbon microstructures [40]. But all these multilayers

microstructures fabrication method can only succeed in microstructures with smaller top layers and larger bottom layers.

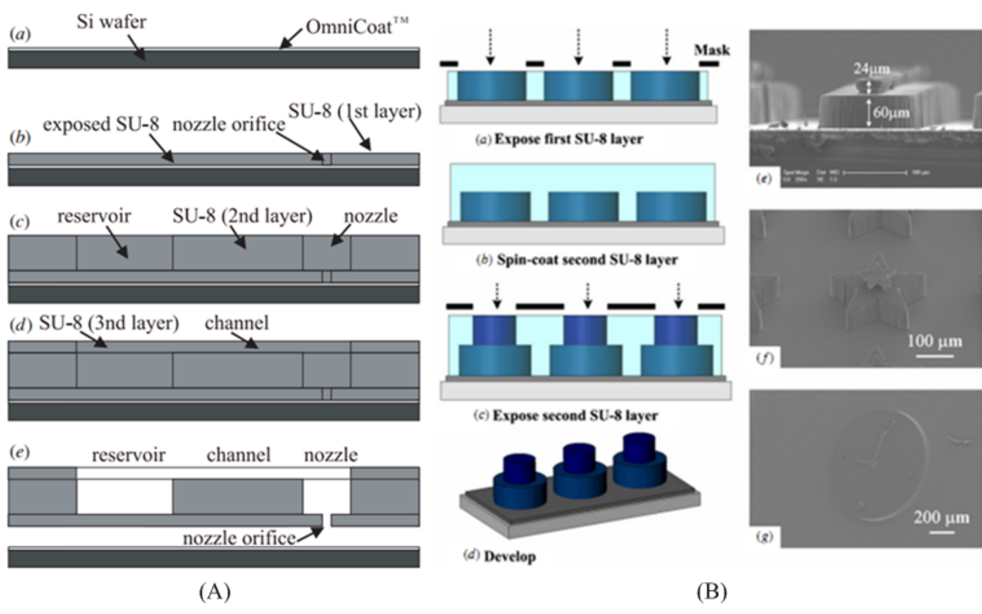

Figure 2.4 (A) Description of the SU-8 lift-off process for the fabrication of the DWP [61]. (B) Fabrication process for multi-level SU-8 microstructures (left) and examples of fabricated SU-8 microstructures (Right) [40].

Frederik Ceyssens and Robert Puers [60] improved multi- spincoating and exposing SU-8 layers to fabrication any-sized multi-layered microstructures. They exposed one SU-8 layer with different photo masks and 365 nm and 313 nm UV lights to fabricate freestanding micro-cantilever. This method saves processing time on reducing multiple SU-8 layers spincoating and baking to only one layer compared to Benjamin Bohl [59]. However, switching UV light during exposure experiments is inconvenient and both the UV lights are not easy accessible. Further, B E J Alderman, et al. and Frederik Ceyssens, et al. evaporated a thin aluminum masking layer to block UV light and just using 365 nm UV light expose another SU-8 layer to realize the freestanding micro-cantilever [60, 61]. But the evaporation process can elevated the temperature or leak small amount of UV radiation from the white-hot filament. This would crosslink the unwanted SU-8 and cause development problem. Yun-Ju Chuang et al. demonstrated a microfabrication which can avoid using different UV lights and the embedded blocking mask, but still can fabricate

any-sized multi-layered microstructures through controlling the exposing energy [62]. However, this method still has limitation on precisely dosage control, which might be a reason for their low quality sidewalls.

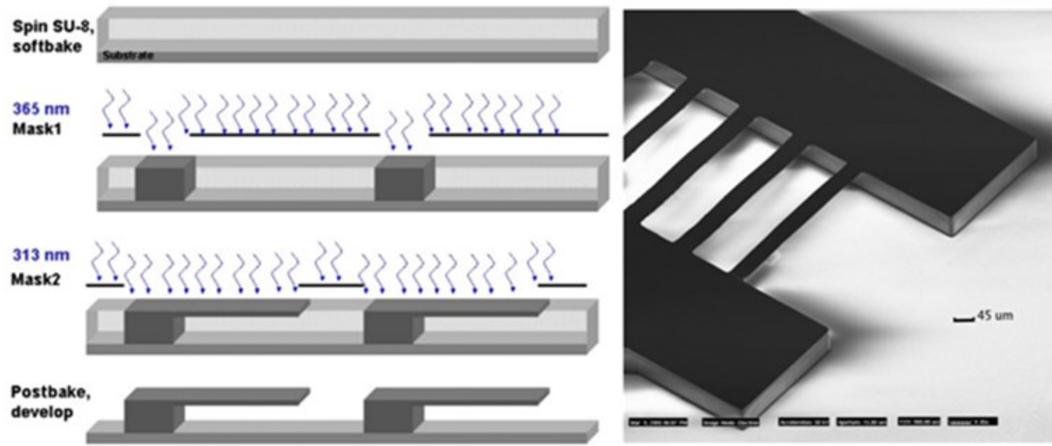

Figure 2.5 The 313 nm absorption method (left); SEM image of clamp structure made by the method (right) [60].

Although the microcomponents mentioned in the previous section are physically three-dimensional, they are microfabricated using stacking layer-by-layer fabrication methods and limited to flat, layered geometries. These kinds of microstructures are called two-and-half-dimensional (2.5D) microstructures instead of true three-dimensional microstructure in MEMS field [10].

2.1.2 Freestanding Three-dimensional Microstructres Fabrication

As the development of MEMS applications, new micro-devices need complex true three-dimensional microstructures fabricated with diverse materials. For example, microengine, micropump, micro-medical devices, etc., they are complex and cannot be constructed by multi-layered microstructures fabrication methods. To date, numerous microfabrication methods have been developed to produce complicated true three-dimensional microstructures. Real three-dimensional micromanufacturing processes can be classified into two main groups, including comprehensive 3D microfabrication

techniques which can be employed for arbitrary geometric shape microparts, and specialized 3D microfabrication methods which are developed for specific functional and geometric microstructures.

Comprehensive 3D microfabrication methods include gray-scale lithography, dynamic projection microstereolithography, two-photon polymerization, and pixels exposed lithography. These microfabrication processes are considered as promising approaches for real 3D microstructures fabrication and can be utilized into create complex 1D, 2D, and 3D microcomponents.

Gray-scale lithography is a one-step lithography process using gray-scaled photomask exposing photoresist to create gradient height microstructures. Due to the different amount of UV intensity passing through the optical mask, excessive photoresist are developed away after the exposure; hence, arbitrary geometric microstructrues are obtained.

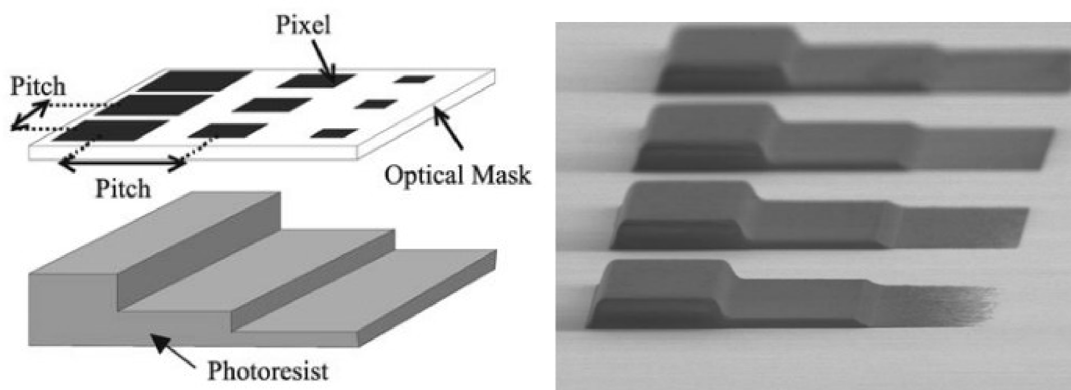

Figure 2.6 (a) Example of a three-level gray-scale mask pattern and the resulting photoresist structure. (b) Three gray levels patterned in AZ 4620 photoresist resulting from a similar mask pattern [63].

Pakorn Preechaburana and Daniel Filippini [64] utilized the gray-scale lithography principle and designed photomask with 8-bit gray level illuminating patterns with single pixel resolution. And photoresist was exposed with varying gray-scale level pattern and the heights of the developed microstructures were measured. A relation between gray-

scale intensity and microstructures thicknesses is found and used to calibrate the illuminating patterns to compensate for the nonlinear development process of photoresist and yield real three-dimensional microcomponents.

Christopher M Waits, et al [63, 65] investigated the relation between gray level numbers, minimum pixel size, and the increment between subsequent pixel size used to create the gray-scaled photomask, and the resolution and magnification of the projection lithography system. It was found out that an approximate minimum pixel size can be estimated by

$$w_{min} = P - \sqrt{\frac{P_C^2}{2}} \qquad 2.1$$

where w_{min} is the minimum pixel width, P is the pitch chosen for the mask and P_C is the system resolution as shown in Figure 2.5. The maximum pixel size could be as large as the pitch. The minimum and maximum pixel size could set up the number of gray level numbers; furthermore, the size and surface quality of desired microstructures are determined by the gray levels. The more gray levels the mask has and the smaller the pixel size is, the smoother the fabricated microstructures are.

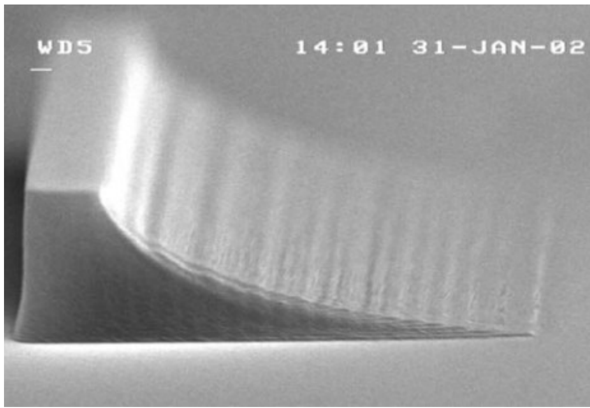

Figure 2.7 SEM image showing developed AZ 4620 photoresist using a 3.5 μm pitch and one row per pixel size [63].

Microstereolithography is a three-dimensional printing technology for fabricating micro-scale size structures by UV or other power source drawing the object onto the surface of liquid photoresist layer by layer [66]. Microstereolithography has two types, one is a scanning-based method in which the power source scans the photoresist resin surface according to sliced layers, and the other is projection-based process where the pattern of a sliced section is focused on the resin surface at one time [15].

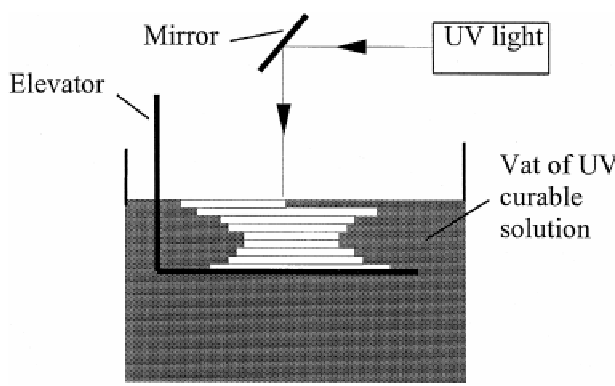

Figure 2.8 The principle of scanning-based microstereolithography [15].

The principle to produce three-dimensional microstructures by scanning-based microstereolithography is shown in Figure 2.7. First, a 3D solid model need to be designed with computer-aided-design (CAD) software and sliced into a series of 2D layers with uniform thickness. The numerical controllable code generated from each sliced 2D layer is then executed to control a motorized x–y stage carrying a vat of liquid photoresist. The focused scanning UV beam is used to expose the photoresist according to the sliced layers. A layer is solidified and the elevator moves downward and a new layer is formed. As a result, with the synchronized x–y scanning and the Z-axis motion, the complicated three-dimensional microstructure is constructed. X. Zhang, et al.[15] focused UV beam to 1-2 μm to expose a thin layer of 1-10 μm in thickness. The fine UV beam and the small z-directional translation enabled precise fabrication of real three-dimensional microstructures, like microgear and microcone, with 1.2 μm resolution. However, the process was really time-consuming, which can be as long as couples of hours. In this situation, the projection-based microstereolithography was developed.

The projection-based microstereolithography can significantly reduce processing time by exposing one layer pattern instead of scanning exposing threads on one layer in scanning-based microstereolithography. The projection-based microstereolithography also need create 3D model and slice into 2D layers. The 2D layers data need to be converted into binary images to create the patterns. Each layer is exposed by a certain time by focusing the light pattern onto the resin surface. The solidified layer is immersed deeper and the fresh resin flows on top of the previously fabricated layer. The 3D structure is produced by repeating these steps for the required number of layers.

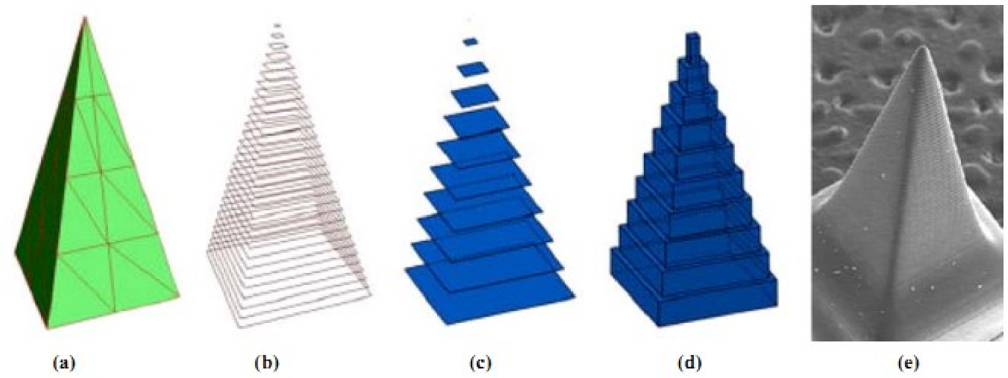

Figure 2.9 Scanning-based micrpstereolithography processes to produce 3D microstructures: (a) 3D STL model; (b) sliced 2D sections; (c) binary images; (d) stacking; (e) final structure [67].

Jae-Won Choi, et al. [67] and Pranav Soman, et al. [68] used a digital micromirror device (DMD) to generate 2D patterns from the binary images converted form sliced 2D layers, which realized the projection-based microstereolithography. The light was filter at 365 nm and through a collimating two-convex lens set; and then was projected to the DMD by LightGate. The reflected light traveled through tube lens to keep collimated. DMD consists of almost one million mirrors and each one can be controlled independently according to the pattern information created by the binary images from the sliced layers. These patterned lights were focused on the resin surface and the layer with desired pattern is polymerized. As a result, the final real 3D microstructure was constructed. The DMD-based microstereolithography method increased the resolution limits. It can achieve producing real three-dimensional microstructures with 10 μm depth

resolution and 1μm fabrication precision. The DMD-based microstereolithography method also enabled layer exposure and reduced process time from hours to tens of minutes as compared to scanning-based microstereolithography.

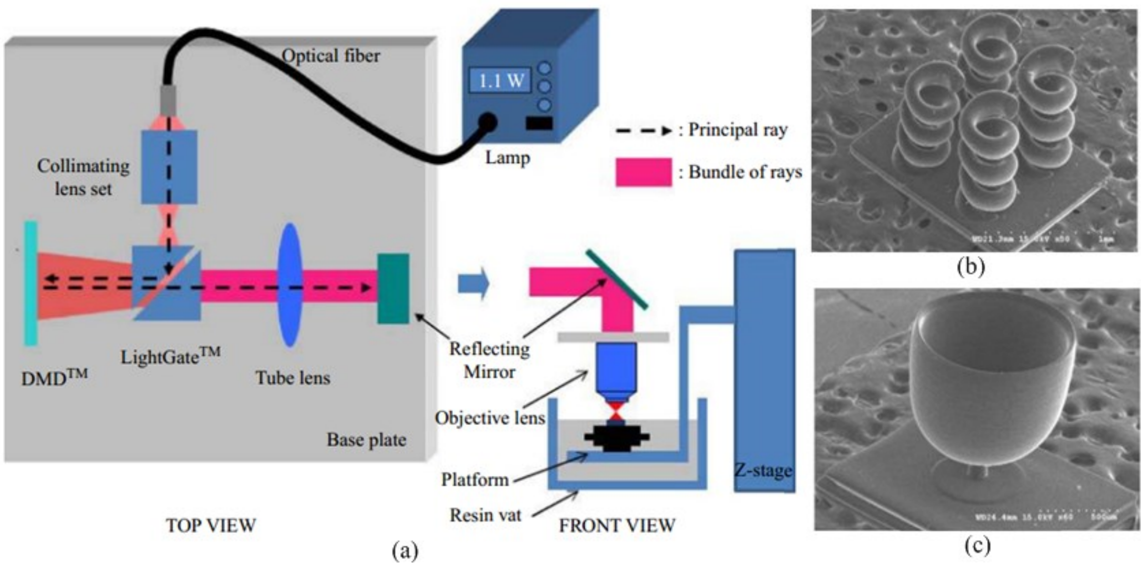

Figure 2.10 (a) Schematic diagram of DMD-based microstereolithography system. SEM images of complex 3D microstructures with down-facing surfaces successfully fabricated using MSL and cure depth control: (b) 4 micro-springs and (c) micro-wineglass [67].

Another promising comprehensive three-dimensional microfabrication method is two-photon polymerization (TPP), which can create microstructures with higher resolution compared to other methods. TPP enables resin absorbing two-photon at longer wavelength, usually in red-near-infrared (NIR) region, instead of one-photon absorption in conventional prototyping microfabrication. The desired shape of the photoresist is irradiated directly from inside by laser and the outside material is kept from contaminated. After washing out the outer resin, the desired geometry 3D microstructure is obtained by solidifying the inner volume [69-72].

Shuhui Wu, et al. [73, 74] utilized TPP and attained complex three-dimensional microfeatures with 150 nm resolution. A 3D micro-scale Venus model with closed surface was built by CAD software and converted to a surface model with triangles where all adjacent triangles share two common vertices. Then the surface model was sliced into

layers with closed contour. The thickness of each layer was determined by the focal length of the laser. The contour patterns were irradiated and the 3D microstructure's shell was attained. Then the surrounding material was washed and the inner part was exposed by UV light. The Venus microfeature was fabricated in 5 minutes by TPP microfabriction method, which is significantly more efficient than microstereolithography microfabrication.

Florian Formanek, et al. [75] used TPP microfabrication technique combined with selective metal deposition by electroless plating (EP) to obtain complex three-dimensional metallic microstructures. The selective coating was achieved by modifying the chemical property of the polymer and the substrate. Desired geometry 3D microstructures were initially fabricated by TPP microfabrication on hydrophobic treated glass substrate by dimethyldichlorosilane (DMDCS) [76]. The fabricated microfeatures were pretreated by $SnCl_2$ to increase the metal deposition and adhesion; then coated with silver by EP. Samples were washed and metallic microstructures were attained. This method enables uniform large area metal deposition in ambient conditions compared to electron-beam writing or focused-ion-beam chemical vapor deposition, which makes it perfect for insulating microstructures.

Pixels exposed lithography (PEL) for arbitrary three-dimensional microstructures fabrication was devised by Mitsuhiro Horade and Susumu Sugiyama [77] in 2010, PEL employed synchrotron radiation (SR) light energy distribution by a pixel-scaled pattern created function instead of conventional photomask used in photolithography. The desired microfeatures can be fabricated layer by layer and each layer pattern is polymerized by SR light exposing selected pixels by the pattern function. The schematic of PEL is shown in Figure 2.9.

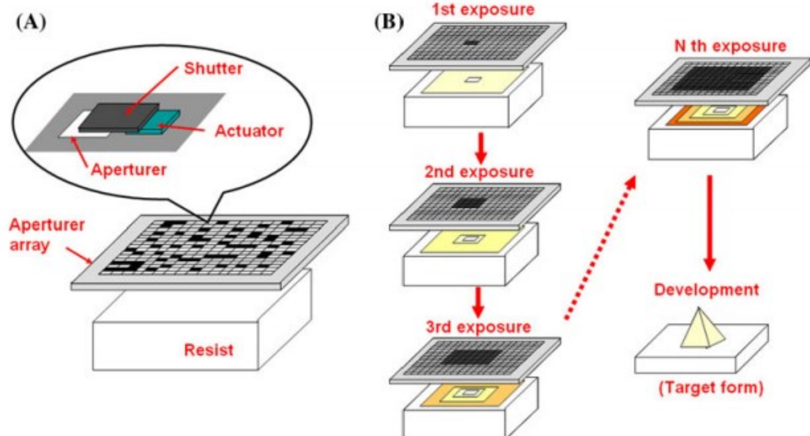

Figure 2.11 Outline of 3-D method of fabrication based on pixels exposed lithography. (A) Concept underlying this method, using the mask with pattern created function where SR light is shaped by aperture, and amount of exposure energy is controlled by closing and opening aperture with actuator; (B) using the mask with pattern created function to apply mosaicked energy distribution to resist surface [77].

It was also investigated that the pixel size could be made smaller than the aperture size by overlapping adjoining pixels to fabricate finer microfeatures. A 3D microstructures was created by x-y function:

$$Depth(x,y) = -50[1 - \sin(x \times y)] - 20 \qquad 2.2$$

and it was derived and visualized as shown in Figure 2.10 (a). This desired microstructure was fabricated using the PEL with different pixel sizes by overlapping as in Figure 2.10 (b) and (c).

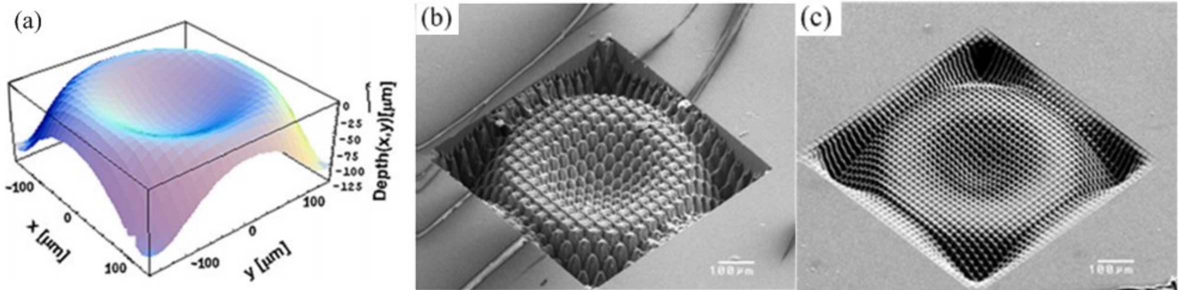

Figure 2.12 (a) 3D microstructure derived from Equation 2.2. (b) 3D microstructures fabricated by overlapping ½ aperture size. (c) 3D microstructures fabricated by overlapping ¼ aperture size [77].

PEL microfabrication method can arbitrary 3D microstructures and reduces process time and cost compared to conventional techniques since photomask is not needed for fabrication and alignments are not avoided during the process.

Specialized 3D microfabrication methods are created for specific functional or geometric 3D; and hence, there are diverse specialized 3D microfabrication methods designed for specific function al and geometric 3D microcomponents, including drawing lithography UHAR microneedles, electrodes glass ball molding for spherical bowl, and self-scrolling method for helical microstructures. Here, just a few of these methods are introduced. Unlike comprehensive 3D microfabrication methods, these methods cannot apply to arbitrary 3D microstructures fabrication.

Kwang Lee, et al. [78] proposed an additive microfabrication method to creat ultra high-aspect-ratio (UHAR) 3D microstructures without the need for a conventional photomask, in which thermosetting polymer was drawn directly from a 2D pattern to produce UHAR microneedles; hence, this method is called “drawing lithography”. SU8 2050 was sued because its photoresistant properties are easily controlled with temperature and enables the precise control of drawing and microstructure formation. Photoresist was spincoated on substrate and arrays of 200μm diameter, 3mm long pillars on PDMS frame contacted the SU8. Simultaneously the drawing lithography was performed and it caused conical-shaped bridges between the substrate and the pillars. After polymerized the bridges, a second drawing separated the bridges and yielded

microneedles. Then chemical treatment and metallic coating conducted and then 3D UHAR (100:1) hollow metallic microneedles were obtained.

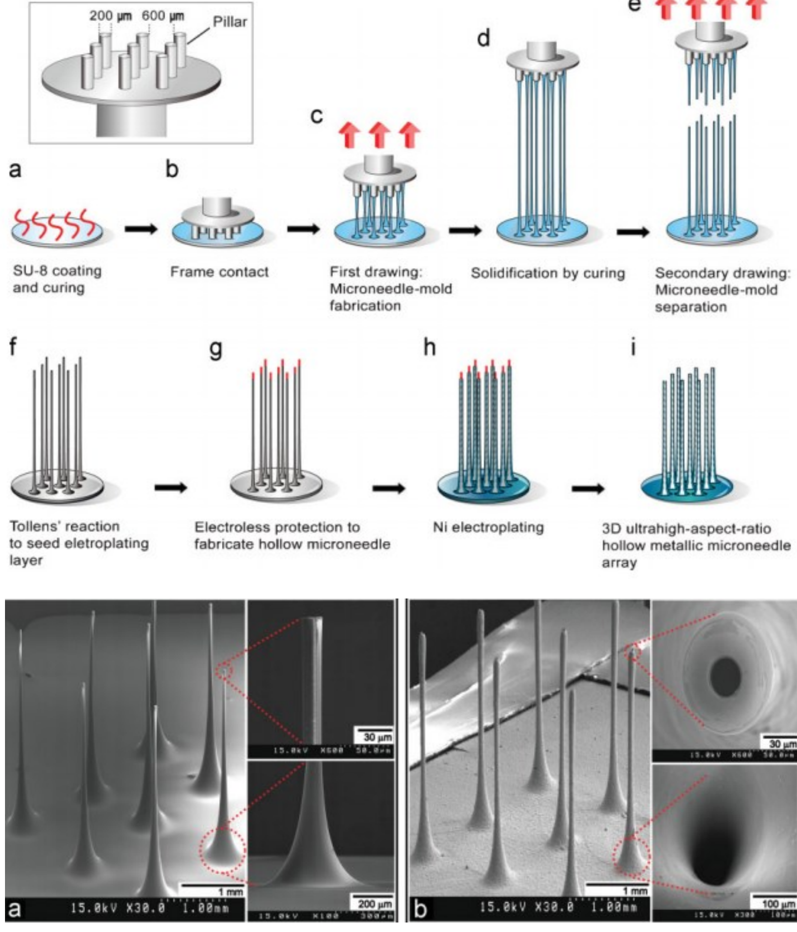

Figure 2.13 Schematic of microneedles fabriacation by “drawn lithography” and SEM images of the microneedles [78].

Md Mahbubur Rahman, et al. [79] developed a new fabrication method for a hemispherical microbowl shape 3D microstructure with glass ball molding as well as a self-guided-alignment process to maintain the gap distance between the electrodes and the shell uniform. The electrodes were first fabricated with tall enough (~ 700 µm) thickness to provide 3D microbowl height. A thin patterned wafer was prepared by DRIE and bonded with a thick wafer with metal etch stopper to form a fusion bonded wafer. A contact layer was deposited on another glass substrate with Ti/Pt and bonded with the fusion bonded wafer. Two steps of DRIE were conducted to create the electrodes and a

pre-manufactured ultra-low expansion (ULE) glass ball mold with pre-coated polysilicon (3 μm) was placed in the gap among all electrodes. Then Ar plasma etching was used to remove the top half of the sphere and the bottom half was left and the microbowl was attained.

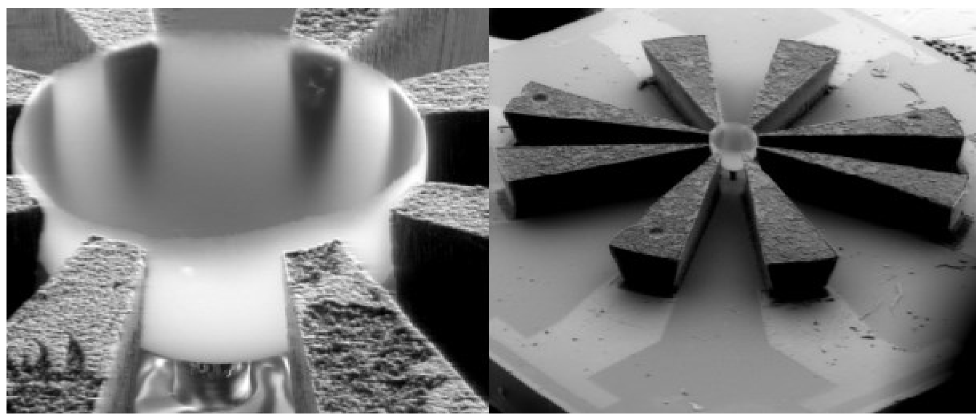

Figure 2.14 Fabricated microbowl (left) and eight electrodes after the ball bearing release (right) [79].

Nelson et al. [80-82] reported a microfabrication method based on the self-scrolling to fabricate helical microstructures as shown in Figure 2.13 (a). Two or three thin film layers of stripes were fabricated and a square nickel head was deposited. And wet etching enabled the stripes curled into helices due to the internal stress of the thin material layers. These helices size can be control by the thicknesses and width of the stripes and the square by adjusting the lithography and nickel deposition. A. Ghosh and P. Fischer [83] proposed another method to fabricate helices by glancing angle deposition (GLAD). The helices pillars using magnetic polymer were fabricated on spherical seeds on controlled platform in magnetic field. The magnetic force enabled the pillars curled to controlled direction and the platform rotation determined the helical feature.

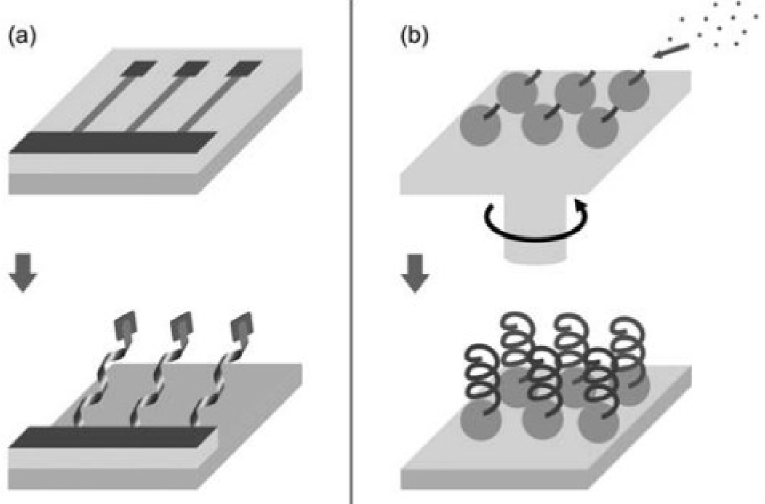

Figure 2.15 (a) Self-scrolling method for ABF fabrication. Bi- or tri-layered thin-film ribbons and a square nickel head are grown and deposited, respectively. After wet-etching, the ribbons curl into helices in a controlled manner. (b) GLAD fabricated helices. Pillars are deposited at an angle and under constant rotation of the stage, resulting in helices on the spherical seeds [84] .

The helical microstructures can also be fabricated by comprehensive 3D microfabrication methods, like microstereolithography, two-photon technique. But these specialized fabrication methods are more time and cost efficient. Moreover, these methods can realize mass production of the 3D microstructures, which is key feature for applying applications into industry.

All these microfabrication methods demonstrated previously can produce freestanding microstructures on substrate but not releasable for assembling into MEMS devices and implement the applications. Therefore, the release of the finalized MEMS microstructures is a key step in the fabrication process of MEMS applications [85].

2.1.3 Freestanding Microstructures Release Techniques

To significantly enhance those microfabrication methods for freestanding microstructures and their applications, two techniques need to be developed: an easy to use sacrificial layer, and a releasing technique to fabricate complex multilayer structures [86, 87]. The sacrificial layer concept was first mentioned by H. C. Nathanson1 and R. A.

Wickstrom1 [88] and the releasing technique came out corresponding to sacrificial layer. Sacrificial layer is a layer of material deposited between structural layers for mechanical separation and isolation and can be removed during the release etch to free the structural layers and to allow mechanical devices to move relative to the substrate [21]. The release step brings some difficulty since cross-linked SU-8 or other photoresist is very hard to release/remove and may be a time-consuming step and affect the integrity of the microstructures during this process. Another difficulty is the difference of the coefficient of thermal expansion (CTE) between standard substrate materials and fabrication materials. For instant, SU-8 has a high CTE [89] so this difference causes relatively high stresses to the structures, making SU-8 films to crack [90]. Currently various methods for fabricating sacrificial layer and releasing microfeatures are reported as summarized later in this section. The schematic of general sacrificial layer fabrication and release is shown in Figure 2.14.

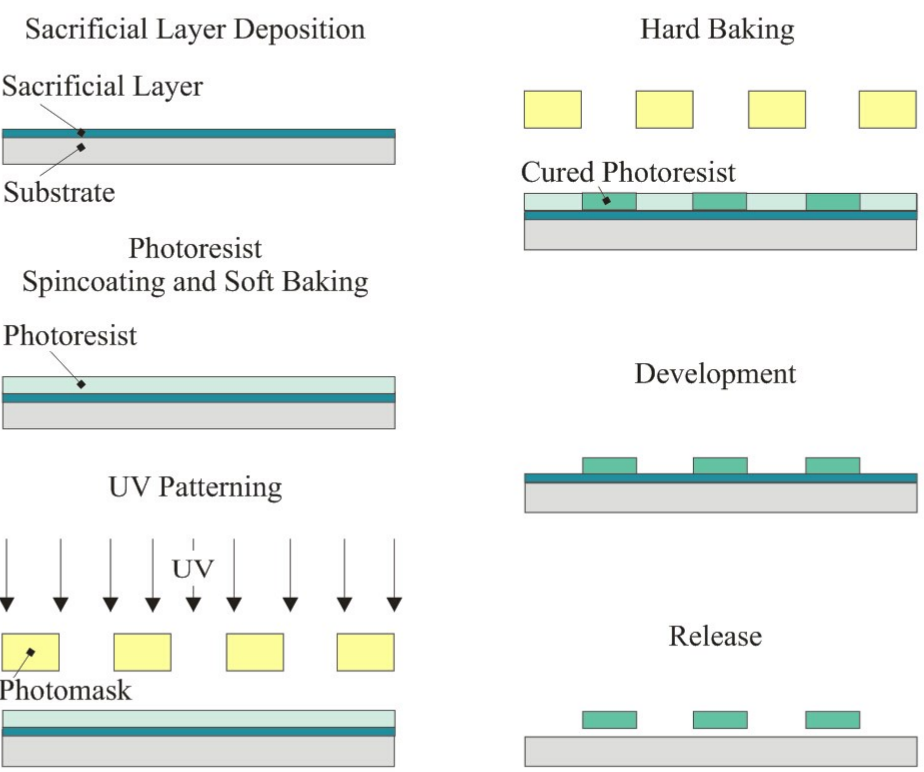

Figure 2.16 Schematic of general sacrificial layer deposition and freestanding microstructures releasing.

Omnicoat (MicroChem®) and polyimide are the most common used sacrificial layers materials [91]. OmniCoat is from the line of the Polydimethylglutarimide (PMGI) resists with proprietary solvent blends. It has many advantages to be a sacrificial layer material. It is optically transparent and only tens nanometers thick to apply on substrate. More important, Omnicoat is readily soluble in most standard alkaline photoresist developers and has highly controllable dissolution properties. It is a simple, easy, and fast apply and release method.

Sarah L Ta, et al. [92], Luciana Wasnievski da Silva, et al. [93], Sotiria D. Psoma and Derek W.K. Jenkins [94], D.E. Pesante, et al. [85] spun Omnicoat at 3000 rpm and yield an approximate 13 nm sacrificial layer to facilitate microstructures removal. A Bagolini, et al. [95] selected PI2610 polyimide as their sacrificial layer material since they needed spin-on polyimides which are IC process compatible, can withstand as high as 400 ^{o}C and can be dry etching in conventional equipment. Polyimide was spun on wafer with a thickness of 2-4 µm; followed by hard baking in N_2 environment at a temperature of 400 ^{o}C for 30 min. Javaneh Boroumand Azad [96] proposed the longer polyimide was baked, the harder to remove it. They chose ProLift 100 (Brewer Science®) because they found out it was not only soluble in positive photoresist, but also in negative photoresist which have TMAH base, such as MF319, RD6, etc. Polyimide 115a (Fujifilm) was used by Benjamin Mimoun et al. [97] to form a sacrificial layer by spincoating 15 s at 350rpm and 45 s at 1000 rpm; following soft-baked at 120 ^{o}C for 6 minutes and hard-baked polyimide in a N_2 environment at a temperature of 400 ^{o}C for 2 hours, which yielded a 10 µm thick polyimide sacrificial layer.

Besides Omnicoat and polyimide, Cu, Al, and Cr. can also be used in microfabrication as sacrificial layer material. V. Seidemann et al. used sacrificial sputtered thin Cu films (~200 nm) to fabricate small movable parts; electroplated thick Cu layer (up to a few microns) for larger parts fabrication [11]. Likewise, H.C. Chiamori et al. [98] sputtered a 500 nm thick Aluminum sacrificial layer on Silicon wafer to fabricate microfeatures with SU-8 and diamondoid/single-wall carbon nanotubes (SWNT) nanocomposite. A 33 µm long, 2 µm wide, and 60 or 50 nm high sputtered Cr sacrificial

layer was patterned using electron-beam evaporation in the work of Marcel A. G. Zevenbergen, et al. [99]. Nevertheless, these sacrificial methods are time consuming, and the prolonged exposure to the etchant damages devices.

Photoresists are normally used as structural material in microfabrication; but it is also reported that photoresists can also be used as sacrificial layer material [100, 101], especially in IC microfabrication due to its convenience to be dissolved easily in benign solvent solution and not hurt the fabricated circuitry [101]. Xudi Wang, et al. [100] also used positive photoresist Polymethyl methacrylate (PMMA) as sacrificial layer to facilitate the separation from SU-8 microstructure. In-hyouk Song and Pratul K Ajmera [101]took two different photoresists, Shipley S1813 and Hoechst AZ P4620, as sacrificial layer materials in conjunction of SU-8 photoresist top layer as electroplating mold in IC microfabrication. Polydimethylglutarimide (PMGI) is spinable at a wide variety of thicknesses; and it is photopatternable and has a glass transition temperature greater than the processing temperatures required for SU-8. P I G Foulds, et al. [102] used PMGI and Shipley S1813 as sacrificial materials for SU-8 surface-micromachining PMGI was used to release and achieve the freestanding microstructure and Shipley S1813 was used to release the unwanted Cr/Au deposition to attain the desired microstructures. Photoresists as sacrificial layer materials, compared to metallic sacrificial layer, can avoid evaporation leaking exposure damaging microstructures, and reduce processing steps and hence fabrication cost.

Some sacrificial layer was created for specific special purpose on releasing. Like in Saad A. Hasan et al. research [103], a copolymer -- poly lactic-co-glycolic acid (PLGA) was selected as sacrificial layer for its favorable solvent chemistry to release freestanding colloidal nanoparticles (NPs) assemblies. Because PLGA experiences minimal swelling and degradation in hexane, the NP suspension liquid and tolerance to hexane, PLGA was used as sacrificial layer and provides a stable surface for NP assembly.

Sacrificial etching has been developed in the field of microelectromechanical systems for various applications, including mechanical micromotors [104], acceleration sensors [105], switches [106] and micromirrors for optical projection [107].

Numerous materials can be used as sacrificial layer materials; here just a few of them are named. Different sacrificial materials are used in different environments to meet the need to release different fabrication materials. Similarly, diverse releasing techniques are needed and developed to remove sacrificial layers and liberate freestanding microstructures. Releasing techniques are developed corresponding to sacrificial material and fabrication material, which must have the ability to remove sacrificial layer and not damage microstructures. Usually, releasing techniques can be categorized into dry etching release and wet etching release.

Dry etching is generally an anisotropic material removal process where plasmas or etchant gases were used to remove the sacrificial material by applying high kinetic energy of particle beams, chemical reaction or a combination of both, which is also called reactive ion etching (RIE) [108]. Dry etching was first developed by S. M. Irving in 1968 [109, 110]. The capability of plasma processes was demonstrated by oxygen plasma ashing of a polymer-based photoresist film. Following in 1971, he disclosed experimental data pertaining to the plasma etching of silicon using CF_4 plasma [111].

O_2 plasma removal is a method to develop Omnicoat. Luciana Wasnievski da Silva, et al. [93], developed Omnicoat sacrificial layer in an O_2 plasma environment. In-hyouk Song and Pratul K Ajmera [101] demonstrated O_2 plasma removed S1813 positive photoresist sacrificial layer. The sacrificial layer was completely removed in a barrel asher with oxygen gas which laterally dissolved the sacrificial layer underneath the structure and free the microstructures. The dry etch used here is preferred because it does not suffer from stiction-related problems inherent in a wet etching process.

O_2 plasma can also be used to etch polyimide sacrificial layer. A Bagolini, et al. [95] conducted sacrificial etching of the polyimide using an isotropic dry etch process in high-

density, low pressure oxygen plasma at an under etch rate of 4 μm/min. To increase the O_2 plasma dry etching rate, solutions were found by research groups. Benjamin Mimoun et al. [97] used pure oxygen plasma for etching polyimide 115a (Fujifilm) with 1000W for 1h and 1.5h, still resulted in a thin silicon-rich residue layer. They developed adding small amounts of fluorine-containing gas carbon tetrafluoride (CF_4) to the pure oxygen. The mixed etching gas was then capable of achieving residue-free polyimide plasma etching. And this dry etching can realize residue-free plasma etching of polyimide coatings with both isotropic and anisotropic profiles, with 95% O_2 and 5% CF_4, at 1000W.

Reactive-ion etching (RIE) is the combination of physical etching and chemical etching. RIE processes are usually faster than physical or chemical etching since it combines both physical and chemical interactions. Javaneh Boroumand Azad [96] used dry RIE to remove hard-baked ProLift sacrificial layer; but it was so slow and the desired microstructures were damaged from unexpected-prolonged physical bombardment by plasma ions. They had the etching done under ultraviolet light using Trion RIE with 100 W power, 900 mTorr pressure, 98 sccm O_2, and 2 sccm CF_4 flow rate. It was found that blanket exposure to ultraviolet light allows rapid dry etch O_2 plasma of the ProLift surrounding the desired microstructures without damaging them.

Dry etching can avoid handling of dangerous acid and solvents, enables better process control and less undercutting. But it still has quite disadvantages. Equipments for dry etching are specialized and expensive. Some etchant gases used for dry etching are highly toxic and corrosive. Last but not least, dry etching is usually time-consuming, which can be up to tens of hours.

Wet etching can overcome dry etching's disadvantages. Wet etching is a material removal process that uses liquid chemicals or etchants to remove materials from substrate [31]. Wet etching process has three basic steps and always involves multiple chemical reactions that consume the original material. First, liquid etchant is applied onto the material which is to be removed; then the reaction between the liquid etchant and the material occurs and the material is dissolved; and the byproducts from the reaction

diffuses and needs to be cleaned away. Typically, wet etching is isotropic; but in some specific cases, it can be anisotropic [112, 113]. Here, wet etching release technique is using wet etching to remove the sacrificial layer between substrate and fabricated microfeatures to liberate them.

The most advantage of wet etching, compared to dry etching, is significantly process time reduced. The etching process can be reduced from tens of hours by dry etching to couples of minutes. D.E. Pesante, et al. [85] completely released multipolyeric microchips after 1 minute development of Omnicoat sacrificial layer in AZ 300 MIF positive photoresist developer. Compared with O_2 plasma removal of Omnicoat layer [93], the wet etching saved more than 90% process time.

Besides fast processing, wet etching also can release high-quality microfeatures. Marcel A. G. Zevenbergen, et al. [99] removed the Cr layer by immersing the device in chromium etchant (Merck, 111547.2500). I G Foulds, et al. [102] developed three methods to remove the PMGI layer without damage to SU8 layer. First, the sacrificial layer was immersed in 25% Tetramethylammonium hydroxide (TMAH) for 30 minutes at room temperature; and then in fresh 25% TMAH for 2 minutes; followed by bathing in DI water for 2 minutes and in isopropyl alcohol (IPA) for 2 minutes. Second, the sacrificial layer was developed in EBR PG (MicroChem®) at 60 ◦C; and then in fresh EBR PG for 2 minutes at room temperature; followed by bathing in IPA for 2 minutes. Third, sacrificial layer was placed in glacial acetic acid for 30 minutes at 60 ◦C; and then in fresh glacial acetic acid for 2 minutes at room temperature; followed by 2 minutes in DI water and 2 minutes in IPA. It is obvious that these wet etching uses much less processing time than dry etching. But these wet etching processes introduced highly toxic and corrosive chemicals, which can be dangerous.

To avoid using those harsh chemicals, nontoxic chemicals were selected preferentially. H.C. Chiamori et al. [98] chose water and salt crystals as etchant. After the nanocomposite was spun and developed. The wafer was bathed in water and salt crystals with applying 0.5 V through attached cathode for 16 hours; and the galvanic reaction

removed the Al layer and the samples were release. Saad A. Hasan et al. [103]immersed PLGA in water, where PLGA is not initially solvated, but instead is cleaved by hydrolysis of its ester linkages, reducing the PLGA to its water-soluble monomers. And the structural material colloidal nanoparticles (NP) is unperturbed since the hydrophobic end of oleic acid faces outward from the NPs. Submerging the substrate-bound NP film in water triggers breakdown of the PLGA, and within minutes yields freely floating macroscopic NP film.

Dry etching releasing and wet etching releasing have their own advantages and disadvantages as shown in all these researches summarized above. The proper releasing method should be chose incorporated with specific sacrificial layer material and structural material. The best releasing method can remove sacrificial layer fast without using harsh chemical, and not damage the desired features.

2.2 Contact-free Control in MEMS

For example, electrostatic force can be a dominant driving force for mechanical components against inertia in micro scale, as opposed to in macro scale where it is often negligible compared to gravity [114]. Magnetic forces can also offer an attractive option for actuation in MEMS because they scale favorably at micro- and nano-scale lengths [115, 116]. Unlike electrostatic force actuation, magnetic actuation is contact-free, making it ideal for applications where contamination must be avoided—such as interactions with cells or other biological samples [117, 118] —or where connecting the power source to the actuator would be cumbersome—such as freestanding microrobots [82, 119, 120]. And unlike systems based on electrostatic or dielectric forces, magnetic actuators can operate in liquid or gas and are unaffected by the ionic concentration of the surrounding medium. However, magnetically responsive materials are often difficult or expensive to integrate into microfabrication schemes with high patterning resolution. So new microfabrication are in demand to overcome these defects; and fabricate MEMS microstructures micromanipulated by contact-free magnetic field.

In various MEMS applications, ranging from microaccelerator, mirogyroscope, to micro-drug-delivery system, the complexity of microsystems is increasing and requires a lot of different materials, diverse microfabrication processes, and actuation methods to realize. Among those, some applications require contact-free wireless actuation, where contamination must be avoided – such as interactions with cells or other biological samples [117, 118]; or connecting the power source to the actuator would be cumbersome – such as freestanding microrobots [82, 119, 120], especially in liquid or gas environment [80, 84, 121] – such as biomedical applications in diagnosis and targeted drug delivery.

In order to achieve wireless actuation of untethered microrobots, fabrication material and method are investigated and developed. To date, primary strategies are reported for actuating untethered microrobots are electrostatic forces[122, 123], thermal forces [124], and magnetic forces and torques [82, 117, 120, 125-128]. Corresponding to the control strategies, the microrobots geometries and fabrication materials are variously designed and chosen.

Donald, Bruce R., et al [122, 129] fabricated the untethered microrobot with polysilicon by dimple etch and via etch and evaporation coated with chromium. The microrobot consists of an untethered scratch drive actuator (A) and a cantilevered steering arm (B) exerting from one corner as shown in Figure 2.15. The untethered scratch drive is used for propulsion; and the steering arm can be raised or lowered for turning. The “wavy” background of the image is arrays of insulated interdigitated electrodes, which can provide power source to generate electrostatic field and send control signal to the microrobots.

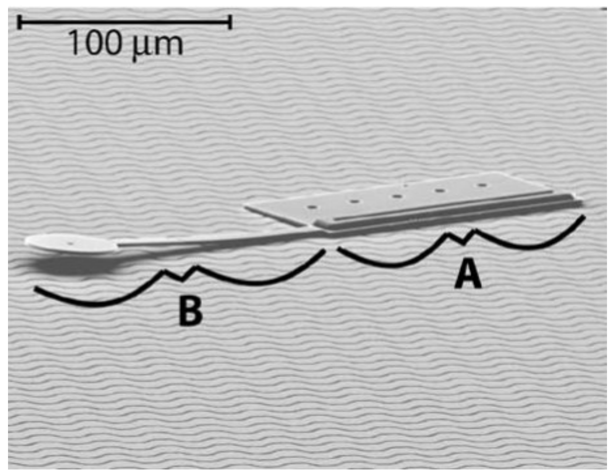

Figure 2.17 SEM image of an untethered electrostatic microrobot [122].

Based on the states of the untethered electrostatic microrobot parts, the movements of the microrobot can be categorized into four states – S_0: relaxed scratch and raised arm; S_1: flexed scratch and raised steering arm; S_2: relaxed scratch and lowered arm: S_3: flexed scratch and lowered arm. These states of actuation movements are as shown in Figure 2.16.

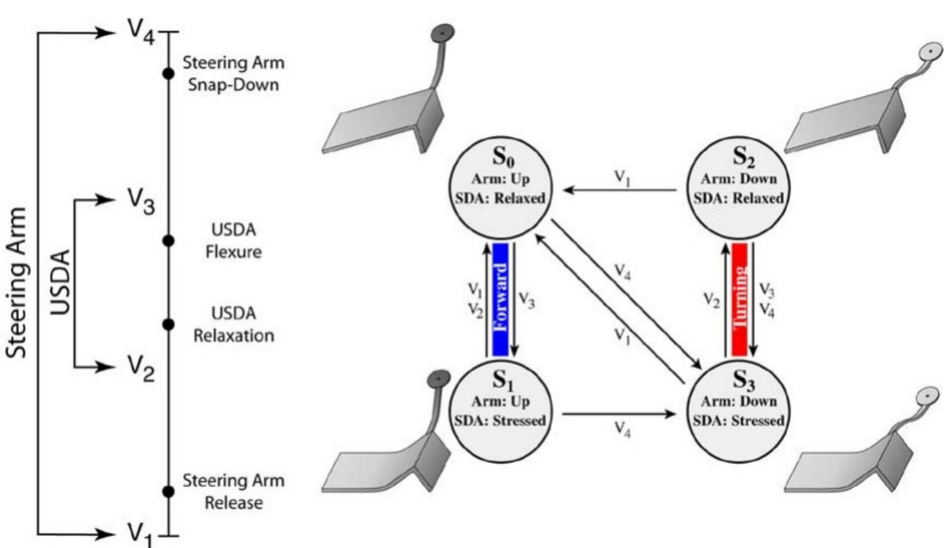

Figure 2.18 The state transition diagram of the microrobot [122].

To actuate microrobot in a desired movement, moving forward or turning, a control command is specified by an electrical pulse, and is stored in the elastic flexure of the microrobot components. Then continuous motion can be driven by applying AC waveform. Four voltages, $V_1 = 0$ V $< V_2 = 39$ V $< V_3 = 112$ V $< V_4 = 140$ V, are used in constructing the control waveforms. Any applied voltage below the relaxation voltage will cause the untethered scratch drive actuator (USDA) to relax; and any voltage above the flexure voltage will cause it to flex. Any applied voltage below the release voltage will raise the steering arm, and any voltage above the snap-down voltage will lower it. The microrobot would switch to another state when the voltage is changed. Therefore, the microrobot can move forward by repeatedly transitioning between states S_0 and S_1, and turn by transitioning between states S_2 and S_3.

The untethered microrobot speed and turning rate were tested by applying 4 kHz AC for scratch forward motion and 2, 4, 8, 16 kHz for arm steering motion. The experiments revealed that the higher the frequency applied, the faster the microrobots moved forward; but the turning wasn't affected by various frequencies. These untethered electrostatic microrobots realized turning error of less than 3.7 ^{o}/ mm during forward motion, turn with radius as small as 176 μm; and achieved speeds of over 200 μm/sec with an average step size as small as 12 nm. They have been shown to operate open-loop for distances exceeding 35 cm without failure.

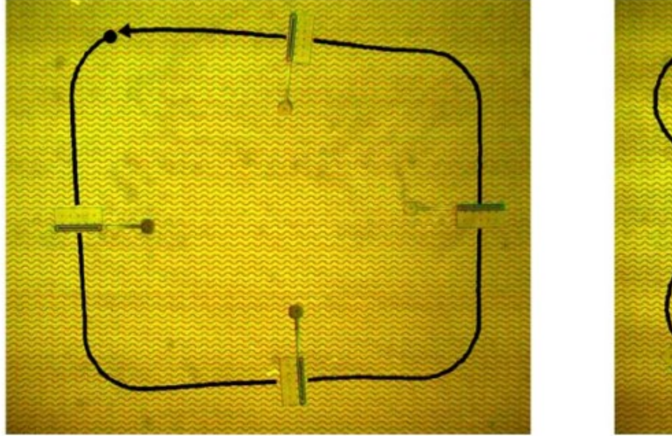

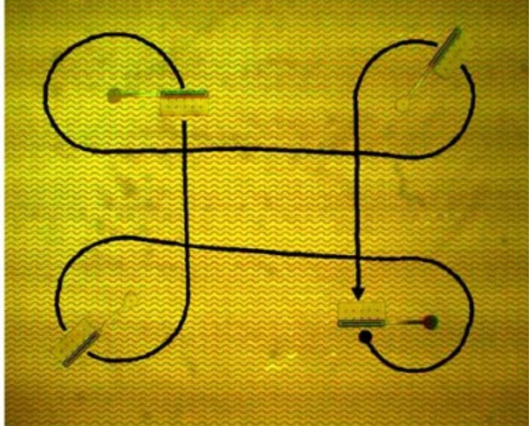

Figure 2.19 Sample paths traversed by one of the micro-robots under teleoperated control [122].

Chytra Pawashe et al [123] proposed an improved electrostatic control system for microrobots, which enables the control of multiple microrobots simultaneously applying electrostatic forces to selectively anchor the microrobots onto the surface. Since this approach didn't require geometric differences like in Donald's [130] and Vollmers' [120], the microrobots were fabricated by laser micromachined (Quicklaze, New Wave) out of a hard magnetic material – neodymium-iron-boron with dimension 250 x 130 x 100 μm.

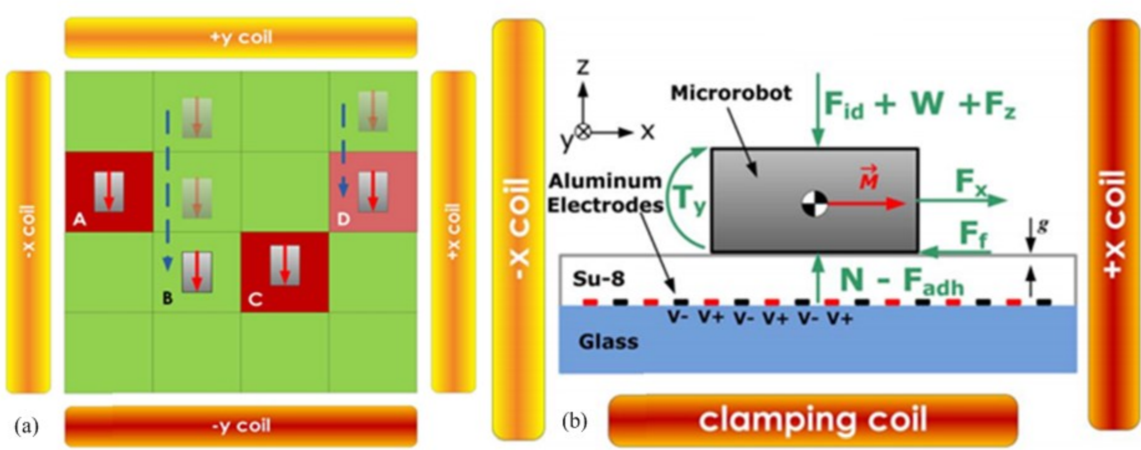

Figure 2.20 (a) Top-down schematic of four microrobots, A, B, C, and D, demonstrating coupled and decoupled motion. (b) A free body diagram of an anchored magnetic microrobot experiencing an electrostatic anchoring force [123].

This electrostatic control scheme allowed for the uncoupled serial actuation of each microrobot, as well as parallel actuation of multiple robots as demonstrated in Figure 2.18 (a). Each of the 4 x 4 squares shown in the figure were independently electrostatic controlled anchor. The –y coil was held at a constant current to orient the microrobots towards the coil. Microrobots A and C were anchored to the surface and did not translate; while, B and D were moving towards the –y coil and D was anchored after passing one square. As shown in Figure 2.18 (b), a 3.5 μm thick SU8 layer was fabricated with an anchoring voltage of 260 V which resulted in approximately 23 μm force to anchor the microrobots; and a pulsing frequency of 20 Hz was used for microrobots translation. This electrostatic control method realized multiple microrobots uncoupled control.

Besides electrostatic energy driven microrobots, thermally actuated microrobots are also developed by researchers. Sul, O. J., et al [124] utilized material shape deformation by thermal effect to actuate microrobot as fast as 100 μm/s with as 30 nm step. The microrobot was fabricated with three radial spokes as “legs” on a polymethyl metharcrylate layer on SiO_2 and deposited with 5 nm Au, 400 nm Al, and 200 nm Cr.

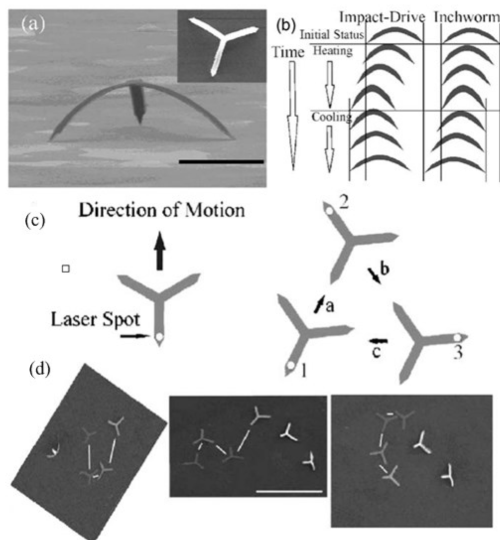

Figure 2.21 (a) Side view and top view SEM image of a standing microrobot. (b) Comparison of idealized impulse drive and inchworm walk. (c) and (d) Schematic and SEM images of forward motion and steering. Scale bar = 20 μm in (a) and 120 μm in (d) [124].

In microrobot forward actuation, based on the thermally power order, the motion driven can be classed into two categories, an inchworm drive and an impulse drive as shown in Figure 2.19 (b). Inchworm drive was resulted from cyclic deformation of successive legs; and impulse drive was continuously laser heating one leg but with pulse to let it cool and relax to original shape [131, 132]. In their research, the thermal energy was laser powered with 20 mW and 3 μm spot projected at the microrobot leg. With pulsed heating laser, the laser spotted leg deformed and relaxed, and the microrobot moved forward. Steering microrobot needed to thermally power the legs asymmetrically; otherwise, it would not move if powered spatially symmetric in a contraction phase.

Previous microrobots were remotely powered and controlled by electrostatics, laser-driven thermal impact, or magnetic fields. Electrostatic microrobots require a flat structure to harvest sufficient energy, limiting their movements to flat surfaces. Thermal-driven microrobots would generate heat, which prevents their use in microorganisms. In contrast, magnetic microrobots, which do not have structural or heat generation limitations, are able to exert large forces and carry other devices [133]. Unlike systems based on electrostatic or dielectric forces, magnetic actuators can operate in liquid or gas and are unaffected by the ionic concentration of the surrounding medium. Magnetic fields have emerged as the most favorable option, especially for biomedical applications, because they are capable of penetrating nonmetallic materials with little or no interaction and are nearly harmless to most living organisms [125].

K. B. Yeşin et al. [127] demonstrated a three-dimensional elliptical shape magnetic microrobot by microassembing nickel microcomponents using UV activated glue. The microrobot can be steering actuated in external magnetic field as shown in Figure 2.? (b) and (c). Through this steering actuation system using Maxwell and Helmholtz fields, the magnetic force and torque on the microrobot can be controlled independently; therefore, the microrobot actuation can be achieved in 2D surface.

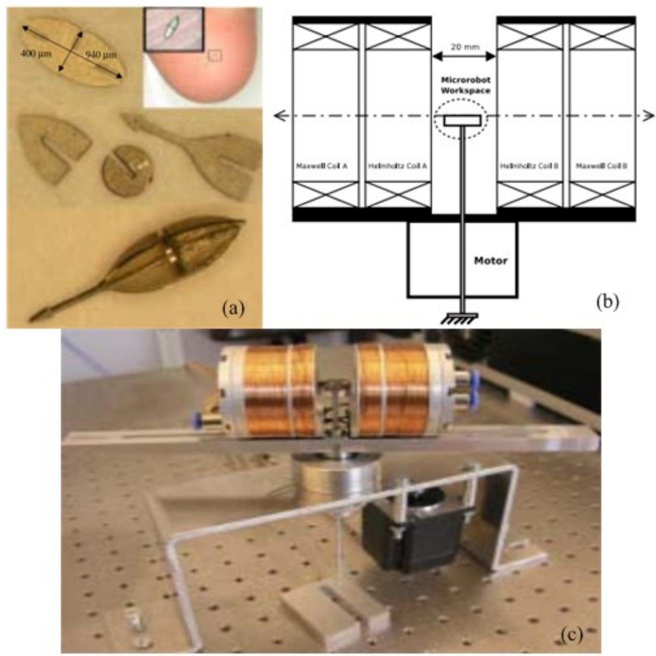

Figure 2.22 (a) Nickel microrobot components and an assembled microrobot. (b) Schematic of microrobot steering actuation system. (c) Image of magnetic steering system [127].

The microrobots reached saturation magnetization between 5- 8 x 10^5 A/m at approximately 0.2 T external field. And a minimum gradient of 0.7 T/m of magnetic field would be able to resist fluid drag force. These results indicated that the microrobots have potential for biomedical use; but the current clinical MRI machine provides tens of mT/m of gradients in any direction for imaging purposes [128] and such gradient could not provide high enough magnetic field gradients to actuate the microrobots [127]. To apply the microrobots application to biomedical field, especially MRI system for cardiovascular system, J.-B. Mathieu et al. [128] used ferromagnetic materials 1010/1020 carbon steel to attain the strongest magnetization with higher saturation value. Their experiments showed that 600 µm spherical ferromagnetic microrobots were actuated in relatively larger blood vessel with mm diameter with 18 mT/m field gradient. But in smaller vessels, microrobots needed as high as couples of T/m field gradient to be propelled, which current MRI system cannot meet this requirement. But lots of other biomedical applications of magnetic microrobots were reported for cellular level vivo medical task

[117, 134, 135], targeted drug delivery [84, 136], minimally invasive surgery [137-139] etc.

On the other hand, K. B. Yeşin group didn't provide any information about the microrobot movement, like speed, steering radius etc.; and their magnetic steering actuation system could not control multiple microrobots simultaneously and achieve precision control. Hsi-Wen Tung, et al. [125][designed a novel microrobot utilizing spring-mass oscillator system concept to solve those problems. This microrobot consists of two masses made with ferromagnetic material cobalt–nickel (CoNi) alloy and two springs and frames using SU-8 2025 a instead of gold spring used in other designs [120, 126]. Compare to expensive, complex, and laborious gold spring, the polymer based microrobots were easier, faster, and cheaper to fabricate. The microrobot was coated with Au for biocompatible use.

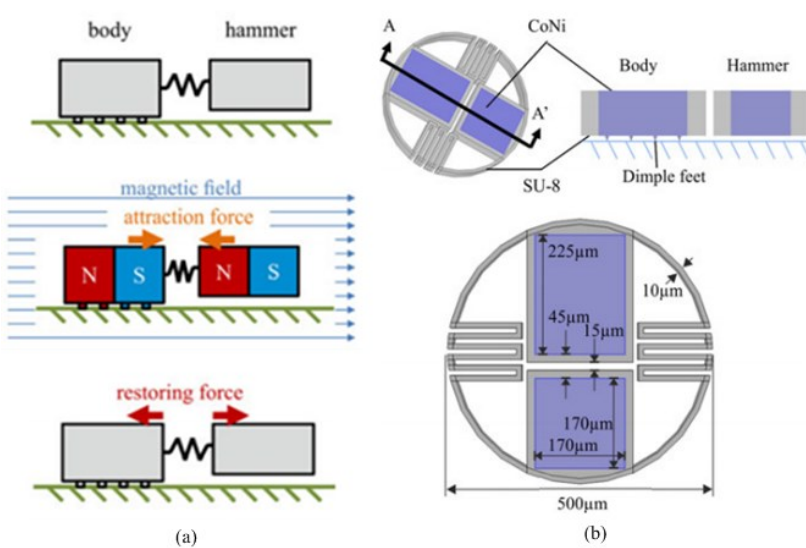

Figure 2.23 (a) Schematic of resonant magnetic microrobot actuation. (b) Microrobot design model and cross-section from A-A' shows the dimple feet [125].

The microrobots were actuated by external magnetic field. When the body mass and the hammer mass exposed to an external oscillating magnetic field, the two masses were magnetized in the direction of the long axis; the attractive force between the two masses pulled them together. And when the magnetic field is off, the two masses were pushed

away by the restored energy in the springs. Especially when the frequency of the magnetic field was close to the microrobot, the force can be magnified and the microrobot would be driven a net displacement. The microrobots was tested in an external magnetic field with 4 mT flux density and various frequencies, a speed of over 20 mm/s , compare to 12.5 mm/s in other researches [120, 126], was achieved at 7.3 kHz on a titanium-coated silicon wafer in air.

The control method proposed by Hsi-Wen Tung group could only actuate microrobots in two-dimensional surface. Recent research has developed microrobots and control approaches, which enable precision control of the microrobots in three-dimensional space [82, 140-142]. Khalil, Islam SM, et al [142] designed proposed a magnetic control system for precisely control of microrobots in three-dimensional space as shown in Figure 2.21 below.

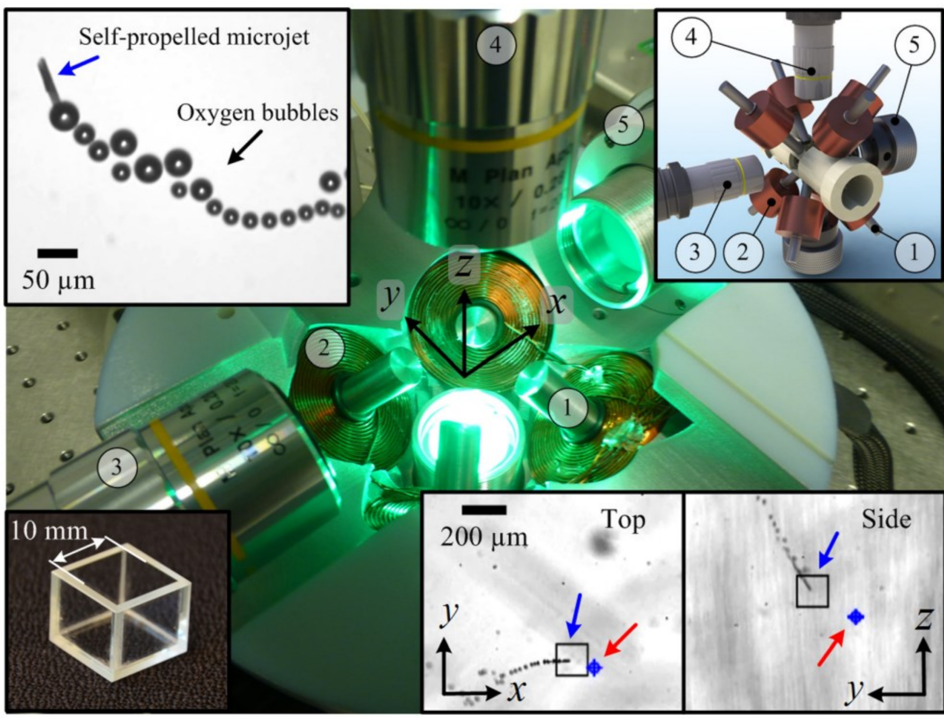

Figure 2.24 Electromagnetic system for the wireless control of microjets in three-dimensional space. Insets in the bottom right corner show a microjet moving towards a reference position (crosshair) under the influence of its propulsion force and the controlled magnetic fields. The upper left inset shows the propulsion mechanics of the microjet. The bottom left inset shows a reservoir for the hydrogen peroxide that contains microjets [142].

The magnetic system consisted of two sets of orthogonal arrays of iron-core, coils, and microscopies with auto-focusing and adjustable illumination. And a 10 x 10 x 10 mm^3 reservoir with hydrogen peroxide was used for microrobots actuation environment. 40 mT, 38 mT and 65 mT magnetic field were applied in x, y , and z directions. The microjets were controlled within a spherical region with diameter around 400 μm by the closed loop control strategy. These microjets could be propelled with an average speed of 222 μm/s in the horizontal plane; and could reach as fast as 272 μm/s when diving downward overcoming the buoyancy forces, interaction forces with bubbles, and vertical drag force; while they swam upward faster at around 316 μm/s. This electromagnetic actuation system realized real three-dimensional actuation of microrobots, which offered potential to be used in diverse applications that required precise positioning such as targeted drug delivery.

Chapter 3 Fabrication of Two-dimensional Polymer Micromagnets

3.1 Introduction

Magnetic forces offer an attractive option for actuation in MEMS and microscale systems because they scale favorably at micro- and nano-scale lengths [115, 116]. The magnetic actuation is contact-free, making it ideal for applications where contamination must be avoided, such as interactions with cells or other biological samples [117, 118], or applications where connecting the power source to the actuator would be cumbersome, such as freestanding microrobots [82, 119, 120]. And unlike systems based on electrostatic or dielectric forces, magnetic actuators can operate in liquid or gas and are unaffected by the ionic concentration of the surrounding medium.

The benefits of microscale magnetic actuation have led to its implementation in a variety of MEMS and microfluidics devices, performing tasks such as wireless on chip mixing [143] and pumping [144] of fluids; in microrobotics, the use of magnetic force to provide wireless control and power is particularly appealing as it does not require the robots to be operated on a specialized surface, and it can be used to perform complex three-dimensional motions [140]. Remotely-controlled microscale robots show potential in a variety of applications, including interaction with samples in lab-on-a-chip systems, microassembly of structures [145], in-vivo delivery of cancer therapies, and performance of retinal- and neuro-surgical procedures [146]. But for many of these applications, ferro- or paramagnetic components are challenging to integrate into existing microfabrication schemes.

Researchers have demonstrated a variety of methods for creating microscale magnetic components; most of which can be characterized as either additive, subtractive, or polymer mixing methods. Additive methods, such as deposition of paramagnetic materials via sputtering or evaporation [82, 120], show good results and high purity for

small volumes, but can be expensive and time consuming for larger features. Subtractive methods include etching or laser-cutting of a structure from a blank of the desired magnetic material [147]; these methods can achieve excellent material density and purity, but are difficult to adapt to small features or integrate with other components. Photopatternable polymer magnets have been demonstrated by mixing epoxy-based photoresist with Ni [148, 149] or Fe_xO_x nanoparticles [117, 150-152]; these materials exhibit excellent patternability, but the required nanoparticles are prohibitively expensive for many applications.

This chapter describes a facile method of creating inexpensive photopatternable polymer micromagnets and characterization of fabrication properties of this polymer-based magnetic material. The magnets are composed of Nd-Fe-B microparticles dispersed in an UV-curable polymer matrix; the resulting material is inexpensive, biocompatible [153], chemically resistant [44], and easy to integrate with lithography-based microfabrication processes. The Nd-Fe-B material used in this work has very high coercivity compared to nanoparticles used in [117, 148-152], which allows the material to maintain its excellent magnetic properties even when subjected to a very high applied magnetic field.

3.2 Materials and Fabrication Method

The polymer micromagnets were created using a magnetic composite composed of Nd-Fe-B microparticles with 2 μm average diameter (Magnequench®) and SU-8 10 negative photoresist (MicroChem®). The Nd-Fe-B microparticles are 25.8% Nd, 73.2% Fe, and 1.0% B by weight; and the kinetic viscosity of SU-8 10 is 1050 mm^2/s. The magnetic composites were prepared by mixing 10% (1.5%) concentrations of Nd-Fe-B microparticles by mass fraction (volume) with SU-8 10 in microcentrifuge tubes. To avoid settling of the magnetic particles and attain a uniform dispersion, samples were mixed by vortexing (Vortex Genie 2, Scientific Industries) at 3000 rpm for 30 minutes immediately prior to use. Unless otherwise stated, particle concentrations are given by fractional mass percentage in the thesis.

To create freestanding two-dimensional micromagnets, silicon wafers were coated with a sacrificial layer, Omnicoat (MicroChem®), which was applied by spin-coating at 500 rpm for 5 sec, followed by 3000 rpm for 30 sec, and baking at 200 ºC for 1 minute, in accordance with the manufacturer's instructions. After the wafer cooled to room temperature, the mixed magnetic composite material was applied to the surface by spin-coating at 500 rpm for 5 sec (ramp rate of 100 rpm/s) followed by 30 sec at 1000 (ramp rate of 300 rpm/s). This was followed by pre-exposure baking at 65 ºC for 2 minutes and 95 ºC for 5 minutes. Then the composite was patterned using ultraviolet (UV) radiation using a mask aligner (Karl Suss MJB3) for 35s (130 MJ/cm^2 exposure energy). Samples were post-exposure baked at 65 ºC for 2 minutes and 95 ºC for 2 minutes. This was followed by soaking the samples in SU-8 developer (MicroChem®) with gentle agitation for 5 minutes to sufficiently remove the uncrosslinked SU-8 based magnetic composite material. The fabrication process is shown in Figure 3.1.

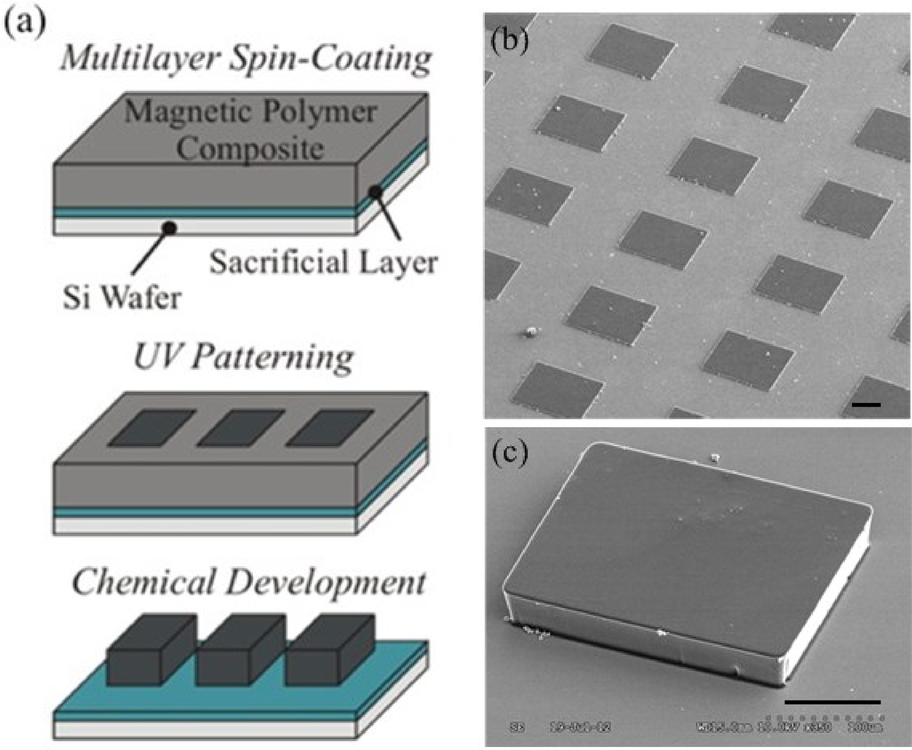

Figure 3.1 (a) Fabrication process of freestanding two-dimensional magnetic micromagnets. (b) Scanning electron microscopy (SEM) images of micromagnets arrays. (c) SEM image of single 40mm thick micromagnet. Scale bars = 100 μm [121].

In order to obtain freestanding micromagnets, the patterned magnets created using the method just described were released from the silicon surface by chemically dissolving the sacrificial Omnicoat layer. The Omnicoat was removed by soaking the wafer in PG Remover (MicroChem) for up to 30 minutes under gentle agitation. Individual micromagnets were then carefully separated out using a micromanipulator. Alternatively, the PG Remover solution containing the released micromagnets was pipetted into a microcentrifuge tube where a permanent magnet was used to collect the robots to the side of the vial; several wash steps were performed to remove the PG Remover and replace it with isopropyl alcohol for long-term storage. Optical images of micromagnets before and after dissolving the Omnicoat layer are shown in Figure 3.2.

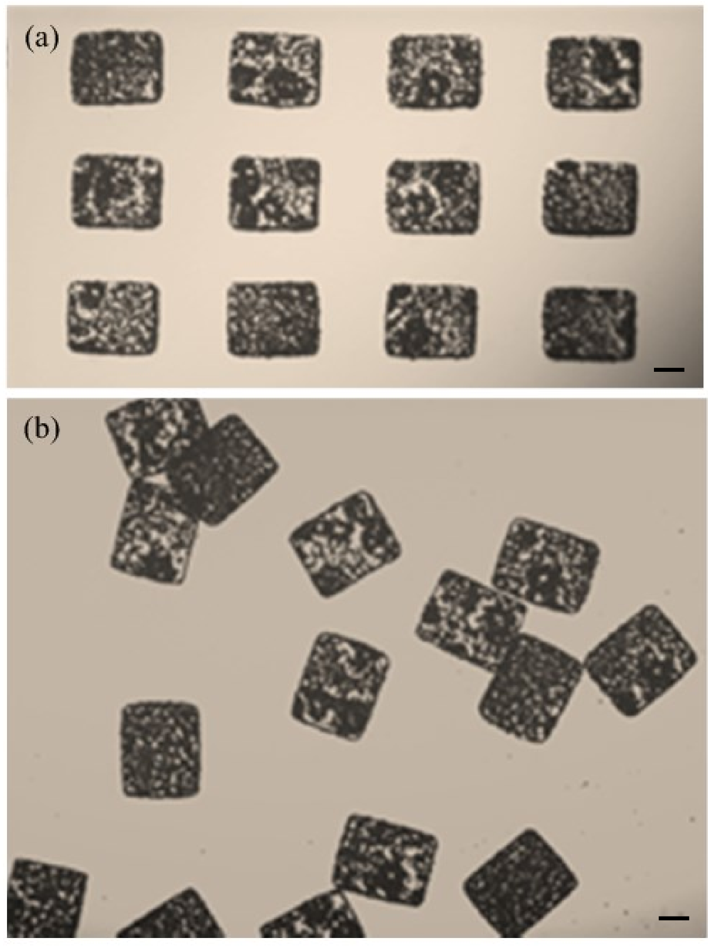

Figure 3.2 (a) Optical microscopy image of patterned micromagnets. (b) Optical microscopy image of freestanding micromagnets released from substrate by dissolving sacrificial layer. All scale bars = 100 μm [121].

3.3 Composite Material Characterization

In order to characterize the effect on material viscosity caused by adding magnetic microspheres to SU-8, polymer magnet samples were fabricated at various spin-speeds, particle concentrations, and exposure energy. The sample micromagnets were prepared by mixing 10%, 20%, 30% and 40% (by mass ratio) magnetic microparticles, and spun at 1000 rpm, 2000 rpm, 3000 rpm, and 4000 rpm; and then exposed to UV radiation at various energy values (35 - 375 mJ, depending on thickness). The height of each sample was measured using scanning white-light interferometry (Zygo Newview 5000).

The results of micromagnet thickness as a result of particle concentration and spin speed are shown in Figure 3.3, with the overall results summarized in Figure 3.4. While the addition of Nd-Fe-B microparticles does cause a small increase in material thickness, particularly at low spin speeds, the overall impact is minor.

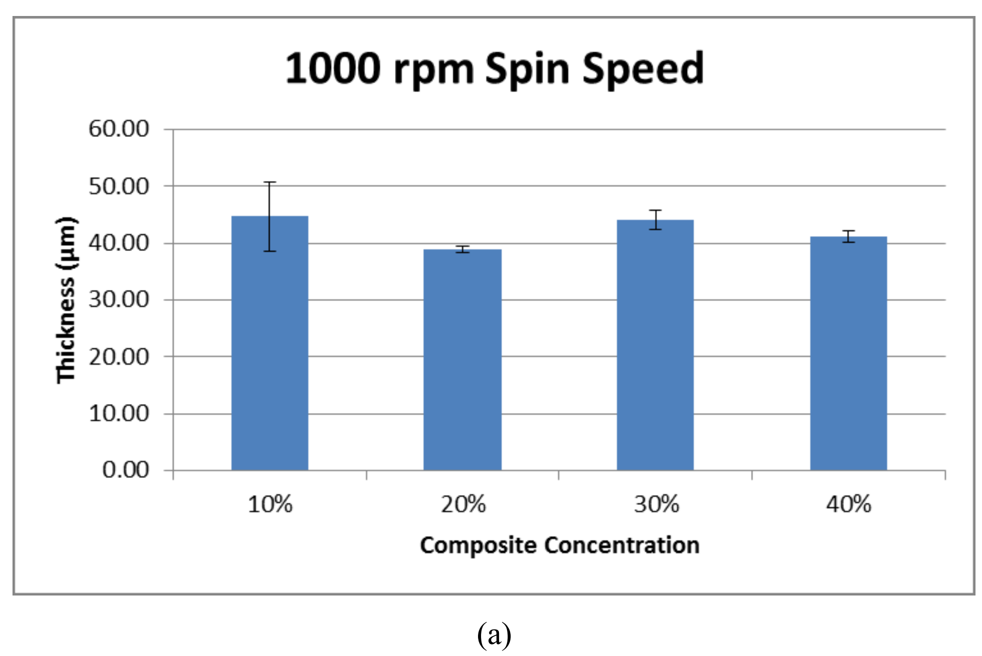

(a)

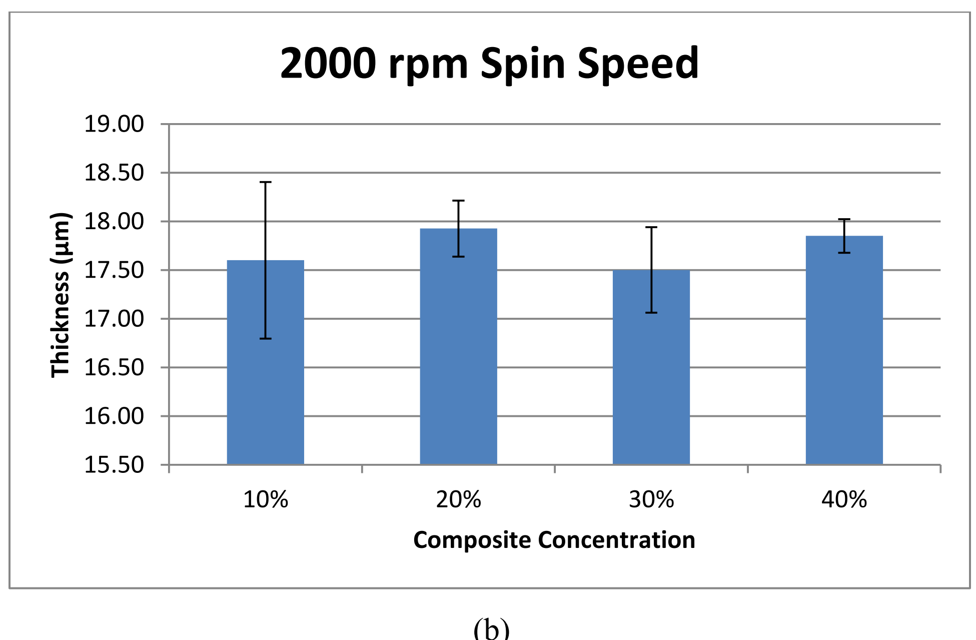

(b)

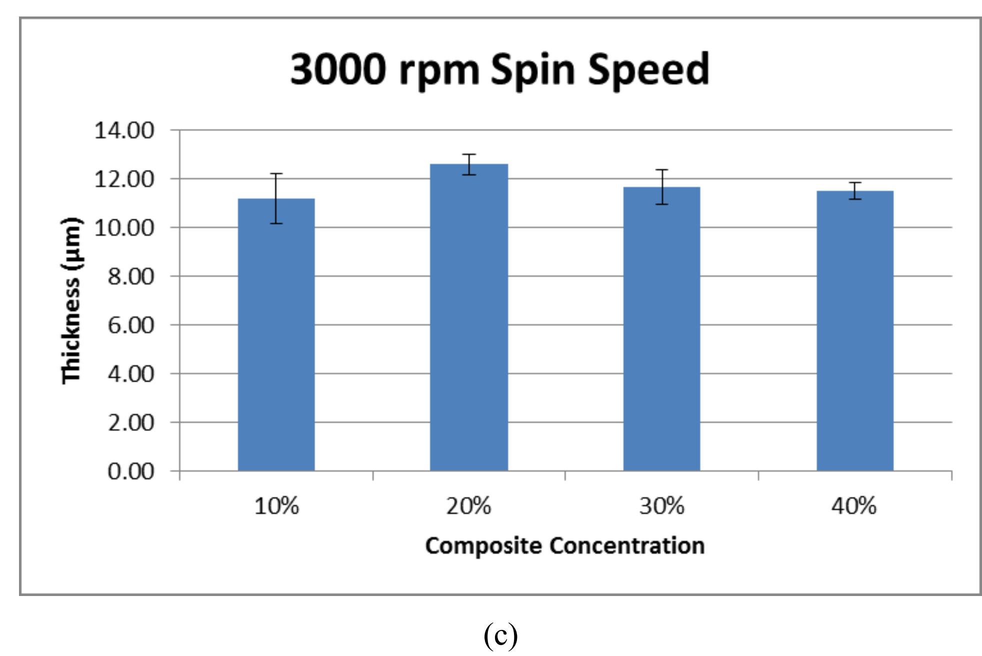

(c)

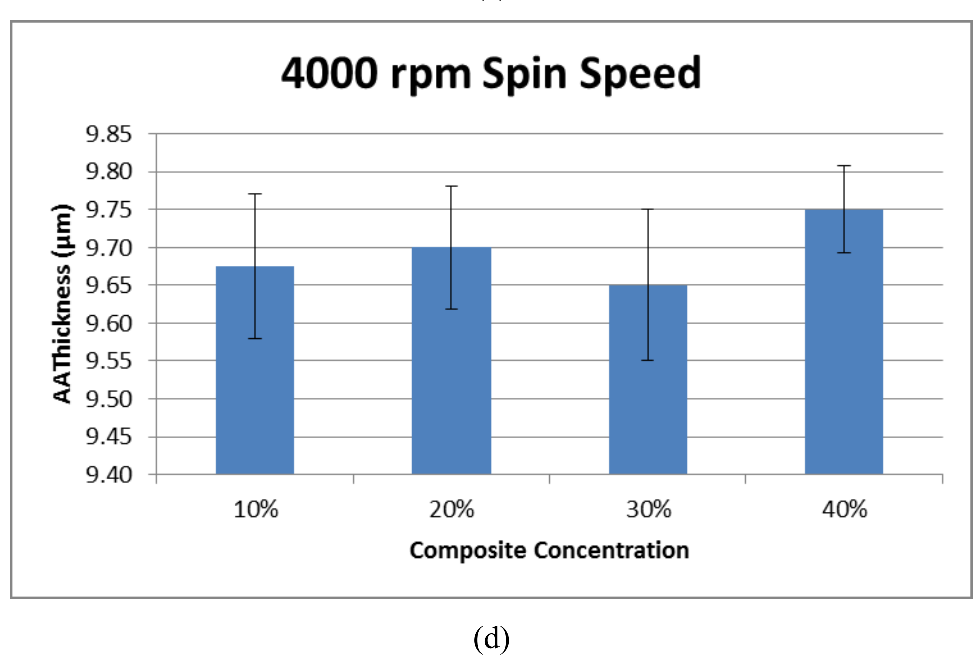

(d)

Figure 3.3 Material thickness as a function of spin-coating speed for different mass ratios of magnetic microparticles. (a) 1000 rpm spin-coating speed. (b) 2000 rpm spin-coating speed. (c) 3000 rpm spin-coating speed. (d) 4000 rpm spin-coating speed.

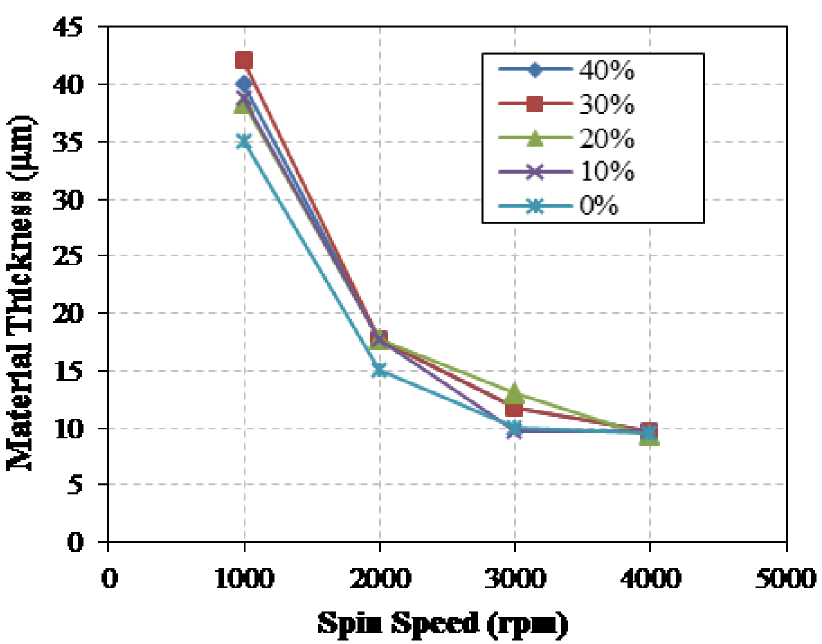

Figure 3.4 Spin speed versus composite thickness for magnetic polymer composite using manufacturer's recommended exposure energy for corresponding thickness micromagnets [121].

A small change in the mass fraction of solvent in a polymer (x_s) can have a large impact on dynamic viscosity (η) of the material, as described by the following relation: $\eta \sim (1 - x_s)^4$ [154]. Using known relations between material thickness during spin-coating (h) viscosity and spin speed (ω): $h \sim \sqrt{\eta/\omega}$, it is possible to derive a relation between mass fraction of solvent, spin-speed and material thickness:

$$h \sim (1 - x_s)^2 \omega^{-1/2} \qquad 3.1$$

In the current work, an SU-8 formulation with a high viscosity and low initial mass fraction of solvent was chosen because it can be used to produce a large range of material thicknesses (10-40 µm). Because of the small initial amount of solvent in the polymer, the addition of magnetic particles does not result in an appreciable change in the volume fraction of solvent, which is consistent with the small change in spin thickness seen in Figure 3.4. A much larger change would be expected when using a polymer formulation with higher initial mass fraction of solvent.

Optimized exposure energy for the magnetic composite was found by observing the geometry of polymer micromagnets produced using different UV exposure times, particle concentration, and spin-speed combinations. The samples and experiments were prepared the same methods as the previous experiment for characterization of the effect on material viscosity. All geometric measurements were made using SEM and scanning white-light interferometry for each experimental group.

Underexposed samples were found to have poor adhesion to the fabrication surface and would often detach during the development step in fabrication. Overexposed samples displayed enlarged geometry with excessively rounded corners; optimized samples showed minimal feature blurring while maintaining good adhesion. The optimized exposure time/intensity for material at different thicknesses/concentrations is shown in Figure 3.5 and the results are fairly uniform; addition of microparticles at the concentrations listed here has minimal impact on the energy necessary to pattern the SU-8 material. A similar effect was reported with the addition of Ni nanoparticles to SU-8, and is considered to be a result of the scattering effect of the particles [148].

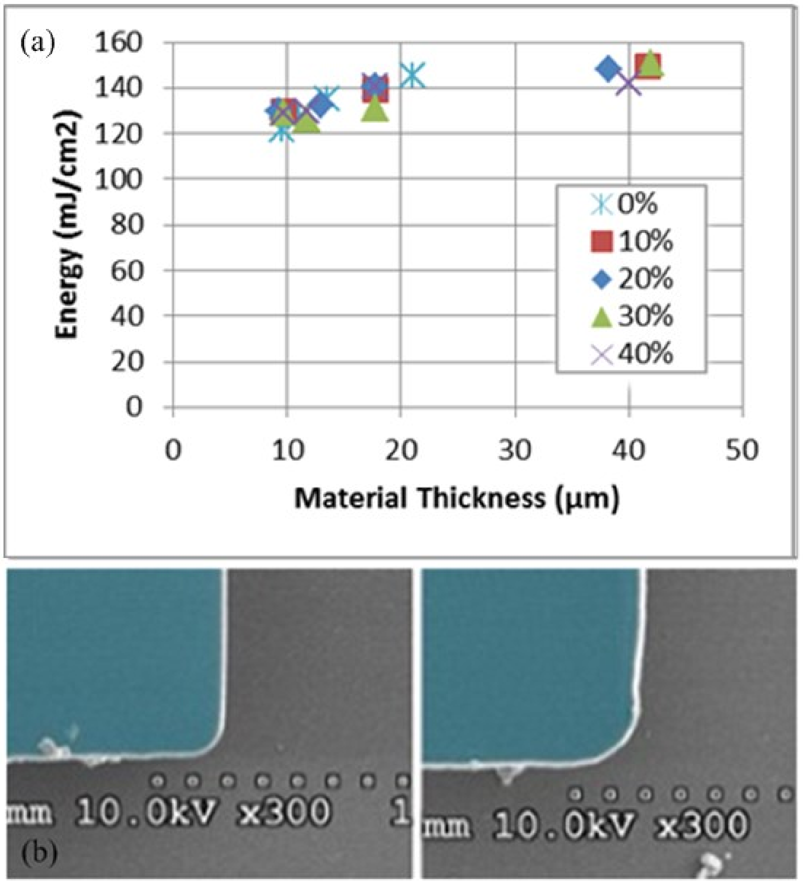

Figure 3.5 (a) Optimized UV exposure energy necessary for material crosslinking. (b) SEM images display rounding of corners inherent in material processing (left) and excessive rounding of corners and deterioration of edges due to UV overexposure (right) [121].

Uniform distribution of magnetic particles in the composite material is important for obtaining homogeneous magnetic properties. This parameter was characterized by analyzing the optical uniformity of high-magnification optical microscopy images of polymer micromagnets produced at several particle concentrations and spin speeds. Images were digitally processed using ImageJ software to dice each 300 μm x 240 μm micromagnet area into 20 μm x 20 μm subsets and then calculate the percentage of each subset occupied by magnetic particles (C). The average (μ_C) and standard deviation (σ_C) of this value was calculated for set of processing parameters. As particle concentration increases, $\mu_C \rightarrow 100\%$ and as material uniformity increases, $\sigma_C \rightarrow 0\%$. The statistical

parameters, histograms of C values for each sample, and representative optical microscopy images are shown in Figure 3.6.

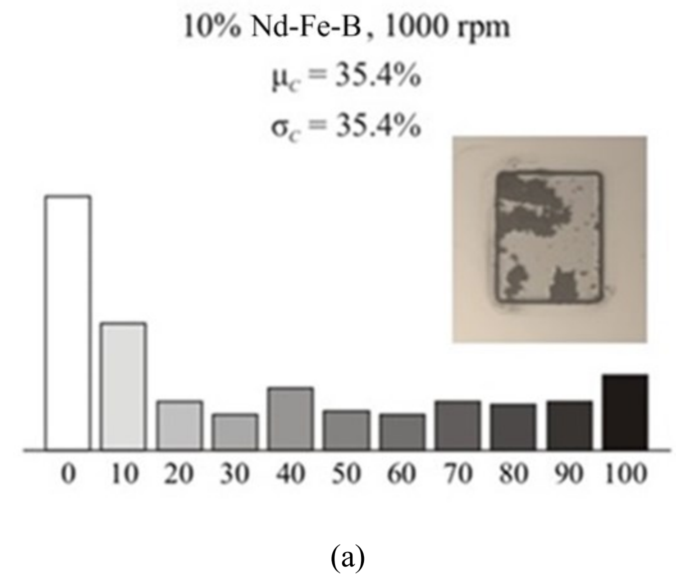

(a)

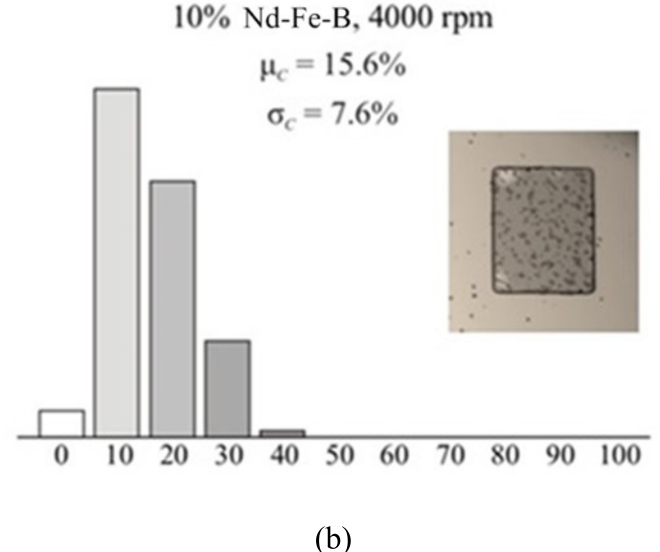

(b)

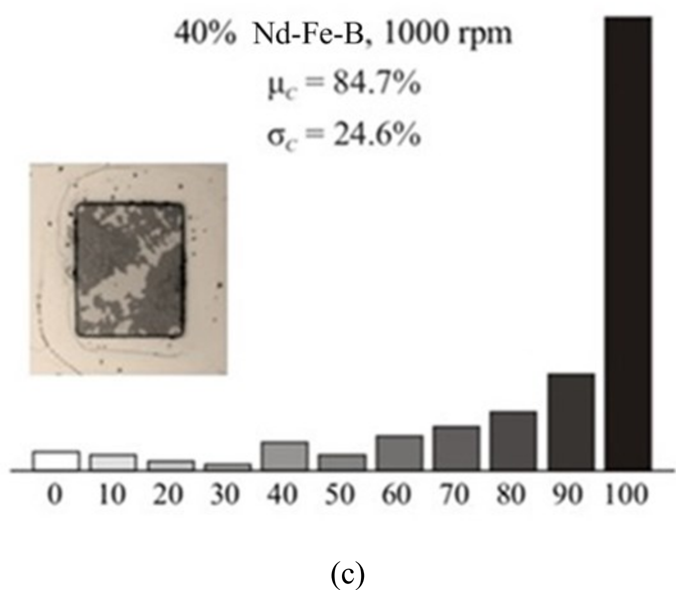

(c)

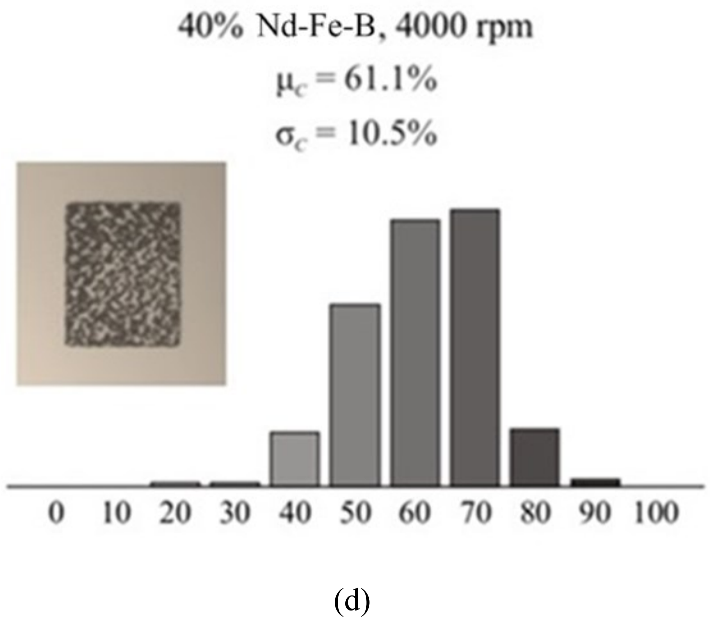

(d)

Figure 3.6 Magnetic composite uniformity for different particle concentration and fabrication spin speeds. Histograms represent C values for samples at given processing parameters [121].

At lower spin speeds, magnetic microparticles in the polymer composite material clustered together to form large aggregates, but at higher fabrication speed the particles became more uniformly dispersed. Micromagnets fabricated at 1000 rpm had a splotchy,

nonuniform appearance and high σ_C values, regardless of particle concentration. As processing spin speeds increased, the particle distribution became substantially more uniform; at 4000 rpm, σ_C values were considerably lower than the 1000 rpm values and the average particle aggregate size also decreased. This shear-mixing effect was observed at all concentrations and enables the creation of well-mixed magnetic composites by controlling fabrication speed instead of requiring chemical surface modification of the magnetic particles [147] or additional chemical solvents [145].

Increased spin speed causes more uniform distribution of the magnetic particles, but also decreases the material thickness; for a given surface area, magnets created at a higher spin speed will have smaller total volume and fewer included magnetic particles. As a result, the thicker, low-speed samples analyzed in Figure 3.6 have higher mean C values than comparable high-speed samples. To create polymer micromagnets with good particle distribution and high particle count, multiple layers of 40% Nd-Fe-B composite can be deposited sequentially on a silicon wafer and patterned with a single UV exposure step. The resulting magnets have roughly the same height and particle content as magnets fabricated at 1000 rpm, but with substantially improved material uniformity.

Patterning resolution of the magnetic composite was characterized by patterning the magnetic polymer composite material in a series of test patterns. Polymers with high (40%) and low (10%) magnetic particle concentrations were compared to pure SU-8 with regards to the minimum line width, minimum radius on a 90° corner and maximum aspect ratio that each mixture could reliably produce. The results of these tests are summarized in Table 3.1. These values show a noticeable decrease in patterning resolution caused by the addition of magnetic particles to SU-8. These particles produce a light scattering effect within the polymer during UV patterning, resulting in rounded corners and less defined geometry. Despite this effect, it was possible to produce high magnetic density structures with uniform particle distribution and better than 5 μm patterning fidelity.

Table 3.1 Fabrication properties and patterning resolution limits of magnetic polymer composite [121]

Particle concentration (% by mass)	Spin speed (rpm)	Thickness (µm)	Minimum line width (µm)	Corner radius (µm)	Maximum aspect ratio
0%	1000	35.0	2.2	2.7	16:1
0%	4000	9.5	1.8	1.4	5:1
10%	1000	38.7	3.3	4.84	11:1
10%	4000	9.7	3.1	3.54	3:1
40%	1000	40.0	5.4	5.35	7:1
40%	4000	9.7	4.6	4.3	2:1

3.4 Summary

This chapter introduced a large-scale facile microfabrication method for freestanding 2D polymer micromagnets that can be utilized in MEMS, microfluidics, microrobotics applications. These micromagnets can be patterned using standard lithography, are inexpensive to manufacture, and require limited equipment to produce. The method was capable of fabricating polymer micromagnets with 3 µm feature resolution and greater than 10: 1 aspect ratio. The liquid SU-8/Nd-Fe-B composite material was characterized and it was found that magnetic particles within the polymer matrix were possible to be dispersed uniformly by modulating spin speed during fabrication without requiring chemical modification of either of the two composite components.

Chapter 4 Fabrication and Contact-free Actuation of Encapsulated Micromagnets for Microrobotics Applications

4.1 Introduction

Over the course of the last 40-50 years, new microfabrication and microactuation methods have enabled the development of MEMS for a wide variety of applications. The emergence of micro-scaled robots is gaining a wide impact on industry and even daily life. Microrobots have been proposed for potential applications as broad as industrial inspection [155], micro-cargo transportation [117, 125], drug delivery [7], and minimally invasive surgery [137, 138].

Among the potential MEMS and microrobotics applications, many require contact-free wireless actuation. This is especially true when contamination must be avoided, such as interactions with cells or other biological samples [117, 118], or applications where connecting the power source to the actuator would be cumbersome, such as freestanding microrobots [82, 119, 120]. There are even many potential applications for biologically-based microrobots, such as biomedical applications in diagnosis and targeted drug delivery.

Current strategies for wireless actuation of untethered microrobots include electrostatic forces [122, 123], thermal forces [124], and magnetic forces and torques [82, 117, 120, 125-128]. Electrostatic actuation of microrobots requires a specially-designed surface to generate motion, meaning that microrobots based on this mechanism would be limited to movements on flat surfaces. Thermally-driven microrobots require heat generation to move, which limits their use in biological settings. In contrast, magnetic microrobots do not have structural or heat generation limitations; in addition, they are able to exert large forces and even carry other devices [133].

Magnetic forces offer an attractive option for actuation in MEMS and micro-scale systems because they scale favorably at micro- and nano-scale lengths [115, 116, 156]. Magnetic fields allow for actuation from a relatively long distance and, thus, a large working range [157]. And magnetic fields have been utilized for a long time with interactions inside the human body, which makes it acceptable for medical applications [158]. Finally, unlike systems based on electrostatic or dielectric forces, magnetic microrobots do not require batteries or electrical wires; they can be operated in liquid or gas and are unaffected by the ionic concentration of the surrounding medium.

Researchers have used a variety of microfabrication methods for creating magnetic microrobots. Most of which can be characterized as direct microfabrication methods, which means the microrobots were fabricated directly with the magnetic material, such as deposition of paramagnetic materials via sputtering or evaporation [82, 120], show good results and high purity for small volumes, but can be expensive and time consuming for larger features; etching or laser-cutting of a structure from a blank of the desired magnetic material [147]; these methods can achieve excellent material density and purity, but are difficult to adapt to small features or integrate with other components. And all these methods cannot guarantee the microrobots are biocompatible or chemical resist since the magnetic material are exposed outside to the actuation environment.

In this work, we proposed a novel fabrication method of creating inexpensive microrobots encapsulated with magnetic core and their use in microrobotics application. The magnetic microrobots were made with three layers of photopatternable material. The outer two layers are SU-8 photoresist and the inner core is magnetic composite mixing Nd-Fe-B microparticles and SU-8 photoresist. This structure completed encapsulated magnetic particles inside SU-8 layers and enabled the magnetic robot biocompatible and chemical resistant; and these magnetic microrobots were actuated by an external magnetic field along desired path showing great potential for microfluidics applications.

4.2 Encapsulated Magnetic Microrobot Fabrication

The magnetic composite materials were prepared by mixing 60% (mass fraction) Nd-Fe-B microparticles with 2 µm average diameter and SU-8 10 negative photoresist in microcentrifuge tubes. To avoid settling of the magnetic particles and attain a uniform dispersion, samples were mixed by vortexing (Vortex Genie 2, Scientific Industries) at 3000 rpm for 30 minutes immediately prior to use.

In order to create structures that have the excellent patterning resolution of pure SU-8 but contain high magnetic particle density, a process for fabricating encapsulated microrobots was developed. These microrobots were created by sequentially depositing and patterning layers of pure SU-8 and SU-8/Nd-Fe-B composite, as shown in Figure 4.1. First, a base layer of pure SU-8 was spin-coated on a sacrificial Omnicoat layer at 500 rpm (ramp rate of 100 rpm/s) for 5 sec, followed by 2000 rpm (ramp rate of 100 rpm/s) for 30 sec. This was followed by pre-exposure baking at 65ºC for 2 minutes and 95ºC for 5 minutes. Then the composite was patterned using ultraviolet (UV) lithography by mask aligner (Karl Suss MJB3) for 35 sec (130 mJ/cm2 exposure energy). Samples were post-exposure baked at 65ºC for 2 minutes and 95ºC for 2 minutes. Then this was followed by patterning a layer of magnetic composite repeating the previous fabrication steps and then soaked in SU-8 developer (MicroChem®) to chemically remove uncrosslinked SU-8 from both layers. A final layer of pure SU-8 was then deposited over the entire structure and patterned using the same procedure, followed by a second development step. The freestanding microrobots with encapsulated magnetic core were attained.

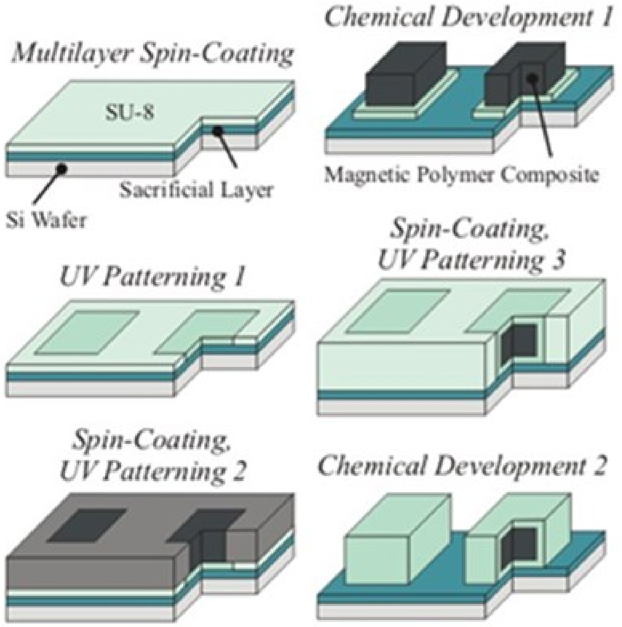

Figure 4.1 Hybrid microrobots fabrication process: Microrobots were created by spin-coating a thin sacrificial layer onto a silicon wafer, followed by deposition and patterning of layers of SU-8, magnetic composite, and another layer of SU-8 [121].

A variety of hybrid microrobot geometry was created; optical micrographs of several patterns are shown in Figure 4.2 (b)-(f). Using this method, we were able to create isolated magnetic islands within a larger SU-8 base (d), Janus particles displaying controlled heterogeneity of magnetic particle density (e), and large magnetic cores with high-resolution SU-8 features (f). The hybrid structures exhibited clean, vertical sidewall geometry similar to that observed with pure SU-8 patterning. Despite the multiple spin-coating and patterning steps, scanning white-light interferometry showed the top surfaces to be flat within 1 μm; profilometry data for the microrobots in Figure 4.2 (f) is shown in Figure 4.2 (g).

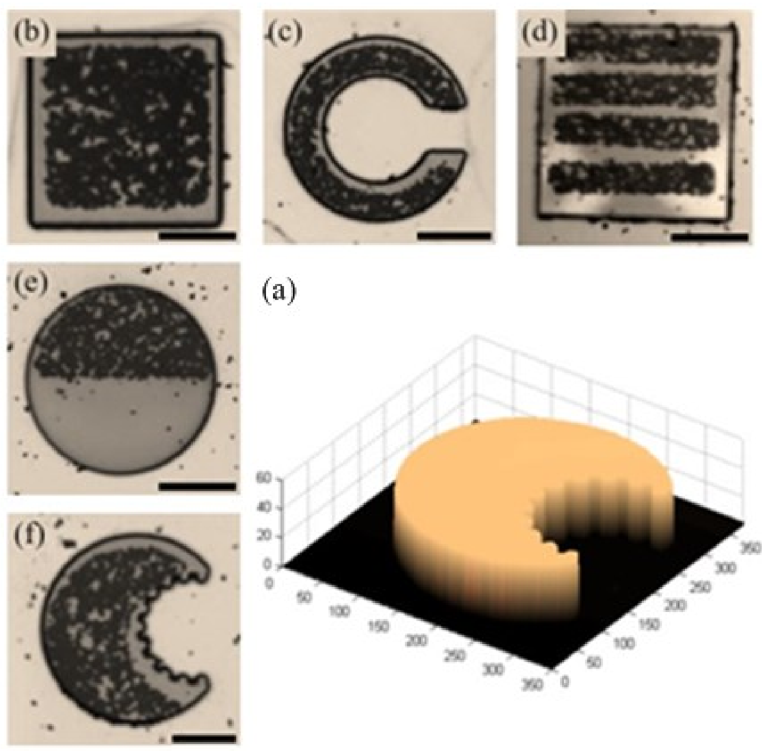

Figure 4.2 Hybrid microrobot microscopy images: (a) 3D profile of microrobot shown in (f); data obtained using scanning white light interferometry. (b)-(f) Optical microscopy images of hybrid microrobots; scale bar = 100 μm [121].

The hybrid magnetic structures are also biocompatible and chemically resistant because the magnetic microparticles are completely encapsulated inside an inert SU-8 layer. Complete internalization of particles cannot be guaranteed when using any photopatternable composite and single-layer deposition/patterning, because particles are immobilized in the composite during the pre-exposure-bake processing step prior to patterning. When the geometry is then defined by UV lithography, it is statistically likely that some particles will fall on the boundary of the UV-exposed area and will remain partially-imbedded in the material sidewalls when the composite is developed. The hybrid fabrication method encapsulates the composite regions in pure SU-8, which has been shown elsewhere to have excellent chemical resistance [44] and biocompatibility [153] . In addition, because the dissimilar SU-8 and composite layers show excellent adhesion to one another, it may be possible to use this method to combine the polymer micromagnetic structures demonstrated here with other SU8-based functional

composites, such as those containing silver nanoparticles [41], polytetrafluoroethylene (PTFE) [159], diamondoids [98] or carbon nanotubes [160].

4.3 Surface Characterization of Microfabrication Method

An array of fabricated microrobots is theoretically biplanar: the entire surface topography ideally lies on one of two parallel horizontal planes. This means that for all locations on the surface, the surface height η (x, y) takes on only one of two values: either η_{min} or η_{max}, where the difference between these two values is defined as the feature height, h_1 (i.e., $h_1 = \eta_{max} - \eta_{min}$). The encapsulated microrobots are one of those types of surfaces: we used a flat silicon wafer as the base layer (η_{min}) and used photolithography to add uniform-height polymer columns or plateaus (η_{max}). Because of the biplanar nature of this geometry, the method developed by Leachman, et al [161] can be used to analyze the surface topography and compare it to ideal values, thus giving a quantitative analysis of the fabrication accuracy.

4.3.1 Surface Texture Description

The microrobot fabrication technique described in previous section results in a surface comprised of a periodic array of features with uniform height (microrobots) on a flat surface (silicon wafer). While multiple microrobot geometries were investigated, all can be characterized using a feature area fraction parameter, which describes the ideal percentage of the overall surface area covered by microrobots. The general form of the feature area fraction (δ^2) is written as the ratio of the surface area of a single asperity (A_{asp}), which in this case is a microrobot, to the total area of the periodic unit cell (A_{cell}) that comprises the array:

$$\delta^2 = \frac{A_{asp}}{A_{cell}} \qquad 4.1$$

The feature surface area for a known geometry is determined by integration; for example, for the c-channel geometry shown in Table 4.1, this area is a function of the inner and outer radii (R_1 and R_2) and the included angle of the opening (α):

$$A_{c-channel} = \int_{0}^{2\pi-\alpha} \int_{R_1}^{R_2} r dr d\theta = \frac{(2\pi - \alpha)\left({R_2}^2 - {R_1}^2\right)}{2} \qquad 4.2$$

Assuming a square unit cell with side length L, the feature area fraction for a surface with periodic c-channel features simplifies to the following equation:

$$\delta^2{}_{c-channel} = \frac{(2\pi - \alpha)\left({R_2}^2 - {R_1}^2\right)}{2L^2} \qquad 4.3$$

Feature area fraction equations for several common deterministic surface features were calculated using this method and the results are summarized in Table 4.1.

Table 4.1 Feature Area Fraction [161]

Unit Cell	Description	Feature Area Fraction, δ^2	Max Value
	Circle	$\frac{\pi R_0^2}{L^2}$	0.785
	Square	$\frac{s^2}{L^2}$	1.000
	C-Channel	$\frac{(2\pi - \alpha)\left[{R_2}^2 - {R_1}^2\right]}{2L^2}$	0.785
	Crescent[a] ($b > R_2$)	$\frac{\pi {R_2}^2 - {R_2}^2 \cos^{-1}\left(\frac{x}{R_2}\right) - {R_1}^2 \cos^{-1}\left(\frac{b-x}{R_1}\right) + \frac{b}{2}}{L^2}$	0.785
	Crescent[a] ($b < R_2$)	$\frac{\pi\left({R_2}^2 - {R_1}^2\right) - {R_2}^2 \cos^{-1}\left(\frac{x}{R_2}\right) + {R_1}^2 \cos^{-1}\left(\frac{b-x}{R_1}\right) + \frac{ba}{2}}{L^2}$	0.785
[a] $x = \frac{1}{2b}\left({R_2}^2 - {R_1}^2 + b^2\right)$; $a = \frac{1}{b}\sqrt{4{R_2}^2 b^2 - \left({R_2}^2 - {R_1}^2 + b^2\right)^2}$			

4.3.2 Areal Surface Parameters for Biplanar Surfaces

Leachman, et al [161] developed a method for analyzing deterministic biplanar surfaces, such as the arrays of microrobots in this thesis. These surfaces can be characterized using twelve common areal surface parameters, which are listed with equations in Table 2. This grouping consists of a mix of roughness, hybrid and functional parameters; each of these parameters is described in detail in reference [162].

For perfect deterministic surfaces it is possible to determine closed-form expressions for eleven of the areal surface parameters as a function of the feature height h_1 and the feature area fraction δ^2. For an ideal surface covered with asperities, the residual surface height (η) when measured with respect to the least-squares datum plane can be expressed as the following:

$$\eta = \begin{cases} \eta_{top} = h_1(1-\delta^2) \\ \eta_{bottom} = -h_1\delta^2 \end{cases} \tag{4.4}$$

The general form of the RMS roughness (S_q) equation when analyzing a surface with area A_{cell} is:

$$S_q = \sqrt{\frac{1}{A_{cell}} \iint \eta^2 dA} \tag{4.5}$$

The residual surface height can only have one of two values at any given location—either η_{top} on the areas of the surface where asperities exist, or η_{bottom} on the areas where no features exist. Because of this, the RMS equation can be written as a function of these values:

$$S_q = \sqrt{\frac{1}{A_{cell}} \iint \eta^2 dA} = \sqrt{\eta_{top}{}^2\delta^2 + \eta_{bottom}{}^2(1-\delta^2)} \tag{4.6}$$

Combining this with equation 4.4:

$$S_q = \sqrt{\left(h_1(1-\delta^2)\right)^2\delta^2 + (-h_1\delta^2)^2(1-\delta^2)} \tag{4.7}$$

This expression can be simplified to the following:

$$S_q = h_1\sqrt{\delta^2(1-\delta^2)} \qquad 4.8$$

Following this general method, closed-form solutions were derived for eleven of the areal surface parameters; the solutions are summarized in Table 4.2 [161][REF]. These represent the target values for manufacturing the surfaces examined later in this section. It should be noted that these solutions are derived for surfaces covered in arrays of asperity features; for cavity-based surfaces, the feature area fraction (δ^2) and feature void fraction ($1-\delta^2$) must be reversed [161]. Finally, Figure 4.3 shows graphically the relationship between feature area fraction and six of the surface parameters (S_a, S_q, S_{sk}, S_{ku}, S_{bi}, and S_{ci}) for asperity surfaces.

Table 4.2 Closed Form Solutions for Surface Parameters [161]

Description	Definition	Closed Form Solution for Ideal Value[a]
Max. Height	$\eta_{\max} = \max[\eta(x,y)]$	$h_1(1-\delta^2)$
Min Height	$\eta_{\min} = \max[\eta(x,y)]$	$-h_1\delta^2$
Avg. Roughness	$S_a = \frac{1}{MN}\sum_{j=1}^{N}\sum_{i=1}^{M}\lvert\eta(x_i,y_i)\rvert$	$2h_1\delta^2(1-\delta^2)$
RMS Roughness	$S_q = \sqrt{\frac{1}{MN}\sum_{j=1}^{N}\sum_{i=1}^{M}\eta^2(x_i,y_i)}$	$h_1\sqrt{\delta^2(1-\delta^2)}$
Peak-to-Valley	$\max[\eta(x,y)] - \min[\eta(x,y)]$	h_1
10 Pt. Height	$S_z = \frac{\sum_{i=1}^{5}\lvert\eta_{pi}\rvert + \sum_{i=1}^{5}\lvert\eta_{vi}\rvert}{5}$	h_1
Skewness	$S_{sk} = \frac{1}{MN{S_q}^3}\sum_{j=1}^{N}\sum_{i=1}^{M}\eta^3(x_i,y_i)$	$\frac{1-2\delta^2}{\sqrt{\delta^2(1-\delta^2)}}$
Kurtosis	$S_{ku} = \frac{1}{MN{S_q}^4}\sum_{j=1}^{N}\sum_{i=1}^{M}\eta^4(x_i,y_i)$	$\frac{[\delta^2]^3+[1-\delta^2]^3}{\delta^2(1-\delta^2)}$
Texture Direction	$S_{td} = \begin{cases} -\beta & \beta \le \frac{\pi}{2} \\ \pi-\beta & \frac{\pi}{2} < \beta \le \pi \end{cases}$	Compute from PSD, where β is a single or group of dominant angles within the texture
Bearing Index	$S_{bi} = \frac{S_q}{\eta_{0.05}}$	$\sqrt{\frac{\delta^2}{(1-\delta^2)}}\ \ for\ \ \delta^2 > 0.05$
Core Index	$S_{ci} = \frac{V_c}{S_q}$	$\sqrt{\frac{(1-\delta^2)}{\delta^2}}\ \ for\ \ \delta^2 > 0.05$
Valley Index	$S_{vi} = \frac{V_v}{S_q}$	$\Rightarrow 0\ \ for\ \ \delta^2 < 0.80$

[a]Listed equations are for asperity-based surfaces; for cavity-based surfaces, simply switch δ^2 and $(1-\delta^2)$

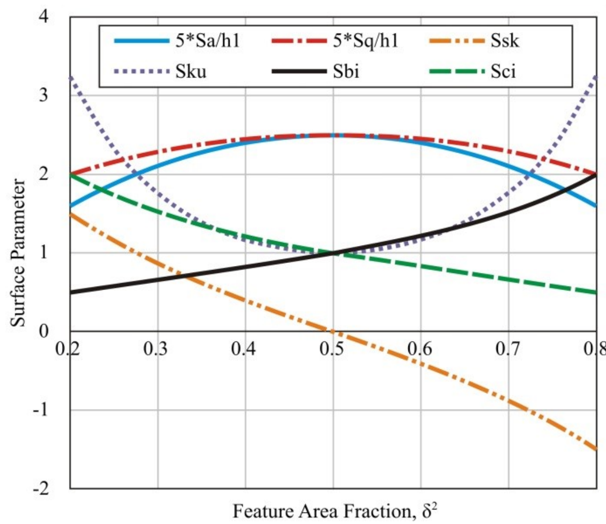

Figure 4.3 Closed form solutions for surface parameters as a function of feature area fraction for asperity-covered surfaces [163].

4.3.3 Surface Analysis Results and Discussion

Five hybrid microrobot geometries were fabricated and analyzed, including two square geometries with different internal metal localization and three circle-based geometries (Janus, crescent and c-channel); these features are shown in Figure 4.4. These textures are interesting because they not only are comprised of unique deterministic shapes, but they also possess customized material properties based on the ratio of metal impregnation to polymer base and can be made non-isotropic and directional. For instance, the Janus geometry is loaded with a high volume ratio of metal particles on the top of the figure and a very low volume ratio on the bottom, and the “Square 1” geometry orients the metal filler in the horizontal direction.

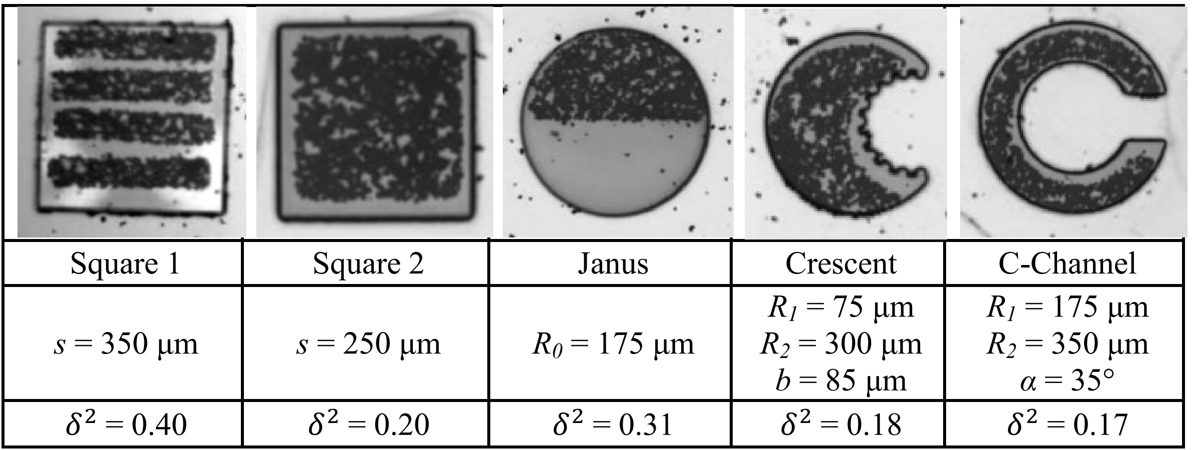

Square 1	Square 2	Janus	Crescent	C-Channel
s = 350 μm	s = 250 μm	R_0 = 175 μm	R_1 = 75 μm R_2 = 300 μm b = 85 μm	R_1 = 175 μm R_2 = 350 μm α = 35°
δ^2 = 0.40	δ^2 = 0.20	δ^2 = 0.31	δ^2 = 0.18	δ^2 = 0.17

Figure 4.4 Microrobot geometries of height h_1 = 45 μm (Square and Janus features) or h_1 = 40 μm (Crescent and C-Channel features). Each shape is patterned into an array with a unit cell length of L = 550 μm [161].

The surface topography of microrobot arrays was measured using a Zygo Newview 5000 Interferometer. Raw data from the Zygo measurements was processed using a custom Matlab code that removed any parallelism errors in measurement and zeroed the data with respect to the least-squares mean plane before using it to calculate the areal surface parameters listed in Table 4.2. The original designed surface geometry was used with the data in Table 4.1 to determine feature area fraction for each surface type, and combined with the equations in Table 4.2 to calculate ideal areal parameters for each engineered surface. The summarized surface parameter measurements for the polymer asperity patterns in the as-manufactured state are given in Table 4.3 below. These values are also compared to the ideal values—assuming the surfaces were perfectly manufactured—and to values for surfaces with a Gaussian surface roughness of the same S_q value as the deterministic pattern.

Table 4.3 Typical Measurement Data for Polymer Asperity Surfaces [161]

Description	Gauss.	Square 1 Ideal	Square 1 Mfg.	Square 2 Ideal	Square 2 Mfg.	Janus Ideal	Janus Mfg.	Crescent Ideal	Crescent Mfg.	C-Channel Ideal	C-Channel Mfg.
Avg. Roughness, S_a (μm)	17.62	21.58	21.66	14.59	14.43	19.36	19.80	11.84	11.53	11.35	11.66
RMS Roughness, S_q (μm)	22.03	22.03	21.92	18.12	18.32	20.87	20.98	15.39	15.32	15.07	14.63
Ratio (S_a/S_q)	1.25	1.02	1.01	1.24	1.27	1.08	1.06	1.30	1.33	1.33	1.26
PV Value, S_t (μm)	36.01	45.00	45.55	45.00	47.91	45.00	47.22	40.00	42.22	40.00	38.90
10 Pt. Height, S_z (μm)	33.12	45.00	45.39	45.00	47.82	45.00	46.17	40.00	41.90	40.00	38.72
Skewness, S_{sk}	0.007	0.41	0.26	1.47	1.56	0.81	0.69	1.66	1.74	1.75	1.50
Kurtosis, S_{ku}	3.00	1.17	1.08	3.17	3.44	1.65	1.48	3.76	4.05	4.05	3.28
Bearing Index, S_{bi}	0.60	0.81	0.87	0.51	0.49	0.68	0.70	0.47	0.45	0.45	0.49
Core Index, S_{ci}	1.58	1.23	1.21	1.98	2.17	1.48	1.50	2.13	2.33	2.20	2.15
Valley Index, S_{vi}	0.11	0.00	3.3e-4	0.00	4.2e-4	0.00	3.9e-4	0.00	3.7e-4	0	5.6e-4

Table 4.3 summarizes measurement data for a typical result of each shape. For each case a different combination of asperity height and area fraction is desired, therefore, the ideal surface roughness parameters are given for each asperity type. For these surface textures it is seen that in every case presented the measured roughness parameters, S_q and S_a, are within 150 nm (<0.1%) of the ideal (desired) geometry. Figure 4.5 further illustrates the accuracy of the manufacturing process in reproducing the surface texture. Again, each measured surface parameter is close to its ideal value indicating excellent repeatability of the microrobot fabrication method. The value of S_{sk} is positive indicating a peak laden surface as is the case for asperity surfaces, such as the microrobot arrays.

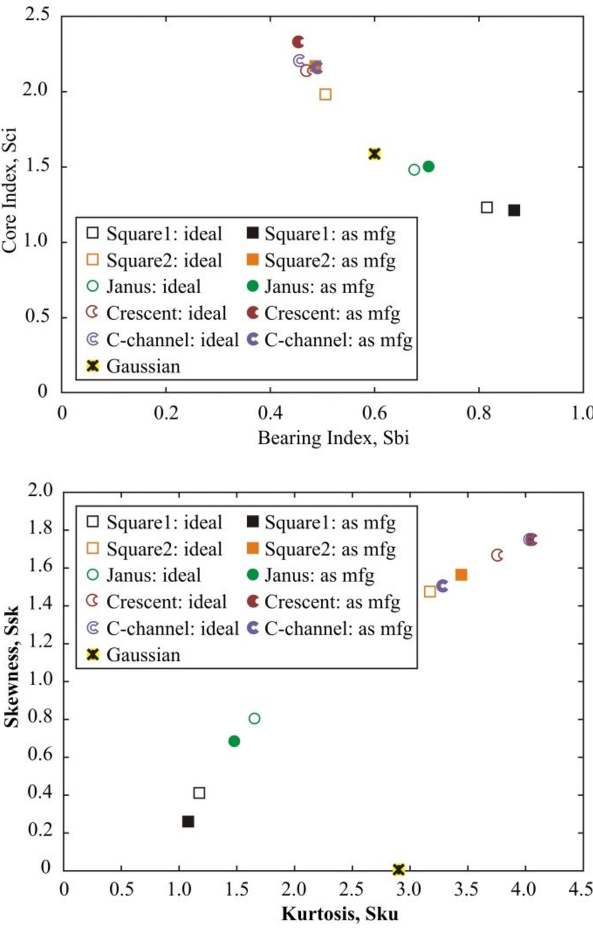

Figure 4.5 Calculated and ideal surface parameters for photolithography patterned microrobot arrays [161].

4.4 Force Calculations on Mobile Magnetic Microrobots

There are two basic ways to generate magnetic field: permanent magnets and electromagnets. Permanent magnets produce a high magnetic field with low mass and volume, and have high values of magnetic remanence and coercivity, making them stable against the influences which would demagnetize them. Electromagnetic solenoids can be used to generate eletromagnetic field as well, but the field is typical weaker than that generated by a permanent magnet of the same volume [164]. Both principles can be used to generate magnetic fields in a controlled way and have been applied in commercial applications, such as data storage device [165, 166] and MRI system [128].

The position and orientation of magnetic devices can be controlled in applied external magnetic field by magnetic force and torque. The magnetic field's flux density can be represented as:

$$\mathbf{B} = \mu_0 \boldsymbol{H} \quad 4.9$$

where $\boldsymbol{H}$ is the magnetic field strength, μ_0 is permeability of free space and $\mu_0 = 4\pi \times 10^{-7} H/m$. Paramagnetism is a form of magnetism of a material attracted by an externally applied magnetic field, and form internal, induced magnetic fields in the direction of the applied magnetic field. Diamagnetism is the opposite behavior that the material is repelled by magnetic fields and form induced magnetic fields in the direction opposite to that of the applied magnetic field. In the case of paramagnetism and diamagnetism, the magnetization $\boldsymbol{M}$ is often proportional to the applied magnetic field such that:

$$\mathbf{B} = \mu\,(\boldsymbol{H} + \boldsymbol{M}) \quad 4.10$$

where μ is the permeability of the medium, and when in vacuum, $\mu = \mu_0$.

The magnetization $\boldsymbol{M}$ is the magnetic dipole moment $\boldsymbol{m}$ per unit volume V, in amperes per meter. $\boldsymbol{M}$ can be written as:

$$\boldsymbol{M} = \boldsymbol{m}/V \quad 4.11$$

For linear and isotropic materials, the magnetization depends linearly on **H** such that

$$\boldsymbol{M} = \chi_m \boldsymbol{H} \quad 4.12$$

where χ_m is a dimensionless quantity (ratio of $\boldsymbol{M}$ to $\boldsymbol{H}$) called magnetic susceptibility of the medium. It is more or less a measure of how susceptible (or sensitive) the material is to a magnetic field [167]. Then, $\boldsymbol{B}$ can be written as

$$\boldsymbol{B} = \mu_0 (1 + \chi_m)\boldsymbol{H} = \mu_0 \mu_r \boldsymbol{H} \qquad 4.13$$

where μ_r is the ratio of a given material to that of the free space μ_0; and is called relative permeability of material. In general, χ_m and μ_r are not constant but change with the magnetization of the material. Both of them are generally used to classify materials in terms of their property or behavior [141, 164, 168-171]. A material is nonmagnetic if $\chi_m = 0$ $(or\ \mu_r = 1)$; otherwise, it is magnetic. And magnetic materials can be grouped into three classes by $\chi_m\ and\ \mu_r$: diamagnetic ($\chi_m < 0, \mu_r \leq 1$) paramagnetic ($\chi_m > 0, \mu_r \geq 1$), and ferromagnetic ($\chi_m \gg 0, \mu_r \gg 1$).

Diamagnetism happens when the magnetic fields in a material that are due to electronic motions of orbiting and spinning completely cancel each other. The permanent magnetic moment of each atom is zero and such materials are weakly affected by a magnetic field. On the other hand, atoms have nonzero permanent magnetic moment may be paramagnetic or ferromagnetic; and ferromagnetic materials have larger permanent magnetic moment than that in paramagnetic materials [167, 172]. Ferromagnetic materials are very useful in practice since they have great properties. They can be magnetized very strongly by a magnetic field and can retain their magnetization after the magnetizing field is taken away. The dependence of magnetization on external fields for a ferromagnetic material is shown in Figure 4.6 below.

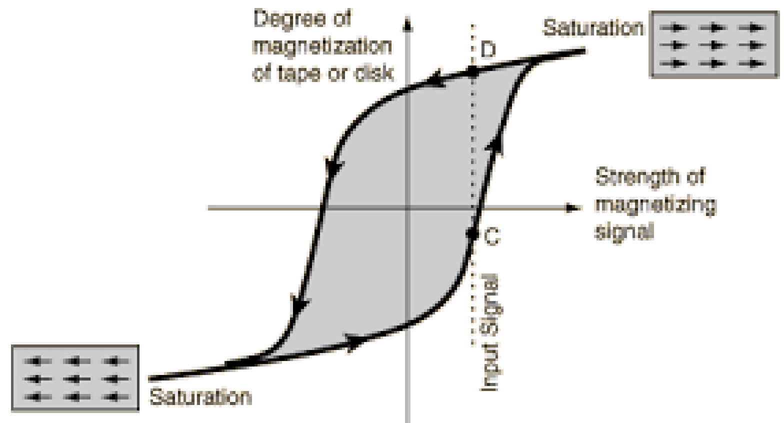

Figure 4.6 Typical magnetization (B - H) Curve [173].

Once a ferromagnetic material is magnetized, it will experience a torque $\boldsymbol{T}$ when in the presence of a magnetic field. The magnetic torque exerted on magnetic structure with uniform magnetization $\boldsymbol{M}$ in a magnetic field can be represented as:

$$\boldsymbol{T} = \boldsymbol{m} \times \boldsymbol{B} \text{ or } \boldsymbol{T} = V\boldsymbol{M} \times \boldsymbol{B} \qquad 4.14$$

where $\boldsymbol{m}$ is the magnetic moment, $\boldsymbol{B}$ magnetic field's flux density, and V is the volume of the magnetized object. With permanent magnets, the magnetic moment $\boldsymbol{m}$ is assumed to have a constant magnitude and be rigidly connected to the frame of the body [140],. The magnetic force on a permanent magnet in a magnetic field can be expressed as:

$$\boldsymbol{F_{mag}} = (\boldsymbol{m} \cdot \nabla)\, \boldsymbol{B} \text{ or } \boldsymbol{F_{mag}} = V(\boldsymbol{M} \cdot \nabla)\, \boldsymbol{B} \qquad 4.15$$

which can also be expressed as:

$$\boldsymbol{F_{mag}} = \left[\frac{\partial \boldsymbol{B}}{\partial x}\ \frac{\partial \boldsymbol{B}}{\partial y}\ \frac{\partial \boldsymbol{B}}{\partial z}\right]^T \boldsymbol{m} \text{ or } \boldsymbol{F_{mag}} = V\left[\frac{\partial \boldsymbol{B}}{\partial x}\ \frac{\partial \boldsymbol{B}}{\partial y}\ \frac{\partial \boldsymbol{B}}{\partial z}\right]^T \boldsymbol{M} \qquad 4.16$$

The permanent magnet is hundreds orders of magnitude bigger than the microrobots and it was positioned near the microrobot, the magnetic field near the microrobot was

assumed constant and uniform as shown in Figure 4.7 (a). The magnetic force applied on the magnetic microrobot in vertical direction can be calculated by Maxwell's pulling force formula [174, 175]:

$$\boldsymbol{F}_{\boldsymbol{mag}} = \frac{\boldsymbol{B} \cdot \boldsymbol{B}\, S}{2\mu_0}\, \boldsymbol{k} \qquad 4.17$$

where S is the cross-sectional area perpendicular to magnetic field $\boldsymbol{B}$. Magnetic flux ϕ flowing perpendicularly into a volume is the sum of integral of the normal component of the magnetic field's flux density through the cross-sectional area [176].

$$\phi = \int \boldsymbol{B}_{\boldsymbol{z}}(\boldsymbol{x}, \boldsymbol{y}) dx\, dy\ \cdot \boldsymbol{k} \qquad 4.18$$

When $B_z\ (x, y) = \boldsymbol{B}$ is constant over the cross section, this integral can be simpilified as

$$\phi = (\boldsymbol{B}S) \cdot \boldsymbol{k} \qquad 4.19$$

Magnetic reluctance R is that magnetic field causes magnetic flux to follow the path of least magnetic reluctance and can be given by

$$R = \frac{l}{\mu S} \qquad 4.20$$

where l is the length of the material in magnetic field direction, μ is the material permeability.

As shown in Figure 4.7 (b), when the magnet is moving in x-direction, the reluctance increases because more air appears in the flux path between the magnet and microrobot. This increase in reluctance generates a force called cogging force F_{cog} (or reluctance centering force) in horizontal plane that drags the microrobot into alignment position (minimum reluctance position) [176].

$$\boldsymbol{F_{cog}} = \frac{1}{2}\, \phi_g^2\, \frac{dR}{dx}\boldsymbol{i} \qquad 4.21$$

where ϕ_g is the air gap flux and R is the net reluctance seen by the flux ϕ_g, x is the displacement of the permanent magnet.

Microrobots that are in a fluid environment experience the magnetic driving force analyzed above in addition to gravitational, buoyancy, and fluid drag force ($\boldsymbol{F_g}, \boldsymbol{F_b}, \boldsymbol{F_{drag}}$, respectively) :

$$\boldsymbol{F_g} = \rho_m\, V\, \boldsymbol{g} \qquad 4.22$$

$$\boldsymbol{F_b} = -\, \rho\, V\, \boldsymbol{g} \qquad 4.23$$

where ρ and ρ_m are the density of the fluid and the magnetic microrobots, V is the microrobot volume, and $\boldsymbol{g}$ is gravitational acceleration. The net buoyancy force on microrobot is

$$\boldsymbol{F_{bnet}} = (\rho_m - \rho)V\boldsymbol{g} \qquad 4.24$$

If the microrobot is being moved in a horizontal plane, the net buoyancy force will be perpendicular to the direction of the microrobot's motion. If buoyant force is greater than or equal to the gravitational force, it will result in the microrobot floating in the fluid environment. The resulting speed of the microrobot is determined by the fluid drag force and magnetic force. The fluid drag force can be expressed as

$$\boldsymbol{F_{drag}} = -\frac{1}{2}\, \rho\, \boldsymbol{v} \cdot \boldsymbol{v}\, C_d\, A\, \boldsymbol{i} \qquad 4.25$$

where ρ is the fluid density, $\boldsymbol{v}$ is the microrobot velocity with respect to the surrounding fluid, A is the cross sectional area of the microrobot in the direction of movement, and C_d is the drag coefficient. C_d is related to the microrobot's geometry [177] as well as the fluid Reynolds number, Re.

$$Re = \frac{\rho \boldsymbol{v} L}{\eta} \quad 4.26$$

where ρ is the fluid density, $\boldsymbol{v}$ microrobot velocity with respect to the surrounding fluid, L is the length of the microrobot in the direction of movement, and η is the viscosity of surrounding fluid. The fluid drag force is area dependent, whereas magnetic and buoyancy forces are volumetric. So as the microrobots size decreases, the required field gradient to move at a particular speed rapidly increases. This is called the Reynolds number scaling effect [178], and in this case, Re increases exponentially and so does the drag force. So in this specific case, the fluid drag force would be relatively large since the microrobot's characteristic dimensions are in ten to hundreds of micrometers; therefore a strong magnetic field is needed to drive the microrobot.

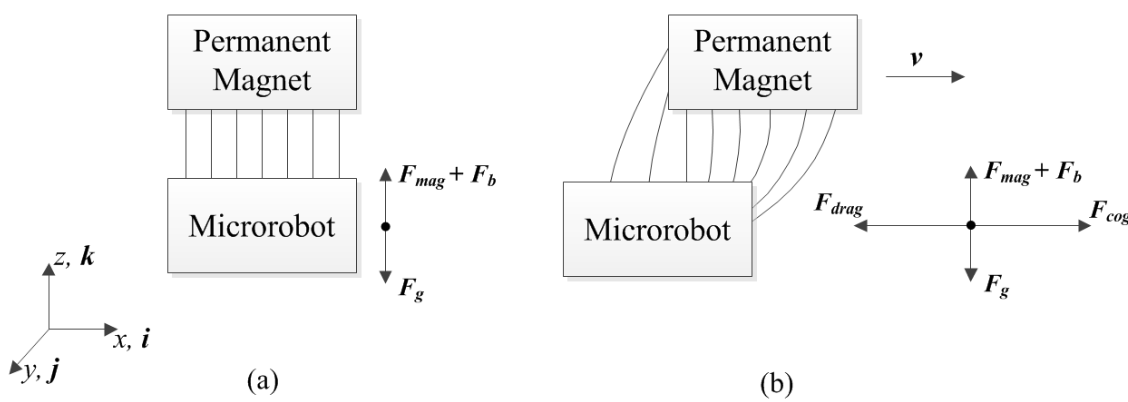

Figure 4.7 Free body diagrams of magnetic microrobot in fluid environment. (a) When the permanent magnet is static and aligned with the microrobot. (b) When the permanent magnetic is moving with a velocity v and misaligned with the microrobot which causes a cogging force $\boldsymbol{F_{cog}}$.

The steady-state locomotion of the microrobot under a given magnetic field in fluid environment would occur very quickly and the velocity can be estimated from:

$$\boldsymbol{F_{cog}} + \boldsymbol{F_{drag}} = 0 \qquad 4.27$$

Combining Equations 4.21, 4.25, and 4.27, the velocity of magnetic microrobots can be calculated as:

$$\boldsymbol{v} = \phi_g \sqrt{\frac{1}{\rho C_d A} \frac{dR}{dx}}\, \boldsymbol{i} \qquad 4.28$$

4.5 Remote Actuation of Magnetic Microrobots

In order to demonstrate contact-free actuation of magnetic microrobots, we used an external magnetic field to controllably move freestanding microrobots in a liquid environment, as shown in Figure 4.8 (a). In this figure, (1) is the control system frame, (2) is a movable permanent magnet, (3) is a petri dish with IPA that contains the microrobot, (4) is the bottom surface of the petri dish that contains a printed desired path line, (5) is a holding stand for the petri dish, (6) are servo motors, and (7) is a microscope with camera. Figure 4.7 (b) shows the control interface. Figure 4.8 (b) shows the enlarged schematic diagram of locations of the permanent magnet and the microrobot in IPA contained in a petri dish.

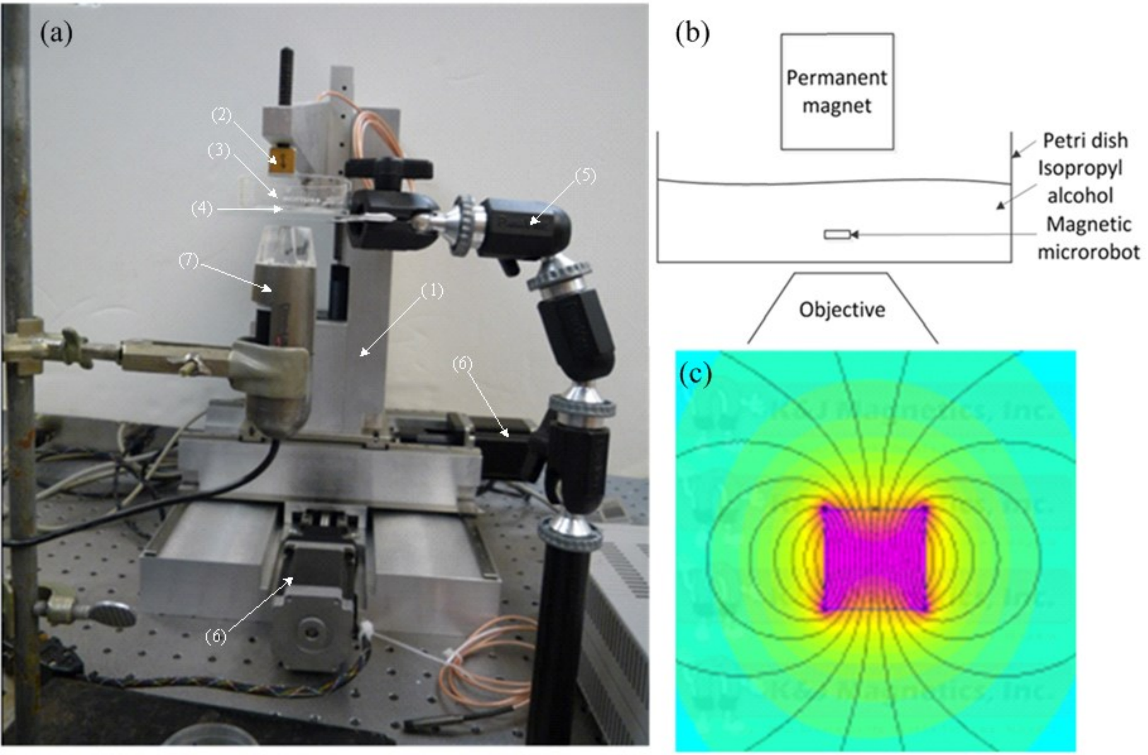

Figure 4.8 (a) Magnetic microrobots control setup. (b) Enlarged schematic diagram of locations of the permanent magnet and microrobot. (c) Visualization of the magnetic field generated by a permanent cubic magnet.

For this demonstration, polymer microrobots were released from the handling wafer as described previously and moved to a glass dish filled with isopropyl alcohol and an arbitrary pattern printed on the bottom surface. An external magnetic field was generated using a permanent magnet (NdFeB 42, 12 mm × 12 mm × 12 mm, K&J Magnetics) with surface field strength of 4200 G held at a distance of 10 mm from the microrobot; at this distance the strength of the magnetic field was approximately 700 G. The magnetic field of the cubic magnet is visualized in Figure 4.8 (c). The location of the permanent magnet was controlled remotely using a series of precision linear translation stages and used to guide the microrobot along a series of arbitrary courses. In the demonstration shown in Figure 4.9, the polymer microrobot was moved along the 30.5 mm long path shown in approximately 18 sec, resulting in an average speed of 1.7 mm/sec.

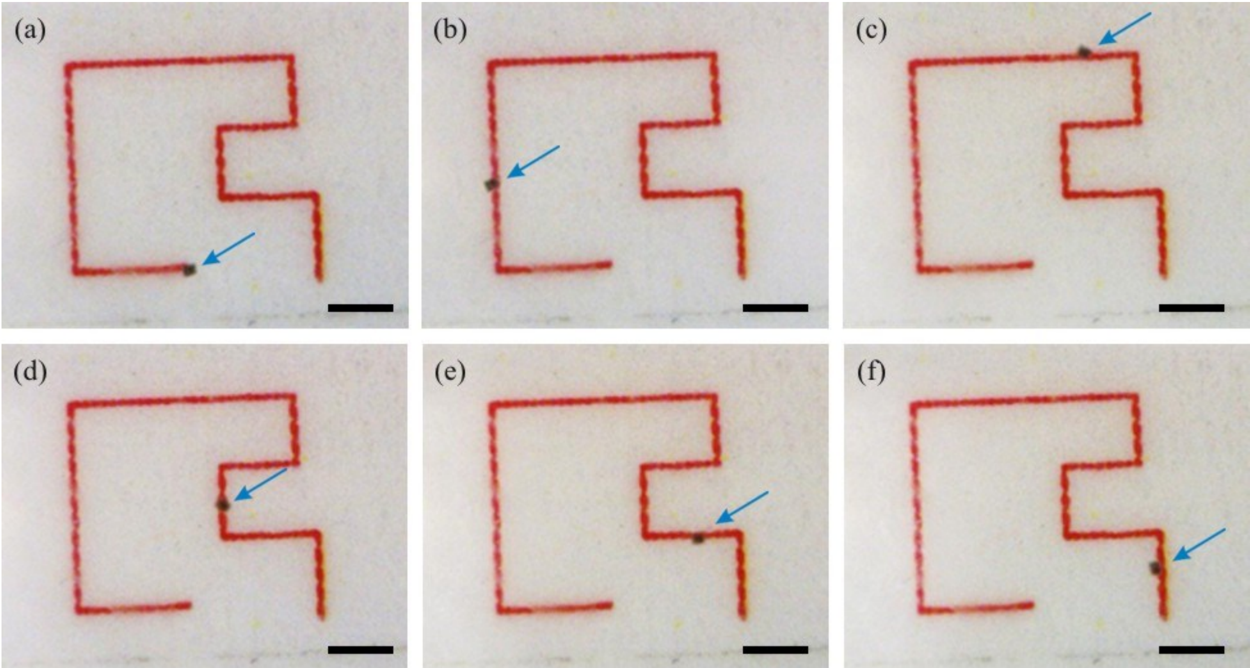

Figure 4.9 Time-lapse images of "swimming" magnetic polymer microrobot powered by external magnetic field; the robot completed the course in 18 seconds following the line 30.5 mm in length. Scale bar = 2 mm [121].

4.6 Summary

Hybrid microrobots with an encapsulated magnetic core surrounded by pure SU-8 were fabricated utilizing multilayer photolithography with a magnetic middle layer. The resulting microrobots are magnetically responsive while still being biocompatible and chemically resistant, making them suitable for a wide range of applications. Surface analysis of these microrobots was conducted to evaluate the fabrication process, and values were found to be within 1% of ideal fabrication values. The fabricated microrobots were also magnetically propelled in isopropanol alcohol along a desired path in order to demonstrate contact-free actuation; in this demonstration, the robots achieved an average speed of 1.7 mm/sec along a complex predefined path.

Chapter 5 Creation of Freestanding Three Dimensional Microstructures by Aligned Mask Micromolding

5.1 Introduction

Over the last few decades, there has been very active development in the fields of micro-electro-mechanical systems (MEMS) and microfabrication. This area of research has a wide variety of applications, from micro-gears [2, 3, 35] and micro-sensors/actuators [6], to drug delivery devices [7] and disease diagnostic tools [8, 9, 179]. Many potential MEMS/microfabrication applications require three dimensional microstructured components, but traditional photolithography microfabrication is limited to the creation of flat, layered geometries [10, 12].

Researchers have demonstrated a variety of methods for three dimensional microstructure fabrication, but all of these methods have limitations. One of the most established microfabrication methods—photolithography based processing originally developed for integrated circuit fabrication—excels in the area of precision but is fundamentally limited to creating 2D features [13]. A variety of 3D microprototyping methods have recently been demonstrated [14-16], but these have limitations in throughput, quality, and the geometry and material types that can be processed. Inclined and rotated UV lithography with micromolding can yield some specific three dimensional microstructures [180], but it is impossible to fabricate three dimensional microstructures with curvature, such as micro-hemispheres. Roll-to-roll micro- and nanofabrication excel in high-throughput production [18-20], but it is challenging to create film-free materials with this processing type or to use highly viscous materials. Greyscale photolithography is capable of creating 3D microstructures, but geometry and material types are very limited [64].

One possible alternative is 3D micromolding. Microscale polymer molding has become a ubiquitous fabrication method due to its numerous advantages: high

fabrication throughput, large breadth of available material properties, low cost due to the economics of scale, and wide variety of producible geometry. It would be beneficial to extend these advantages to the microscale, but defect-free processing is difficult because of film/flash.

One of the primary challenges in micromolding and microforming-style processes is the elimination of unwanted connecting film or "flash" between parts that results from overfilling mold cavities. Because the internal volume of micromolding cavities tends to be in the picoliter to femtoliter range, it is unrealistic to control injection volume to fill mold cavities precisely enough to eliminate overflow; this problem becomes exacerbated when large arrays of cavities need to be filled, as in highly-parallel micromolding processes that can have thousands or millions of cavities per mold. Micromolding cavities are typically filled by imprinting rigid mold into a liquid or solid polymer layer; material is forced into the cavities and any excess polymer remaining when closing pressure is applied forms a film or "flash" around the edge of the part.

Previous methods of eliminating flash in micromolding involve postprocessing steps to remove excess material, or controlling cavity filling with surface tension or microchannels. The first method works best with 2D, planar geometry and requires additional processing time and equipment [181, 182]. Using surface wettability to control cavity filling only works with low-viscosity polymers and leaves a distinct "dimple" defect on the reverse side of the part [183, 184]. Capillary-based mold filling uses a series of microfluidic channels to fill closed mold cavities [51, 56, 185]—similar to a sprue/runner system in microscale molding—but this method inherently leaves all the final parts interconnected after molding, and there is no straightforward way to remove the interconnecting channel material.

5.2 Materials and Methods

The research demonstrated here overcomes the film/flash issue by developing a method called Aligned Mask Micromolding (AMM). This method uses nanocomposite

polymers that solidify when exposed to UV radiation and selectively exposes only the material within the mold cavities to this radiation; the excess polymer can simply be washed away between molding cycles, or in some cases reused. Virtually any photoactive polymer can be used as the base material in the nanocomposite, from biocompatible hydrogel materials [186-188] to high strength epoxy-based compounds [43], including the magnetic composite described in chapters 3 & 4. And because many material properties can be tuned by the addition of nanoparticles to the base—strength [98, 189], wettability [159], electrical conductivity [41, 190], magnetic response [121]—these nanocomposite materials can be fine-tuned for a wide variety of applications.

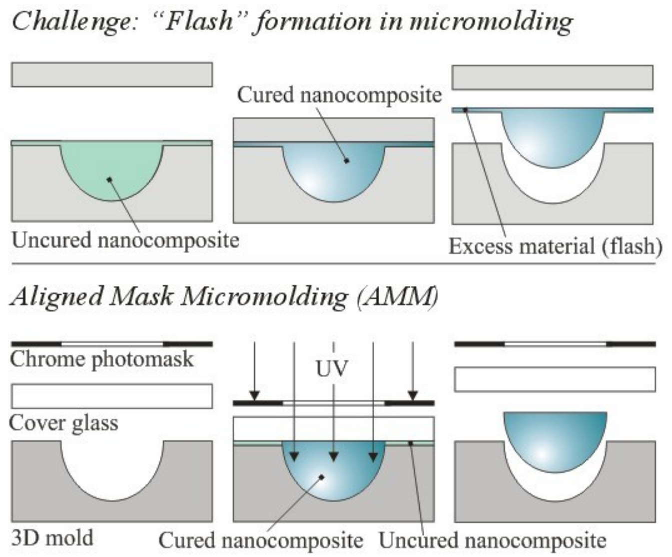

Figure 5.1 Flash formation in micromolding versus flash-free micromolding using AMM.

The Aligned Mask Micromolding (AMM) method demonstrated here is a low-cost method that aligns a separate chrome photomask with 3D micromolds in order to prevent UV crosslinking of extra material outside the mold cavities, as shown in Figure 5.1. The transparent regions of the photomask allow penetration of UV light from a columnated source, causing the material to crosslink and become rigid; the regions shielded from UV exposure—those outside the mold cavity—remain soluble and can easily be removed after the mold is removed. An additional benefit of this method is that the mask geometry is decoupled from the micromold, making it possible to use different photomask patterns to create unique 3D geometry from the same mold.

A polymer mold was used in the AMM process, since polymer molds are cheap, replaceable, and easy to remove without damaging the molded component [191]. A nickel mold with micro-milled three dimensional microstructured cavities was used as the original master mold, and additional polymer molds were created from this geometry by using a casting process and a soft polymer: polydimethylsiloxane (PDMS). First, an intermediate PDMS mold with positive 3D microstructured cavities was created from the nickel geometry, and then the final polymer mold copy was fabricated from the intermediate PDMS mold, as shown in Figure 5.2 (a).

Dow Corning 184 Sylgard silicone elastomer kit was used to fabricate the PDMS molds. The PDMS was prepared by combining the silicon elastomer base and the curing agent in a 10:1 ratio in a clean plastic cup and mixing vigorously for 3 minutes. The mixture was then degassed by placing it in a vacuum (Thermo Scientific) of 10 psi for 1 hour. The degassed PDMS liquid was poured over the nickel master mold and then degassed for another 1 hour to remove any additional bubbles. Once degassed, the assembly was placed in an oven (Quincy 40 GC lab oven) at 70 C for 4 hours to completely cross link the PDMS. Once set, the assembly was removed from the oven and allowed to cool to room temperature, followed by slowly and gently peeling off PDMS mold from the nickel mold, taking care not to tear the PDMS mold. The process was then repeated, but this time using the intermediate PDMS mold in place of the master mold, thus creating the final PDMS polymer mold.

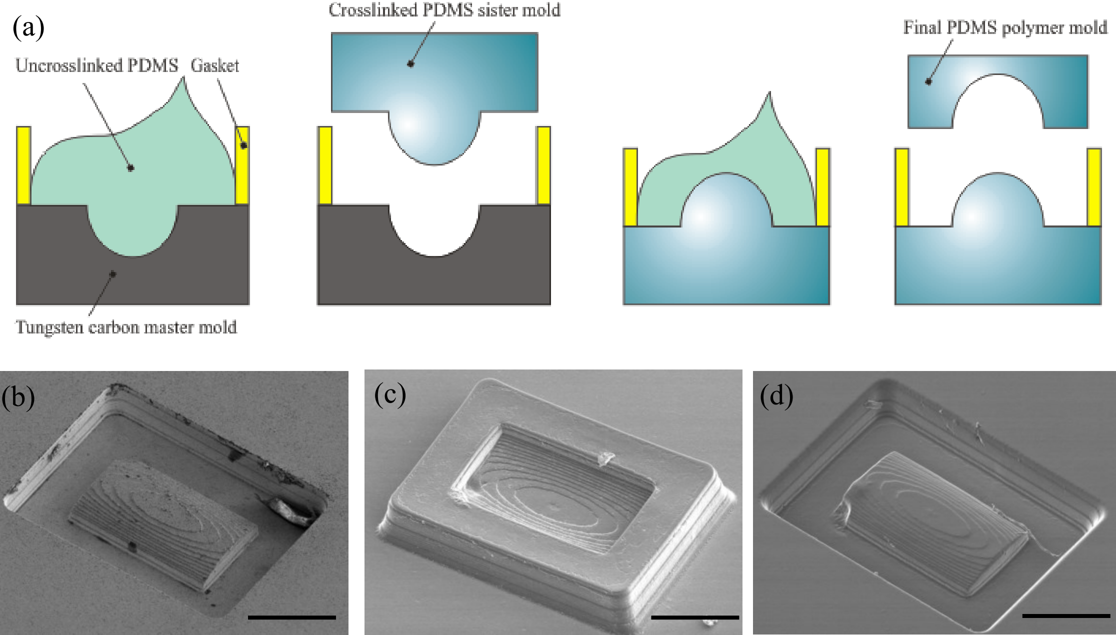

Figure 5.2 Final negative PDMS mold fabrication process and microscopy images. (a) Polymer mold copy fabrication process. (b) SEM image of original tungsten carbide negative master mold (provided by AMT Nano, LLC). (c) SEM image of PDMS positive sister mold. (d) SEM image of PDMS final polymer mold copy. All scale bars = 100 µm.

Once PDMS molds were fabricated, freestanding three dimensional microstructures were created using the process shown in Figure 5.1. First, a microscope cover glass (Thermal Scientific, 22mmx22mm) was coated with a sacrificial layer (Omnicoat, MicroChem) by spin-coating (Brewer Scientific Cee 100) at 500 rpm for 5 s and 3000 rpm for 30 s, followed by baking at 200 C for 1 min, according to the manufacturer's recommendations. Then SU-8 negative photoresist (MicroChem) with 1050 mm^2/s kinetic viscosity was applied to the PDMS mold and covered with the cover glass. The assembly was pre-exposure baked at 75 ºC for 4 hours, followed by 85 ºC for 2 hours, and 95 ºC for 30 minutes. After cooling to room temperature, the assembly and corresponding photomask were aligned using a mask aligner (Karl Suss MJB3) and exposed to 365 nm wavelength UV light for 7.5 minutes. The exposed assembly was post-exposure baked at 75 ºC for 3 hours, followed by 85 ºC for 1.5 hours, and 95 ºC for 30 minutes. Before the set cooled down to room temperature, the PDMS mold and the cover glass with microstructures were separated. Then the cover glass was soaked in

SU-8 developer (MicroChem) for 20 minutes under gentle agitation to remove the uncured SU-8 material and attain the freestanding microstructures.

5.3 Demonstration of Film-Free Micromolding

Film-free arbitrary geometric three dimensional microstructures were created by the Aligned Mask Micromolding (AMM). AMM eliminates the formation of unwanted film by aligning the transparent geometries of the photomask with the micromold cavities. This prevents the excess UV-sensitive material from being exposed to UV radiation, so it remains uncrosslinked. The UV light penetrated the transparent regions of the mask and solidified the material in the cavities; the excess material between PDMS mold and cover slip was covered from UV light, which was not crosslinked and can be easily developed.

Freestanding polymer microhemispheres were created by using this method; SEM micrographs of the mold and features are shown in Figure 5.3. The freestanding microcomponents replicated the features of the original nickel mold, including the machining grooves, metal protrusion, and the burr formation around the edge. All geometric measurements of both the metal mold microhemisphere cavity and the aligned mask micromolded microhemisphere were made using a stylus profilometer; the results of this data are discussed in section 5.5. These measurements showed that the error between the original mold cavity geometry and the final component geometry is approximately 3%.

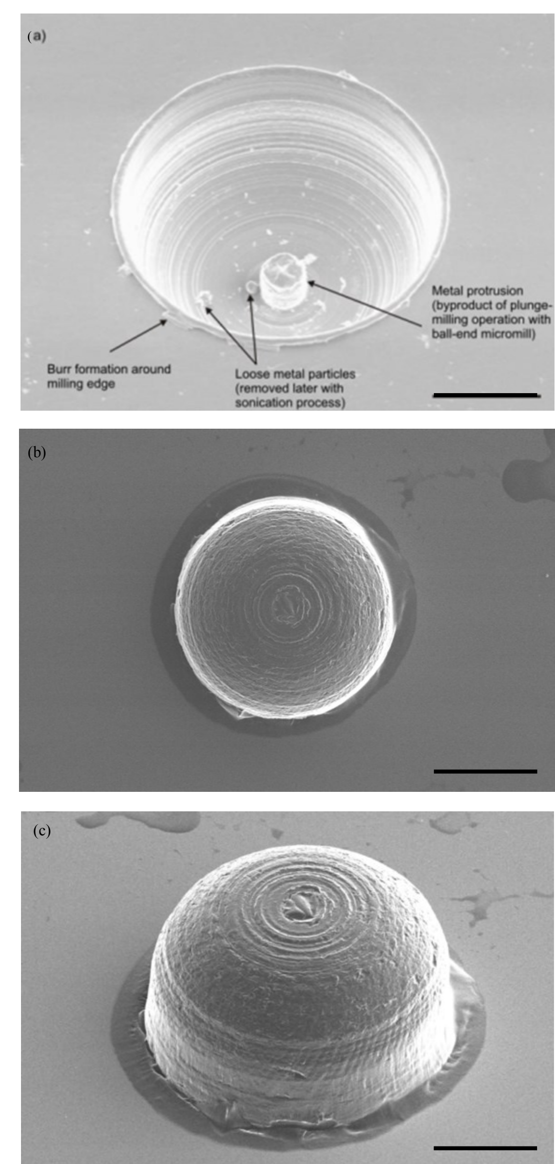

Figure 5.3 (a) SEM image of micromilled hemisphere cavity of original nickel mold [192]. (b, c) SEM images of freestanding SU8 three dimensional microhemisphere by AMM; sacle bars = 150 µm.

Although these 3D microhemispheres were fabricated to be film-free, some anticipated spread of the collimated UV light occurred, caused by the separation distance between the chrome photomask and molded structures. This causes a small amount of

material to be crosslinked just outside the area of the mold, as can be seen in Figure 5.6 (b) & (c). This error was estimated by:

$$Error = \sqrt{k\lambda g} \qquad 5.1$$

where k is a process parameter generally ≈ 0.8, λ is the wavelength of exposure radiation, and g is the gap between the mask and features [193]. In this case, the wavelength was 365 nm and the gap was estimated 150 µm, and this resulted in about 6.6 µm film.

5.4 Film Thickness Measurements

Using traditional micromolding processes it is impossible to control the volume of material filling a mold cavity precisely to avoid overflowing. The excess material overflows outside the mold cavities and becomes unwanted film. In the process described in the previous section, film formation is avoided by only exposing the area within the mold cavities to UV light, so the regions outside the mold never solidify. However, it is still important to quantify the thickness of the material that would have become film, because it adds to the overall height of the feature created during the micromolding process.

Film thickness was characterized by micromolding an SU8 component using the freestanding microstructure fabrication process described in the previous section, but using a photomask that intentionally exposed regions larger than the mold cavity. The original mold and resulting component/film structures are shown in Figure 5.4.

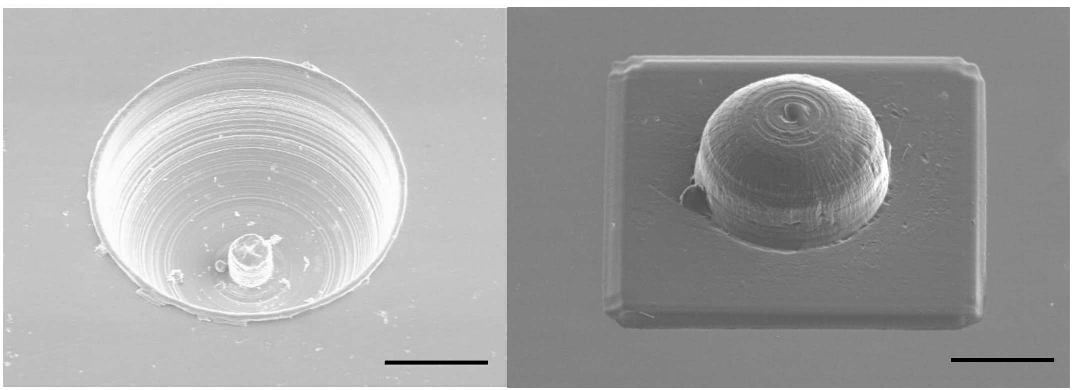

Figure 5.4 SEM images of original metal mold (left) [192] and SU-8 molded component with surrounding film (right); scale bars = 150 μm.

In order to characterize the effect material viscosity and force have on film thickness, polymer microcomponents were fabricated with two different SU8 formulations: SU8 10 with a kinematic viscosity of 1050 mm^2/s and SU8 2000.5 with a kinematic viscosity of 2.49 mm^2/s. force was applied during the pre-exposure baking process by employing a 100g weight on top of the cover slip and the PDMS mold with SU8 in the cavities. Samples were exposed intentionally by slight larger transparent squares on photomask. The height of each sample was measured using profilometer (Veeco, Dektak 6M) and the results are summarized in Figure 5.5. The material viscosity does increase the film thickness, especially when no force applied during pre-exposure baking; but in force applied case, the impact is minor.

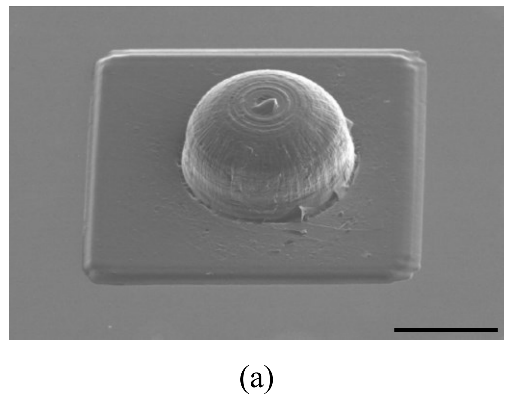

(a)

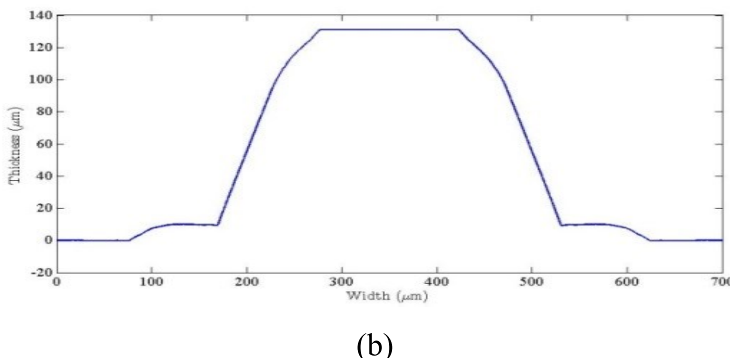

(b)

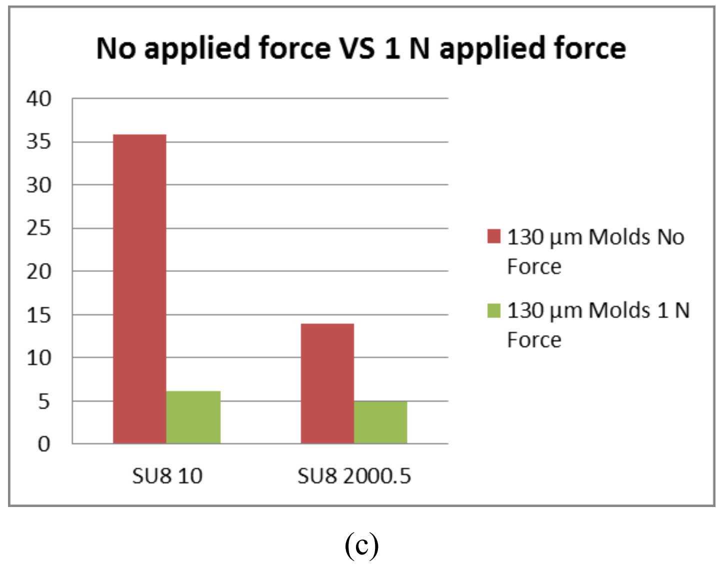

(c)

Figure 5.5 (a) SEM image of SU-8 with 2.49 mm^2/s kinetic viscosity micro-molded component with intentional film halo without force applied during pre-exposure baking. The scale bar = 150 µm. (b) Surface profile of SU-8 with 2.49 mm^2/s kinetic viscosity micro-molded component with intentional film halo without force applied during pre-exposure baking. (c) Film thickness vs. material viscosity with/without force during pre-exposure baking.

5.5 Solvent Loss Experiments

Experiments were carried out to characterize the effect on microcomponent geometry caused by molding material viscosity, applied external force and micromold cavity height. The SU-8 material used has a kinetic viscosity of 1050 mm^2/s and is widely used in microfabrication. The experiments were conducted by fabricating microfeatures using AMM as previously described, but performed using simple rectangular mold geometry. For some of the samples, force was applied to the mold/glass assembly during the pre-exposure baking step by adding a 100 g weight on top of slip cover, which is around 1 N force applied. UV exposure was performed on a mask aligner with columnated UV source and controllable exposure time (Karl Suss MJB3); and UV intensity was measured before each exposure to determine total exposure dose for each experiment. The height of the resulting polymer microstructures and original micromolds were measured using a stylus profilometer, and the results are summarized in Figure 5.6. And Table 5.1 shows the SU-8 10 material properties from manufacturer.

Table 5.1 Properties of SU-8 series 10

Material	Solids (%)	Viscosity (Cst)
SU-8 10	59	1050

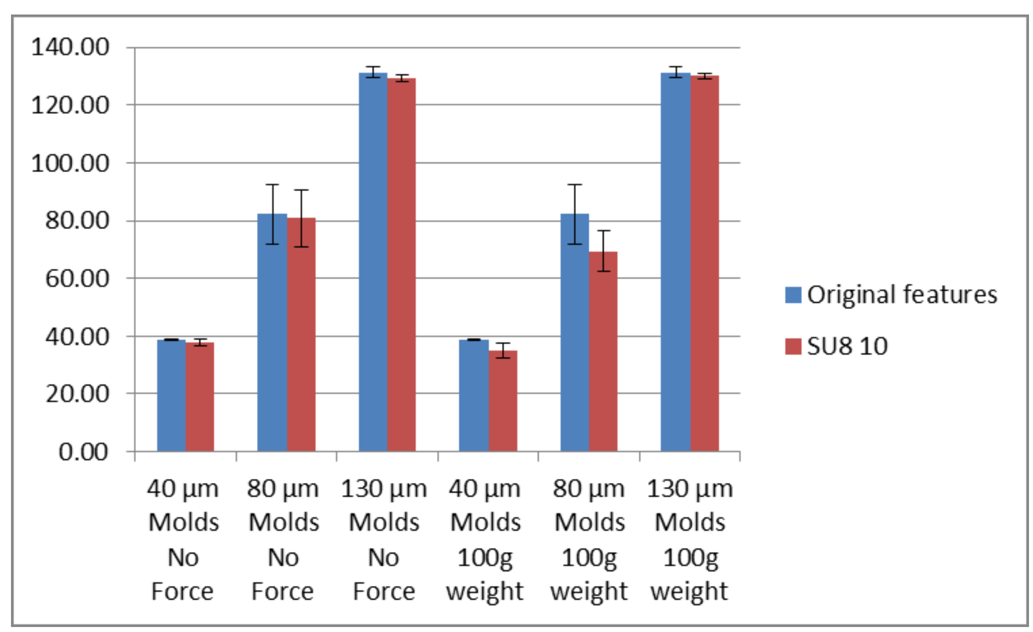

Figure 5.6 Solvent loss for AMM processing of SU-8 10 with/without applied force.

The difference in height between molded structures and the original molds (as seen in Figure 5.6) can be attributed to a combination of thermal expansion and solvent loss in the SU-8. During the pre-exposure baking step, the mold and SU-8 material are heated to an elevated temperature, causing the system to expand and solvent from the liquid SU-8 material to evaporate. Micro-components molded from lower-height micromolds lost less thickness than from higher-height micromolds. For the sets of samples where force was applied during prebaking, microstructures were thinner than the samples without force, most likely due to deformation of the molds caused by the applied force.

5.6 Summary

A novel, inexpensive, high through-put microfabrication method for the creation of film-free 3D microstructures was developed and demonstrated. This microfabrication method—Aligned Mask Micromolding (AMM)—used a combination of photolithography, micromolding and soft photolithography to fabricate freestanding polymer microstructures. Characterization of undesired film caused by material viscosity

and applied external force was conducted; and freestanding microstructures were also characterized for various materials and different micromolds.

Chapter 6 Conclusions and Future Work

6.1 Conclusions

The work described in this dissertation focused on the design and fabrication of polymer-based 2D and 3D microstructures with tunable material properties. Photopatternable Nd-Fe-B polymer micromagnets were fabricated using a magnetic polymer nanocomposite and photolithography. This method was expanded to create magnetic microrobots with encapsulated magnetic cores using a multilayer microfabrication method. These microrobots were wirelessly actuated in a fluid environment by an external magnetic field. A novel microfabrication method for arbitrary three-dimensional microstructures was also developed by combining lithography, micromolding and soft lithography.

The research described in chapter 3 focused on developing a facile microfabrication method creating for 2D polymer micromagnets that can be utilized in MEMS, microfluidics, microrobotics applications. A magnetic composite was prepared by mixing magnetic microparticles and SU-8 photoresist, which was then spin-coated onto a silicon wafer and patterned using UV photolithography. Using this method, micromagnets can be patterned using standard microfabrication equipment, making them inexpensive to manufacture and requiring limited equipment to produce. The method was capable of fabricating polymer micromagnets with 3 μm feature resolution and greater than 10:1 aspect ratio. The liquid SU-8/Nd-Fe-B composite material was characterized and it was found that magnetic particles within the polymer matrix could be dispersed uniformly by modulating spin speed during fabrication without requiring chemical modification of either of the two composite components.

The research described in chapter 4 focused on the creation and actuation of freestanding microrobots with encapsulated magnetic cores. These microrobots were

fabricated utilizing multilayer photolithography with a magnetic middle layer; the encapsulated of the magnetic core makes the microrobots biocompatible and chemically resistant for wide range of applications. Surface analysis of these microrobots was conducted to evaluate the fabrication process and estimate its effect on fluidic force when actuated in fluid environment in an applied external magnetic field. And it showed that the UV patternable photolithography methods reported less than a 1% error in manufacturing the ideal surface height geometries. The microrobots were magnetically actuated in isopropanol alcohol along a desired path and achieved an average speed of 1.7 mm/s, demonstrating that these microrobots could be remotely controlled with high accuracy in a liquid environment.

A novel, inexpensive, high throughput microfabrication method for creating freestanding three-dimensional microstructures with arbitrary size and geometry was developed in Chapter 5. This microfabrication method uses align mask micromolding and soft photolithography to fabricate freestanding microstructures with controllable 3D geometry. SU-8 photoresist was applied into 3D mold cavities and exposed through an aligned photomask. Characterization of undesired film caused by material viscosity and applied external force was conducted and it was found that film thickness can be controlled by either using low viscosity material or applying external force.

6.2 Future Work

The research presented in this dissertation offers critical insights for multi-dimensional freestanding microstructure fabrication, magnetic microrobot fabrication and wireless magnetic actuation for microfluidics and microrobotics applications.

The polymer microfabrication methods discussed in chapters 3-5 can be used to incorporate other SU-8 based functional composites into microstructures. These composites, such as those containing silver nanoparticles, polytetrafluoroethylene, diamondoids or carbon nanotubes [45, 190, 194, 195] offer a wide array of material properties. For example, silver nanoparticle composites can be used to make components

that are electrically conductive. Using these materials would expand the number of applications for this fabrication method and microscale parts in general.

In addition, the use of freestanding microstructures as microrobots can be explored further in future work. A wireless control system could be generated by an external electromagnetic field to produce complex, three-dimensional locomotion. The overall geometry of the microrobots could also be optimized by experimentally or numerically determining the drag coefficient to quantify the drag force and verify maximum achievable velocity.

Finally, the work in Chapter 5, which focused on the development and demonstration of aligned mask micromolding, could be extended to other geometries and high throughput. The geometry produced by this method is theoretically limited only by the mold geometry available. While this work demonstrated the creation of a simple hemisphere, aligned mask micromolding could be used to fabricate freestanding 3D microstructures with any shape, any size, and virtually any material.

References

1. White, R.D., L. Cheng, and K. Grosh, *Microfabrication of coupled fluid–structure systems with applications in acoustic sensing.* Sensors and Actuators A: Physical, 2008. **141**(2): p. 288-298.
2. Tang, Y., et al., *Micro-mould fabrication for a micro-gear via vacuum casting.* Journal of materials processing technology, 2007. **192**: p. 334-339.
3. Imbaby, M. and K. Jiang, *Stainless steel–titania composite micro gear fabricated by soft moulding and dispersing technique.* Microelectronic Engineering, 2010. **87**(5): p. 1650-1654.
4. Johnson, M.L., et al., *A wireless biosensor using microfabricated phage-interfaced magnetoelastic particles.* Sensors and Actuators A: Physical, 2008. **144**(1): p. 38-47.
5. Choi, H., et al., *Microfabrication and characterization of metal-embedded thin-film thermomechanical microsensors for applications in hostile manufacturing environments.* Microelectromechanical Systems, Journal of, 2006. **15**(2): p. 322-329.
6. Dao, D.V., et al., *Micro/nano-mechanical sensors and actuators based on SOI-MEMS technology.* Advances in Natural Sciences: Nanoscience and Nanotechnology, 2010. **1**(1): p. 013001.
7. Stevenson, C.L., J.T. Santini Jr, and R. Langer, *Reservoir-based drug delivery systems utilizing microtechnology.* Advanced drug delivery reviews, 2012. **64**(14): p. 1590-1602.
8. Moon, S.J., R. Lin, and U. Demirci, *CD4+ T-lymphocyte capture using a disposable microfluidic chip for HIV.* Journal of visualized experiments: JoVE, 2007(8).
9. Tokel, O., F. Inci, and U. Demirci, *Advances in Plasmonic Technologies for Point of Care Applications.* Chemical reviews, 2014.

10. Milton, G.E., *An Automated Micro-Grinding System for the Fabrication of Precision Micro-Scale Profiles.* The University of New South Wales, 2006. Thesis and dissertations-Mechanical and Manufacturing Engineering.
11. Seidemann, V., et al., *SU8-micromechanical structures with in situ fabricated movable parts.* Microsystem technologies, 2002. **8**(4-5): p. 348-350.
12. Mata, A., A.J. Fleischman, and S. Roy, *Fabrication of multi-layer SU-8 microstructures.* Journal of micromechanics and microengineering, 2006. **16**(2): p. 276.
13. Madou, M.J., *Fundamentals of microfabrication: the science of miniaturization*. 2002: CRC press.
14. Bertsch, A., et al., *Rapid prototyping of small size objects.* Rapid Prototyping Journal, 2000. **6**(4): p. 259-266.
15. Zhang, X., X. Jiang, and C. Sun, *Micro-stereolithography of polymeric and ceramic microstructures.* Sensors and Actuators A: Physical, 1999. **77**(2): p. 149-156.
16. Tan, D., et al., *Reduction in feature size of two-photon polymerization using SCR500.* Applied physics letters, 2007. **90**(7): p. 071106-071106-3.
17. Choi, S.-O., et al. *3-D patterned microstructures using inclined UV exposure and metal transfer micromolding*. in *Proc. Solid State Sensors, Actuators and Microsystems Workshop (Hilton Head, SC)*. 2006.
18. Ahn, S.H. and L.J. Guo, *High‐Speed Roll‐to‐Roll Nanoimprint Lithography on Flexible Plastic Substrates.* Advanced materials, 2008. **20**(11): p. 2044-2049.
19. Ahn, S.H. and L.J. Guo, *Large-area roll-to-roll and roll-to-plate nanoimprint lithography: a step toward high-throughput application of continuous nanoimprinting.* ACS nano, 2009. **3**(8): p. 2304-2310.
20. DiBartolomeo, F.J. and C.A. Trinkle. *High Throughput Continuous Fabrication of Large Surface Area Microstructured PDMS*. in *ASME 2009 International Mechanical Engineering Congress and Exposition*. 2009. American Society of Mechanical Engineers.
21. Vittorio, S.A. *MEMS*. 2001.

22. Feynman, R.P., *There's plenty of room at the bottom.* Engineering and science, 1960. **23**(5): p. 22-36.
23. Moore, G.E., *Cramming more components onto integrated circuits*. 1965, McGraw-Hill New York, NY, USA.
24. Judy, J.W., *Microelectromechanical systems (MEMS): fabrication, design and applications.* Smart materials and Structures, 2001. **10**(6): p. 1115.
25. Ko, W.H., *Trends and frontiers of MEMS.* Sensors and Actuators A: Physical, 2007. **136**(1): p. 62-67.
26. Fedder, G.K. *MEMS fabrication*. in *2013 IEEE International Test Conference (ITC)*. 2003. IEEE Computer Society.
27. Backer, E., et al., *Production of separation-nozzle systems for uranium enrichment by a combination of X-ray lithography and galvanoplastics.* Naturwissenschaften, 1982. **69**(11): p. 520-523.
28. Saile, V., *LIGA and its Applications*. Vol. 7. 2009: John Wiley & Sons.
29. Bruno Frazier, A. and M.G. Allen, *Metallic microstructures fabricated using photosensitive polyimide electroplating molds.* Microelectromechanical Systems, Journal of, 1993. **2**(2): p. 87-94.
30. Turner, R., et al., *Tapered LIGA HARMs.* Journal of Micromechanics and Microengineering, 2003. **13**(3): p. 367.
31. Jaeger, R.C., *Lithography. Introduction to microelectronic fabrication.* Prentice Hall, Upper Saddle River, NJ, USA, 2002.
32. Huff, M., *MEMS fabrication.* Sensor Review, 2002. **22**(1): p. 18-33.
33. Nathanson, H.C., et al., *The resonant gate transistor.* Electron Devices, IEEE Transactions on, 1967. **14**(3): p. 117-133.
34. Delille, R., et al., *Benchtop polymer MEMS.* Microelectromechanical Systems, Journal of, 2006. **15**(5): p. 1108-1120.
35. Imbaby, M.F. and K. Jiang, *Fabrication of free standing 316-L stainless steel–Al2O3 composite micro machine parts by soft moulding.* Acta Materialia, 2009. **57**(16): p. 4751-4757.

36. Seol, S.K., et al., *Fabrication of freestanding metallic micro hollow tubes by template-free localized electrochemical deposition.* Electrochemical and solid-state letters, 2007. **10**(5): p. C44-C46.
37. Lee, J.S. and S.S. Lee, *Fabrication of a freestanding micro mechanical structure using electroplated thick metal with a HAR SU-8 mold.* Microsystem Technologies, 2009. **15**(2): p. 287-296.
38. Auyeung, R., et al., *Laser decal transfer of freestanding microcantilevers and microbridges.* Applied Physics A, 2009. **97**(3): p. 513-519.
39. Zhang, D., B. Su, and T.W. Button, *Microfabrication of Three‐Dimensional, Free‐Standing Ceramic MEMS Components by Soft Moulding.* Advanced Engineering Materials, 2003. **5**(12): p. 924-927.
40. Lee, J.A., et al., *Fabrication and characterization of freestanding 3D carbon microstructures using multi-exposures and resist pyrolysis.* Journal of Micromechanics and Microengineering, 2008. **18**(3): p. 035012.
41. Jiguet, S., et al., *Conductive SU8 photoresist for microfabrication.* Advanced Functional Materials, 2005. **15**(9): p. 1511-1516.
42. Genolet, G. and H. Lorenz, *UV-LIGA: From Development to Commercialization.* Micromachines, 2014. **5**(3): p. 486-495.
43. Del Campo, A. and C. Greiner, *SU-8: a photoresist for high-aspect-ratio and 3D submicron lithography.* Journal of Micromechanics and Microengineering, 2007. **17**(6): p. R81.
44. Lorenz, H., et al., *SU-8: a low-cost negative resist for MEMS.* Journal of Micromechanics and Microengineering, 1997. **7**(3): p. 121.
45. Zhang, N., et al., *Chemical bonding of multiwalled carbon nanotubes to SU-8 via ultrasonic irradiation.* Smart materials and structures, 2003. **12**(2): p. 260.
46. Teh, W., et al., *Effect of low numerical-aperture femtosecond two-photon absorption on (SU-8) resist for ultrahigh-aspect-ratio microstereolithography.* Journal of applied physics, 2005. **97**(5): p. 054907.
47. Zhang, J., *LIGA mold insert fabrication using SU-8 photoresist*, in *Mechanical Engineering Dept.* 2002, Louisiana State Univ.: Baton Rouge, LA.

48. Zhou, F., et al., *Fabrication of positively patterned conducting polymer microstructures via one-step electrodeposition.* Advanced Materials, 2003. **15**(16): p. 1367-1370.
49. Smoukov, S.K., et al., *Freestanding Three-Dimensional Copper Foils Prepared by Electroless Deposition on Micropatterned Gels.* Advanced Materials, 2005. **17**(6): p. 751-755.
50. LaVan, D.A., P.M. George, and R. Langer, *Simple, Three-Dimensional Microfabrication of Electrodeposited Structures.* Angewandte Chemie, 2003. **115**(11): p. 1300-1303.
51. Rajagopalan, J. and M.T.A. Saif, *Fabrication of freestanding 1-D PDMS microstructures using capillary micromolding.* Microelectromechanical Systems, Journal of 2013. **22**: p. 992-994.
52. Ito, H., *Chemical amplification resists for microlithography*, in *Microlithography· Molecular Imprinting*. 2005, Springer. p. 37-245.
53. Tang, Y., et al., *Micro-layered-photolithography for Micro-Fabrication and Micro-molding.* 2005.
54. Thian, S., et al., *Micro-rapid-prototyping via multi-layered photo-lithography.* The International Journal of Advanced Manufacturing Technology, 2006. **29**(9-10): p. 1026-1032.
55. Zhu, Z., X. Wei, and K. Jiang, *A net-shape fabrication process of alumina micro-components using a soft lithography technique.* Journal of Micromechanics and Microengineering, 2007. **17**(2): p. 193.
56. Kim, E., Y. Xia, and G.M. Whitesides, *Micromolding in capillaries: applications in materials science.* Journal of the American Chemical Society, 1996. **118**(24): p. 5722-5731.
57. Suh, K.Y. and H.H. Lee, *Capillary force lithography: large-area patterning, self-organization, and anisotropic dewetting.* Advanced Functional Materials, 2002. **12**(6-7): p. 405-413.
58. Suh, K.Y., Y.S. Kim, and H.H. Lee, *Capillary force lithography.* Advanced Materials, 2001. **13**(18): p. 1386.

59. Bohl, B., et al., *Multi-layer SU-8 lift-off technology for microfluidic devices.* Journal of micromechanics and microengineering, 2005. **15**(6): p. 1125.

60. Ceyssens, F. and R. Puers, *Creating multi-layered structures with freestanding parts in SU-8.* Journal of Micromechanics and Microengineering, 2006. **16**(6): p. S19.

61. Alderman, B., et al., *Microfabrication of channels using an embedded mask in negative resist.* Journal of Micromechanics and Microengineering, 2001. **11**(6): p. 703.

62. Chuang, Y.-J., et al., *A novel fabrication method of embedded micro-channels by using SU-8 thick-film photoresists.* Sensors and Actuators A: Physical, 2003. **103**(1): p. 64-69.

63. Waits, C.M., A. Modafe, and R. Ghodssi, *Investigation of gray-scale technology for large area 3D silicon MEMS structures.* Journal of Micromechanics and Microengineering, 2003. **13**(2): p. 170.

64. Preechaburana, P. and D. Filippini, *Fabrication of monolithic 3D micro-systems.* Lab on a Chip, 2011. **11**(2): p. 288-295.

65. Waits, C., et al., *Microfabrication of 3D silicon MEMS structures using gray-scale lithography and deep reactive ion etching.* Sensors and Actuators A: Physical, 2005. **119**(1): p. 245-253.

66. Hull, C.W., *Apparatus for production of three-dimensional objects by stereolithography*. 1986, Google Patents.

67. Choi, J.-W., et al., *Cure depth control for complex 3D microstructure fabrication in dynamic mask projection microstereolithography.* Rapid Prototyping Journal, 2009. **15**(1): p. 59-70.

68. Soman, P., et al., *Digital microfabrication of user-defined 3D microstructures in cell-laden hydrogels.* Biotechnology and bioengineering, 2013. **110**(11): p. 3038-3047.

69. Maruo, S., O. Nakamura, and S. Kawata, *Three-dimensional microfabrication with two-photon-absorbed photopolymerization.* Optics letters, 1997. **22**(2): p. 132-134.

70. Kawata, S., et al., *Finer features for functional microdevices.* Nature, 2001. **412**(6848): p. 697-698.

71. Deubel, M., et al., *Direct laser writing of three-dimensional photonic-crystal templates for telecommunications.* Nature materials, 2004. **3**(7): p. 444-447.

72. Sun, H.-B. and S. Kawata, *Two-photon photopolymerization and 3D lithographic microfabrication*, in *NMR• 3D Analysis• Photopolymerization*. 2004, Springer. p. 169-273.

73. Wu, S., J. Serbin, and M. Gu, *Two-photon polymerisation for three-dimensional micro-fabrication.* Journal of Photochemistry and Photobiology A: Chemistry, 2006. **181**(1): p. 1-11.

74. Lee, K.-S., et al., *Advances in 3D nano/microfabrication using two-photon initiated polymerization.* Progress in Polymer Science, 2008. **33**(6): p. 631-681.

75. Formanek, F., et al., *Selective electroless plating to fabricate complex three-dimensional metallic micro/nanostructures.* Applied physics letters, 2006. **88**(8): p. 083110.

76. Hrapovic, S., et al., *New strategy for preparing thin gold films on modified glass surfaces by electroless deposition.* Langmuir, 2003. **19**(9): p. 3958-3965.

77. Horade, M. and S. Sugiyama, *Study on fabrication of 3-D microstructures by synchrotron radiation based on pixels exposed lithography.* Microsystem Technologies, 2010. **16**(8-9): p. 1331-1338.

78. Lee, K., et al., *Drawing Lithography: Three‐Dimensional Fabrication of an Ultrahigh‐Aspect‐Ratio Microneedle.* Advanced Materials, 2010. **22**(4): p. 483-486.

79. Rahman, M.M., et al. *3-D hemispherical micro glass-shell resonator with integrated electrostatic excitation and capacitive detection transducers*. in *Micro Electro Mechanical Systems (MEMS), 2014 IEEE 27th International Conference on*. 2014. IEEE.

80. Bell, D.J., et al. *Flagella-like Propulsion for Microrobots Using a Nanocoil and a Rotating Electromagnetic Field*. in *ICRA*. 2007.

81. Zhang, L., et al., *Characterizing the swimming properties of artificial bacterial flagella.* Nano letters, 2009. **9**(10): p. 3663-3667.

82. Zhang, L., et al., *Artificial bacterial flagella: Fabrication and magnetic control.* Applied Physics Letters, 2009. **94**(6): p. 064107.
83. Ghosh, A. and P. Fischer, *Controlled propulsion of artificial magnetic nanostructured propellers.* Nano letters, 2009. **9**(6): p. 2243-2245.
84. Peyer, K.E., L. Zhang, and B.J. Nelson, *Bio-inspired magnetic swimming microrobots for biomedical applications.* Nanoscale, 2013. **5**(4): p. 1259-1272.
85. Pesántez, D., E. Amponsah, and A. Gadre, *Wet release of multipolymeric structures with a nanoscale release layer.* Sensors and Actuators B: Chemical, 2008. **132**(2): p. 426-430.
86. Agirregabiria, M., et al., *Fabrication of SU-8 multilayer microstructures based on successive CMOS compatible adhesive bonding and releasing steps.* Lab on a Chip, 2005. **5**(5): p. 545-552.
87. Aracil, C., et al., *BETTS: bonding, exposing and transferring technique in SU-8 for microsystems fabrication.* Journal of Micromechanics and Microengineering, 2010. **20**(3): p. 035008.
88. Nathanson, H. and R. Wickstrom, *A RESONANT-GATE SILICON SURFACE TRANSISTOR WITH HIGH-Q BAND-PASS PROPERTIES.* Applied physics letters, 1965. **7**(4): p. 84-86.
89. Tuomikoski, S. and S. Franssila, *Free-standing SU-8 microfluidic chips by adhesive bonding and release etching.* Sensors and Actuators A: Physical, 2005. **120**(2): p. 408-415.
90. Lorenz, H., M. Laudon, and P. Renaud, *Mechanical characterization of a new high-aspect-ratio near UV-photoresist.* Microelectronic Engineering, 1998. **41**: p. 371-374.
91. Bogunovic, L., D. Anselmetti, and J. Regtmeier, *Photolithographic fabrication of arbitrarily shaped SU-8 microparticles without sacrificial release layers.* Journal of Micromechanics and Microengineering, 2011. **21**(2): p. 027003.
92. Tao, S.L., K. Popat, and T.A. Desai, *Off-wafer fabrication and surface modification of asymmetric 3D SU-8 microparticles.* Nature protocols, 2007. **1**(6): p. 3153-3158.

93. da Silva, L.W. and M. Kaviany, *Fabrication and measured performance of a first-generation microthermoelectric cooler.* Microelectromechanical Systems, Journal of, 2005. **14**(5): p. 1110-1117.
94. Psoma, S.D. and D.W. Jenkins, *Comparative assessment of different sacrificial materials for releasing SU-8 structures.* Reviews on Advanced Materials Science, 2005. **10**(2): p. 149-155.
95. Bagolini, A., et al., *Polyimide sacrificial layer and novel materials for post-processing surface micromachining.* Journal of Micromechanics and Microengineering, 2002. **12**(4): p. 385.
96. Azad, J.B., et al. *Release of MEMS devices with hard-baked polyimide sacrificial layer*. in *SPIE Advanced Lithography*. 2013. International Society for Optics and Photonics.
97. Mimoun, B., et al., *Residue-free plasma etching of polyimide coatings for small pitch vias with improved step coverage.* Journal of Vacuum Science & Technology B, 2013. **31**(2): p. 021201.
98. Chiamori, H., et al., *Suspension of nanoparticles in SU-8: Processing and characterization of nanocomposite polymers.* Microelectronics journal, 2008. **39**(2): p. 228-236.
99. Zevenbergen, M.A., et al., *Fast electron-transfer kinetics probed in nanofluidic channels.* Journal of the American Chemical Society, 2009. **131**(32): p. 11471-11477.
100. Wang, X., et al., *Free-standing SU-8 subwavelength gratings fabricated by UV curing imprint.* Microelectronic Engineering, 2008. **85**(5): p. 910-913.
101. Song, I.-h. and P.K. Ajmera, *Use of a photoresist sacrificial layer with SU-8 electroplating mould in MEMS fabrication.* Journal of Micromechanics and Microengineering, 2003. **13**(6): p. 816.
102. Foulds, I.G., R. Johnstone, and M. Parameswaran, *Polydimethylglutarimide (PMGI) as a sacrificial material for SU-8 surface-micromachining.* Journal of Micromechanics and Microengineering, 2008. **18**(7): p. 075011.

103. Hasan, S.A., D.W. Kavich, and J.H. Dickerson, *Sacrificial layer electrophoretic deposition of free-standing multilayered nanoparticle films.* Chem. Commun., 2009(25): p. 3723-3725.

104. Ahn, C.H., Y.J. Kim, and M.G. Allen, *A planar variable reluctance magnetic micromotor with fully integrated stator and coils.* Microelectromechanical Systems, Journal of, 1993. **2**(4): p. 165-173.

105. DeVoe, D.L. and A.P. Pisano, *Surface micromachined piezoelectric accelerometers (PiXLs).* Microelectromechanical Systems, Journal of, 2001. **10**(2): p. 180-186.

106. Zavracky, P.M., S. Majumder, and N.E. McGruer, *Micromechanical switches fabricated using nickel surface micromachining.* Microelectromechanical Systems, Journal of, 1997. **6**(1): p. 3-9.

107. Younse, J.M., *Mirrors on a chip.* Spectrum, IEEE, 1993. **30**(11): p. 27-31.

108. Avinash P. Nayak, e.a. *Wet and Dry Etching*.

109. Irving, S. *A Dry Photoresist Removal Method*. in *JOURNAL OF THE ELECTROCHEMICAL SOCIETY*. 1967. ELECTROCHEMICAL SOC INC 10 SOUTH MAIN STREET, PENNINGTON, NJ 08534.

110. Irving, S., *Plasma oxidation process for removing photoresist films.* Solid State Technology, 1971. **14**(6): p. 47-&.

111. Irving, S.M., K.E. Lemons, and G.E. Bobos, *Gas plasma vapor etching process*. 1971, US Patent 3,615,956.

112. Shikida, M., et al., *The mechanism of selective corrugation removal by KOH anisotropic wet etching.* Journal of Micromechanics and Microengineering, 2010. **20**(1): p. 015038.

113. Radjenović, B., M. Radmilović-Radjenović, and M. Mitrić, *Level set approach to anisotropic wet etching of silicon.* Sensors, 2010. **10**(5): p. 4950-4967.

114. Lee, H.W., *Three-dimensional micro fabrication of active micro devices using soft functional materials*. 2011, University of Illinois at Urbana-Champaign.

115. Trimmer, W.S., *Microrobots and micromechanical systems.* Sensors and actuators, 1989. **19**(3): p. 267-287.

116. Cugat, O., J. Delamare, and G. Reyne, *Magnetic micro-actuators and systems (MAGMAS).* Magnetics, IEEE Transactions on, 2003. **39**(6): p. 3607-3612.
117. Sakar, M.S., et al., *Single cell manipulation using ferromagnetic composite microtransporters.* Applied physics letters, 2010. **96**(4): p. 043705.
118. Leong, T.G., et al., *Tetherless thermobiochemically actuated microgrippers.* Proceedings of the National Academy of Sciences, 2009. **106**(3): p. 703-708.
119. Pawashe, C., S. Floyd, and M. Sitti, *Modeling and experimental characterization of an untethered magnetic micro-robot.* The International Journal of Robotics Research, 2009. **28**(8): p. 1077-1094.
120. Vollmers, K., et al., *Wireless resonant magnetic microactuator for untethered mobile microrobots.* Applied Physics Letters, 2008. **92**(14): p. 144103.
121. Li, H., et al., *Photopatternable NdFeB polymer micromagnets for microfluidics and microrobotics applications.* Journal of Micromechanics and Microengineering, 2013. **23**(6): p. 065002.
122. Donald, B.R., et al., *An untethered, electrostatic, globally controllable MEMS micro-robot.* Microelectromechanical Systems, Journal of, 2006. **15**(1): p. 1-15.
123. Pawashe, C., S. Floyd, and M. Sitti, *Multiple magnetic microrobot control using electrostatic anchoring.* Applied Physics Letters, 2009. **94**(16): p. 164108-164108-3.
124. Sul, O., et al., *Thermally actuated untethered impact-driven locomotive microdevices.* Applied Physics Letters, 2006. **89**(20): p. 203512.
125. Hsi-Wen, T., et al., *Polymer-Based Wireless Resonant Magnetic Microrobots.* Robotics, IEEE Transactions on, 2014. **30**(1): p. 26-32.
126. Frutiger, D.R., et al., *Small, fast, and under control: wireless resonant magnetic micro-agents.* The International Journal of Robotics Research, 2010. **29**(5): p. 613-636.
127. Yesin, K.B., K. Vollmers, and B.J. Nelson, *Modeling and control of untethered biomicrorobots in a fluidic environment using electromagnetic fields.* The International Journal of Robotics Research, 2006. **25**(5-6): p. 527-536.
128. Mathieu, J.-B., G. Beaudoin, and S. Martel, *Method of propulsion of a ferromagnetic core in the cardiovascular system through magnetic gradients*

generated by an MRI system. Biomedical Engineering, IEEE Transactions on, 2006. **53**(2): p. 292-299.

129. Donald, B.R., et al. *Power delivery and locomotion of untethered micro-actuators*. in *Micro Electro Mechanical Systems, 2003. MEMS-03 Kyoto. IEEE The Sixteenth Annual International Conference on*. 2003.
130. Donald, B.R., C.G. Levey, and I. Paprotny, *Planar Microassembly by Parallel Actuation of MEMS Microrobots.* Microelectromechanical Systems, Journal of, 2008. **17**(4): p. 789-808.
131. Ohmichi, O., Y. Yamagata, and T. Higuchi, *Micro impact drive mechanisms using optically excited thermal expansion.* Microelectromechanical Systems, Journal of, 1997. **6**(3): p. 200-207.
132. de Boer, M.P., et al., *High-performance surface-micromachined inchworm actuator.* Microelectromechanical Systems, Journal of, 2004. **13**(1): p. 63-74.
133. Hou, M.T., et al., *A rolling locomotion method for untethered magnetic microrobots.* Applied Physics Letters, 2010. **96**(2): p. 024102.
134. Hagiwara, M., et al., *On-chip magnetically actuated robot with ultrasonic vibration for single cell manipulations.* Lab Chip, 2011. **11**(12): p. 2049-2054.
135. Jing, W. and D. Cappelleri, *A Magnetic Microrobot with in situ Force Sensing Capabilities.* Robotics, 2014. **3**(2): p. 106-119.
136. Kim, S., et al., *Fabrication and Characterization of Magnetic Microrobots for Three-Dimensional Cell Culture and Targeted Transportation.* Advanced Materials, 2013. **25**(41): p. 5863-5868.
137. Ganesh A, D. and C. Velammal Engineering College, *Design of Micro Robot for Minimally Invasive Surgery.* IAES International Journal of Robotics and Automation (IJRA), 2013. **2**(1): p. 35-44.
138. Ullrich, F., et al., *Mobility experiments with microrobots for minimally invasive intraocular surgery.* Investigative ophthalmology & visual science, 2013. **54**(4): p. 2853-2863.
139. Chatzipirpiridis, G., et al., *Electroforming of Implantable Tubular Magnetic Microrobots for Wireless Ophthalmologic Applications.* Advanced healthcare materials, 2014.

140. Kummer, M.P., et al., *OctoMag: An electromagnetic system for 5-DOF wireless micromanipulation.* Robotics, IEEE Transactions on, 2010. **26**(6): p. 1006-1017.
141. Schuerle, S., et al., *Three-dimensional magnetic manipulation of micro-and nanostructures for applications in life sciences.* Magnetics, IEEE Transactions on, 2013. **49**(1): p. 321-330.
142. Khalil, I.S., et al., *Three-dimensional closed-loop control of self-propelled microjets.* Applied Physics Letters, 2013. **103**(17): p. 172404.
143. Lu, L.-H., K.S. Ryu, and C. Liu, *A magnetic microstirrer and array for microfluidic mixing.* Microelectromechanical Systems, Journal of, 2002. **11**(5): p. 462-469.
144. Yamahata, C., et al., *A PMMA valveless micropump using electromagnetic actuation.* Microfluidics and Nanofluidics, 2005. **1**(3): p. 197-207.
145. Wörn, H., et al. *Flexible microrobots for micro assembly tasks*. in *Micromechatronics and Human Science, 2000. MHS 2000. Proceedings of 2000 International Symposium on*. 2000. IEEE.
146. Nelson, B.J., I.K. Kaliakatsos, and J.J. Abbott, *Microrobots for minimally invasive medicine.* Annual review of biomedical engineering, 2010. **12**: p. 55-85.
147. Floyd, S., C. Pawashe, and M. Sitti. *An untethered magnetically actuated micro-robot capable of motion on arbitrary surfaces*. in *Robotics and Automation, 2008. ICRA 2008. IEEE International Conference on*. 2008. IEEE.
148. Damean, N., et al., *Composite ferromagnetic photoresist for the fabrication of microelectromechanical systems.* Journal of Micromechanics and Microengineering, 2005. **15**(1): p. 29.
149. Tsai, K.L., et al., *Magnetic, mechanical, and optical characterization of a magnetic nanoparticle-embedded polymer for microactuation.* Microelectromechanical Systems, Journal of, 2011. **20**(1): p. 65-72.
150. Gach, P.C., C.E. Sims, and N.L. Allbritton, *Transparent magnetic photoresists for bioanalytical applications.* Biomaterials, 2010. **31**(33): p. 8810-8817.
151. Suter, M., et al., *A photopatternable superparamagnetic nanocomposite: Material characterization and fabrication of microstructures.* Sensors and Actuators B: Chemical, 2011. **156**(1): p. 433-443.

152. Kim, J., et al., *Programming magnetic anisotropy in polymeric microactuators.* Nature materials, 2011. **10**(10): p. 747-752.
153. Chronis, N. and L.P. Lee, *Electrothermally activated SU-8 microgripper for single cell manipulation in solution.* Journal of Microelectromechanical Systems, 2005. **14**(4): p. 857-863.
154. Bornside, D.E., C.W. Macosko, and L.E. Scriven, *Spin Coating - One-Dimensional Model.* Journal of Applied Physics, 1989. **66**(11): p. 5185-5193.
155. Zhang, W., S.-X. Guo, and K. Asaka, *A new type of hybrid fish-like microrobot.* International Journal of Automation and Computing, 2006. **3**(4): p. 358-365.
156. Abbott, J., et al., *Robotics in the small.* IEEE Robotics and Automation Magazine, 2007. **14**: p. 92-103.
157. Nagy, Z. and B.J. Nelson, *Lagrangian Modeling of the Magnetization and the Magnetic Torque on Assembled Soft-Magnetic MEMS Devices for Fast Computation and Analysis.* Robotics, IEEE Transactions on, 2012. **28**(4): p. 787-797.
158. Gillies, G., et al., *Magnetic manipulation instrumentation for medical physics research.* Review of Scientific Instruments, 1994. **65**(3): p. 533-562.
159. Hong, L. and T. Pan, *Photopatternable superhydrophobic nanocomposites for microfabrication.* Microelectromechanical Systems, Journal of, 2010. **19**(2): p. 246-253.
160. García, E.J., et al., *Fabrication and Nanocompression Testing of Aligned Carbon-Nanotube–Polymer Nanocomposites.* Advanced materials, 2007. **19**(16): p. 2151-2156.
161. Leachman, W., et al., *Statistical analysis of wear of biplanar deterministically-arrayed surfaces for load bearing applications.* Wear, 2014. **311**(1): p. 137-148.
162. Stout, K.J. and L. Blunt, *Three dimensional surface topography*. 2000: Elsevier.
163. Leachman, W.J., *Effects of Surface Parameters on Hydrodynamic Lubrication for Non Gaussian Surfaces*. 2010, University of Kentucky.
164. Erni, S., et al., *Comparison, optimization, and limitations of magnetic manipulation systems.* Journal of Micro-Bio Robotics, 2013. **8**(3-4): p. 107-120.
165. Eisele, R.H., *Smart data storage device*. 1992, Google Patents.

166. Wickramasinghe, H.K. and F. Zenhausern, *Method and apparatus for mass data storage*. 1997, Google Patents.
167. Sadiku, M.N., *Elements of electromagnetics*. 2007: Oxford university press.
168. Abbott, J.J., et al., *Modeling magnetic torque and force for controlled manipulation of soft-magnetic bodies.* Robotics, IEEE Transactions on, 2007. **23**(6): p. 1247-1252.
169. Yesin, K.B., et al., *Design and control of in-vivo magnetic microrobots*, in *Medical Image Computing and Computer-Assisted Intervention–MICCAI 2005*. 2005, Springer. p. 819-826.
170. Yesin, K.B., K. Vollmers, and B.J. Nelson, *Actuation, sensing, and fabrication for in vivo magnetic microrobots*, in *Experimental Robotics IX*. 2006, Springer. p. 321-330.
171. Fisher, J., et al., *Magnetic force micromanipulation systems for the biological sciences.* NANO, 2006. **1**(03): p. 191-205.
172. Furlani, E.P., *Permanent magnet and electromechanical devices: materials, analysis, and applications*. 2001: Academic Press.
173. *Coercivity and Remanence in Permanent Magnets*.
174. Cribb, J.A., et al., *Cylinders vs. spheres: biofluid shear thinning in driven nanoparticle transport.* Annals of biomedical engineering, 2010. **38**(11): p. 3311-3322.
175. Haus, H.A. and J.R. Melcher, *Electromagnetic fields and energy*. 1989: Prentice Hall Englewood Cliffs.
176. Hanselman, D.C., *Brushless permanent-magnet motor design*. 1994: McGraw-Hill New York.
177. Batchelor, G.K., *An introduction to fluid dynamics*. 2000: Cambridge university press.
178. Herwig, H. and O. Hausner, *Critical view on "new results in micro-fluid mechanics": an example.* International Journal of Heat and Mass Transfer, 2003. **46**(5): p. 935-937.
179. Moon, S., et al., *Enumeration of CD4+ T-cells using a portable microchip count platform in Tanzanian HIV-infected patients.* PLoS One, 2011. **6**(7): p. e21409.

180. Han, M., et al., *3D microfabrication with inclined/rotated UV lithography.* Sensors and Actuators A: Physical, 2004. **111**(1): p. 14-20.

181. Ahn, S.-W., et al., *Fabrication of a 50 nm half-pitch wire grid polarizer using nanoimprint lithography.* Nanotechnology, 2005. **16**(9): p. 1874.

182. Chou, S.Y., P.R. Krauss, and P.J. Renstrom, *Nanoimprint lithography.* Journal of Vacuum Science & Technology B, 1996. **14**(6): p. 4129-4133.

183. Choi, C.H., et al., *Surface‐Tension‐Induced Synthesis of Complex Particles Using Confined Polymeric Fluids.* Angewandte Chemie, 2010. **122**(42): p. 7914-7918.

184. Rolland, J.P., et al., *Direct fabrication and harvesting of monodisperse, shape-specific nanobiomaterials.* Journal of the American Chemical Society, 2005. **127**(28): p. 10096-10100.

185. Heule, M. and L.J. Gauckler, *Gas sensors fabricated from ceramic suspensions by micromolding in capillaries.* Advanced Materials, 2001. **13**(23): p. 1790-1793.

186. Coq, N., et al., *Self-supporting hydrogel stamps for the microcontact printing of proteins.* Langmuir, 2007. **23**(9): p. 5154-5160.

187. Mellott, M.B., K. Searcy, and M.V. Pishko, *Release of protein from highly cross-linked hydrogels of poly (ethylene glycol) diacrylate fabricated by UV polymerization.* Biomaterials, 2001. **22**(9): p. 929-941.

188. Lopérgolo, L.C., A.B. Lugão, and L.H. Catalani, *Direct UV photocrosslinking of poly (< i> N</i>-vinyl-2-pyrrolidone)(PVP) to produce hydrogels.* Polymer, 2003. **44**(20): p. 6217-6222.

189. Wu, Q., et al., *A high strength nanocomposite based on microcrystalline cellulose and polyurethane.* Biomacromolecules, 2007. **8**(12): p. 3687-3692.

190. Jiguet, S., et al., *SU8‐Silver Photosensitive Nanocomposite.* Advanced Engineering Materials, 2004. **6**(9): p. 719-724.

191. Heckele, M. and W. Schomburg, *Review on micro molding of thermoplastic polymers.* Journal of Micromechanics and Microengineering, 2004. **14**(3): p. R1.

192. Trinkle, C.A., *Kinematic Alignment System for the Creation of Integrated Microfluidic Devices*. 2008: ProQuest.

193. Vafaei, A., *Simple, economical methods for electrical access to nanostructures used for characterizing and welding individual silver nanowires*. 2013, University of Waterloo: Waterloo, Ontario, Canada.

194. Chiamori, H.C., et al., *Suspension of nanoparticles in SU-8: Processing and characterization of nanocomposite polymers.* Microelectronics Journal, 2008. **39**(2): p. 228-236.

195. Guo, Y., et al., *Study of Hot Embossing Using Nickel and Ni–PTFE LIGA Mold Inserts.* Microelectromechanical Systems, Journal of, 2007. **16**(3): p. 589-597.

Vita

Hui Li was born in Xianyang, Shaanxi, China. He received his B.S. degree and M.S. degree in mechanical Engineering from the school of Mechanical Engineering at the Northwestern Polytechnical University in Xi'an, China. Then he came to the Department of Mechanical Engineering at the University of Kentucky for doctoral study. Currently, he is a Ph.D. candidate and research assistant in MEMS, microrobotics and microfluidics research fields.